Study of an ettringite-based thermochemical energy storage for buildings

Bao Chen

N°d'ordre NNT : 2020LYSEI056

THESE de DOCTORAT DE L'UNIVERSITE DE LYON
opérée au sein de
l'Institut National des Sciences Appliquées de Lyon

Ecole Doctorale N° ED 162
MEGA
(Mécanique, Énergétique, Génie Civil, Acoustique)

Spécialité/ discipline de doctorat :

Thermique et Energétique

Soutenue publiquement le 22/07/2020, par :
Bao Chen

Study of an ettringite-based thermochemical energy storage for buildings

---

Devant le jury composé de :

Ginestet, Stéphane	Professeur des Universités, INSA-Toulouse	Rapporteur
Le-Pierrès, Nolwenn	Professeure des Universités, Université Savoie Mont Blanc	Rapporteuse
Zondag, Herbert A.	Professeur des Universités, Eindhoven University of Technology	Examinateur
Roux, Jean-Jacques	Professeur des Universités, INSA-Lyon	Examinateur
Kuznik, Frédéric	Professeur des Universités, INSA-Lyon	Directeur de thèse
Johannes, Kévyn	Maître de Conférences (HDR), Université Claude Bernard Lyon 1	Co-directeur de thèse
Horgnies, Matthieu	Docteur, HDR, Ingénieur de recherche, LafargeHolcim Innovation Center	Co-encadrant de thèse

Département FEDORA – INSA Lyon – Ecoles Doctorales – Quinquennal 2016-2020

SIGLE	ECOLE DOCTORALE	NOM ET COORDONNEES DU RESPONSABLE
CHIMIE	**CHIMIE DE LYON** http://www.edchimie-lyon.fr Sec. : Renée EL MELHEM Bât. Blaise PASCAL, 3e étage secretariat@edchimie-lyon.fr INSA : R. GOURDON	**M. Stéphane DANIELE** Institut de recherches sur la catalyse et l'environnement de Lyon IRCELYON-UMR 5256 Équipe CDFA 2 Avenue Albert EINSTEIN 69 626 Villeurbanne CEDEX directeur@edchimie-lyon.fr
E.E.A.	**ÉLECTRONIQUE, ÉLECTROTECHNIQUE, AUTOMATIQUE** http://edeea.ec-lyon.fr Sec. : M.C. HAVGOUDOUKIAN ecole-doctorale.eea@ec-lyon.fr	**M. Gérard SCORLETTI** École Centrale de Lyon 36 Avenue Guy DE COLLONGUE 69 134 Écully Tél : 04.72.18.60.97 Fax 04.78.43.37.17 gerard.scorletti@ec-lyon.fr
E2M2	**ÉVOLUTION, ÉCOSYSTÈME, MICROBIOLOGIE, MODÉLISATION** http://e2m2.universite-lyon.fr Sec. : Sylvie ROBERJOT Bât. Atrium, UCB Lyon 1 Tél : 04.72.44.83.62 INSA : H. CHARLES secretariat.e2m2@univ-lyon1.fr	**M. Philippe NORMAND** UMR 5557 Lab. d'Ecologie Microbienne Université Claude Bernard Lyon 1 Bâtiment Mendel 43, boulevard du 11 Novembre 1918 69 622 Villeurbanne CEDEX philippe.normand@univ-lyon1.fr
EDISS	**INTERDISCIPLINAIRE SCIENCES-SANTÉ** http://www.ediss-lyon.fr Sec. : Sylvie ROBERJOT Bât. Atrium, UCB Lyon 1 Tél : 04.72.44.83.62 INSA : M. LAGARDE secretariat.ediss@univ-lyon1.fr	**Mme Sylvie RICARD-BLUM** Institut de Chimie et Biochimie Moléculaires et Supramoléculaires (ICBMS) - UMR 5246 CNRS - Université Lyon 1 Bâtiment Curien - 3ème étage Nord 43 Boulevard du 11 novembre 1918 69622 Villeurbanne Cedex Tel : +33(0)4 72 44 82 32 sylvie.ricard-blum@univ-lyon1.fr
INFOMATHS	**INFORMATIQUE ET MATHÉMATIQUES** http://edinfomaths.universite-lyon.fr Sec. : Renée EL MELHEM Bât. Blaise PASCAL, 3e étage Tél : 04.72.43.80.46 infomaths@univ-lyon1.fr	**M. Hamamache KHEDDOUCI** Bât. Nautibus 43, Boulevard du 11 novembre 1918 69 622 Villeurbanne Cedex France Tel : 04.72.44.83.69 hamamache.kheddouci@univ-lyon1.fr
Matériaux	**MATÉRIAUX DE LYON** http://ed34.universite-lyon.fr Sec. : Stéphanie CAUVIN Tél : 04.72.43.71.70 Bât. Direction ed.materiaux@insa-lyon.fr	**M. Jean-Yves BUFFIÈRE** INSA de Lyon MATEIS - Bât. Saint-Exupéry 7 Avenue Jean CAPELLE 69 621 Villeurbanne CEDEX Tél : 04.72.43.71.70 Fax : 04.72.43.85.28 jean-yves.buffiere@insa-lyon.fr
MEGA	**MÉCANIQUE, ÉNERGÉTIQUE, GÉNIE CIVIL, ACOUSTIQUE** http://edmega.universite-lyon.fr Sec. : Stéphanie CAUVIN Tél : 04.72.43.71.70 Bât. Direction mega@insa-lyon.fr	**M. Jocelyn BONJOUR** INSA de Lyon Laboratoire CETHIL Bâtiment Sadi-Carnot 9, rue de la Physique 69 621 Villeurbanne CEDEX jocelyn.bonjour@insa-lyon.fr
ScSo	**ScSo*** http://ed483.univ-lyon2.fr Sec. : Véronique GUICHARD INSA : J.Y. TOUSSAINT Tél : 04.78.69.72.76 veronique.cervantes@univ-lyon2.fr	**M. Christian MONTES** Université Lyon 2 86 Rue Pasteur 69 365 Lyon CEDEX 07 christian.montes@univ-lyon2.fr

*ScSo : Histoire, Géographie, Aménagement, Urbanisme, Archéologie, Science politique, Sociologie, Anthropologie

Acknowledgement

First of all, I would like to thank the Association Nationale de la Recherche et de la Technologie (ANRT) of France and LafargeHolcim innovation center for their financial contribution to this project. I also appreciate the LafargeHolcim Innovation Center and INSAVALOR for giving me the opportunity to attend courses and conferences. Most importantly, I feel very lucky to meet a group of fantastic researchers in the “thermal energy storage and cement world”, who have enlarged my scientific horizon.

I address my great appreciation to my thesis directors, Prof. Frédéric Kuznik and Dr. Kévyn Johannes (HDR), for their guidance during the development of this thesis work. Their trust, rigor, support, and large scientific horizon were very important to me during the three years of the thesis. A big thanks to the INSA de Lyon, especially the CETHIL, for their welcome my presence to do the thesis research.

My Ph.D. was a CIFRE-type project. I have the great honor to do some part of the thesis work at LafargeHolcim Innovation Center. I express all appreciation to my industrial advisor, Dr. Matthieu Horgnies (HDR), for the supervision, confidence, and support he gave for the thesis. As a colleague, he showed me not only his profession and intelligence but also kindness and warmth throughout my thesis and internship at the company. I equally thank my industrial co-advisors, Dr. Vincent Morin and Dr. Edouard Gemgembre, for all the contributions they have done for the project. Very special thanks to Dr. Bruno Huet who shared a lot his professional knowledge and encouragement to the work.

I would like to thank my thesis reporters and examiners, Prof. Nolwenn Le-Pierrès, Prof. Stéphane Ginestet, Prof. Herbert A. Zondag, and Prof. Jean-Jacques Roux for critically reviewing this work.

I immensely express my gratitude to LafargeHolcim Innovation Center for the precious opportunity they offered to allow me to pursue my Ph.D. degree and being a research engineer in the Product & Solutions department. I treat it as a unique and special experience for not only scientific training but management learning, which is not accessible for a conventional Ph.D. student. I express thanks to my co-office colleagues, Mr. Pascal Bost and Mrs. Fabienne Legrand. They always helped me out and shared their fantastic life experiences. I am grateful to learn from Mrs. Isabelle Baco for XRD, TGA, and other experimental skills.

Thanks a lot to the technical support team and management team of CETHIL, INSAVALOR and LafargeHolcim Innovation Center for their collaboration and administrative management which are extremely important to succeed.

I owe everything that I have achieved to my family. I thank greatly my beautiful wife Jie for supporting me in this adventure. I thank also my baby on the way, for being my motivation to fight. I appreciate my mom Weiqin, my dad Shuitang, my sister Lieping and all relatives in China. They always encouraged me to embarrass the new worlds and challenges.

I would also like to thank all the new friends we made in my third hometown – the Alpes land (France), for their friendship and for the great experiences we share together.

I dedicate this work to my family, to my colleagues and to my friends.

Villeurbanne, June 09, 2020 Bao Chen

Abstract

The high energy demands for space heating and domestic hot water in buildings, characterized by peaks in consumption at the beginning and end of the day as well as in winter, represent a major challenge in terms of the use of renewable energies. A system of thermochemical energy storage (TCES), one of the most promising accessible technologies, could store different types of energies as chemical potential without energy dissipation. As a recently studied TCES material, ettringite is suitable for large scale use due to its no-toxicity, low material cost, and high energy density at lowing operating temperature.

The first objective of this thesis was to study the physicochemical properties of ettringite and the reaction mechanisms during the hydration (formation of ettringite) and dehydration (formation of meta-ettringite) processes. The knowledge obtained on the reaction kinetics and thermodynamics (Dehydration: Ett30.6 → Ett30 → Met12 → Met6; Hydration: Met7.4 → Met12 →24-hydrate → higher hydrates) allows better use of ettringite for heat storage/release (under different isothermal and isobaric conditions).

After having studied the properties of pure ettringite, three different cementitious binders that are industrially producible were used to test different ettringite contents but also mixtures of particular hydrated phases. The work carried out made it possible to study the carbonation mechanisms of these different ettringite materials and to deduce some relevant information as to their durability in terms of their use in TCES.

Finally, the ettringite-based material most resistant to the carbonation phenomenon has been characterized by different analysis techniques in order to better control the influence of thermo-physical parameters on its energy performance. This material was then incorporated into a fixed bed reactor in the form of a 56 mm high porous bed composed of granules (1–2 mm in diameter). The energy charging / discharging process carried out to study the reversibility of ettringite / meta-ettringite under various experimental conditions. The reactor tests then showed that a maximum instantaneous power of 915 W per kg of initial hydrated material and an energy-releasing density of 176 kWh/m^3. These results will be very useful in designing a future prototype (in scale 1:1) containing ettringite materials for a heating system in buildings.

Keywords: building heating supply, carbonation, ettringite, fixed-bed reactor, hydration / dehydration, kinetic, meta-ettringite, thermochemical energy storage, thermodynamic.

Résumé

Les besoins en énergie dédiés au chauffage et à l'eau chaude sanitaire dans des bâtiments, caractérisés par des pics de consommation en début et en fin de journée tout comme en hiver, représentent un défi d'importance vis-à-vis de l'utilisation des énergies renouvelables. Une des technologies les plus prometteuses, se présente sous la forme d'un système de stockage d'énergie dit thermochimique (TCES). Ce mode de stockage permet en effet de stocker différents types d'énergie sous la forme d'un potentiel chimique et est caractérisé par une absence de dissipation d'énergie. En tant que matériau de stockage thermochimique récemment étudié, l'ettringite conviendrait ainsi à une utilisation à grande échelle en raison de sa non-toxicité, de son faible coût de production et de sa haute densité énergétique à basse température de fonctionnement.

Cette thèse avait pour premier objectif d'étudier les propriétés physico-chimiques de l'ettringite et les mécanismes réactionnels lors des processus d'hydratation (formation d'ettringite) et de déshydratation (formation de méta-ettringite). Les connaissances acquises lors de ces travaux de thèse, vis-à-vis de la cinétique des réactions et des diagrammes thermodynamiques (Déshydratation: Ett30.6 → Ett30 → Met12 → Met6; Hydratation: Met7.4 → Met12 →hydrate de $24H_2O$→ hydrates supérieurs), permettront ainsi de mieux utiliser l'ettringite pour stocker/déstocker de la chaleur (à différentes conditions isothermes et isobares).

Après avoir étudié les propriétés de l'ettringite pure, trois liants cimentaires distincts pouvant être produits industriellement ont été utilisés afin de tester des teneurs en ettringite différentes mais aussi des mélanges de phases hydratées particulières. Les travaux effectués ont permis d'étudier les mécanismes de carbonatation de ces différents matériaux ettringitiques et de déduire plusieurs informations pertinentes quant à leur durabilité dans le cadre d'une utilisation en tant que TCES.

Enfin, le matériau cimentaire ettringitique le plus résistant au phénomène de carbonatation a été caractérisé par différentes techniques d'analyse afin de mieux maîtriser l'influence des paramètres thermo-physiques sur sa performance énergétique. Ce matériau a ensuite été incorporé dans un réacteur à lit fixe, sous la forme d'un lit poreux de 56 mm de hauteur composé de granulés de 1 à 2 mm de diamètre. Le processus de chargement/déchargement de l'énergie a été réalisé pour étudier la réversibilité du couple ettringite/méta-ettringite dans diverses conditions expérimentales. Les essais réalisés dans le réacteur ont alors montré qu'une puissance instantanée maximale de 915 W par kg de matière hydratée initiale et une densité de déstockage d'énergie de 176 kWh/m^3 pouvaient être obtenues. Ces données seront très utiles

pour envisager un futur prototype (à l'échelle 1:1) d'un système de chauffage contenant de l'ettringite et destiné aux bâtiments.

Mots clés : alimentation en chauffage des bâtiments, carbonatation, cinétique, ettringite, hydratation/déshydratation, méta-ettringite, réacteur à lit fixe, stockage d'énergie thermochimique, thermodynamique.

Nomenclature

Abbreviation

AFt	Calcium trisulfoaluminate hydrate, ettringite
BCSAF	Belite-Calcium Sulfoaluminate-Ferrite cement
BET	Brunauer-Emmett-Teller
BTES	Borehole thermal energy storage
CAC	Calcium Aluminate cement
CSA	Calcium Sulfoaluminate
C-S-H	Calcium Silicate Hydrate
CSP	Concentrating solar power
DA	Degree of advancement
Deh	Dehydrated
DHW	Domestic hot water
DSC	Differential scanning calorimetry
DTA	Differential thermal analysis
DVS	Dynamic vapour sorption
EttX	Ettringite contains X water molecules
dHF	Derivation of heat flow
FDDW	Fresh decarbonized demineralized water
FTIR	Fourier-transform infrared spectroscopy
Hc	Hemicarbonate
Hy	Hydrated
MetX	Meta-ettringite contains X water molecules
MIP	Mercury Intrusion Porosimetry
OPC	Ordinary Portland cement
PCM	Phase change materials
PWVP	Partial water vapor pressure
p	Pre-blended
RH	Relative humidity
SAED	Selected area electron diffraction
SEM	Scanning electron microscope
SSA	Specific surface area
TCES	Thermochemical (sorption) energy storage

TES	Thermal energy storage
TESC	Thermal energy storage capacity
TG / TGA	Thermogravimetric analysis
w/s	Water-solid weight ratio
XRD	X-ray Diffraction
XRF	X-ray fluorescence

Latin Symbols

a	**a**-parameter of crystal	nm
a	Weight percentage	%
c	**c**-parameter of crystal	nm
C_p	Specific heat capacity	J/(kg·K)
D	Density	kg/m^3
d	Diameter	µm
E_a	Apparent activation energy	J/mol
I	CO_2 binding quantity	$g_{CO2}/g_{\text{anhydrous mixture}}$
K	Reaction equilibrium constant	-
M	Molar mass	g/mol
m	Material mass	g
$\dot{m}$	Mass flowrate	g/s
n	Calculated water molecule number	-
N_A	Avogadro constant	6.022×10^{23} mol^{-1}
P	Pressure	Pa, hPa or mbar
p	Porosity	%
P_S	System output power	W
Q	Quantity of thermal energy	J
Q_V	Airflow rate	m^3/h
R	Gas constant	8.314 J/(mol·K)
S_l	Liquid saturation degree	%
T	Temperature	°C or K
t	time	s
V	Volume	m^3
wc.	Mass percentage based on anhydrous blend	%

wt.	Mass percentage	%
X	Water molecule number in the phase	-
X	Recalculated mass percentage	%
v	carbonation speed	s^{-1}
x	carbonation rate	-

Greek Symbols

α	Reaction proportion	-
ΔG	Gibbs free energy change	J/mol
ΔH	Enthalpy change	J/mol
ΔS	Entropy change	J/(mol·K)
Δm_t	Cumulative weight change	g
ρ	Density	kg/m^3
ϕ	Relative humidity	%

Subscripts

c	Condensation
e	Evaporation
eq	Equilibrium
exp	Experimental
fusion	Fusion
H_2O	Water
i	initial
in	Entry
inlet	inlet
max	Maximal
n	Step number
o	Standard conditions
out	Exit
outlet	Outlet
r	Real
sat	Saturated

st	Steam point
vap	Vaporization
w	Water vapor
0	Time zero

Cement notion

A	Alumina (Al_2O_3)
C	Lime (CaO)
$\bar{C}$	Carbon dioxide (CO_2)
H	Water (H_2O)
F	Iron oxide (Fe_2O_3)
M	Periclase (MgO)
S	Silica (SiO_2)
$\bar{S}$	Sulphur trioxide (SO_3)
T	Titanium dioxide (TiO_2)

Contents

Chapter I. General introduction 1

1.1 Background of the energy challenge 2
1.2 TES technologies 4
1.2.1 Sensible heat storage 4
1.2.2 Latent heat storage 6
1.2.3 Heat storage by sorption 7
1.3 New candidate for TCES 10
1.4 General layout of the thesis 11
1.5 References 12

Chapter II. Review on physicochemical properties of ettringite/meta-ettringite 17

2.1 Introduction 18
2.2 Formation of ettringite 20
2.2.1 Conversion based on solutions 20
2.2.2 Conversion based on solids 20
2.2.2.1 Ettringite conversed by CA or C_3A 21
2.2.2.2 Ettringite conversed by $C_4A_3\overline{S}$ 21
2.2.2.3 "Alumina, ferric oxide, monosulfate" transformation method 22
2.2.3 Mechanism of formation 22
2.3 Crystal structure 23
2.3.1 Structure of ettringite crystals 23
2.3.2 Structure of meta-ettringite 28
2.4 Thermal properties of ettringite and meta-ettringite 30
2.4.1 Decomposition of ettringite 30
2.4.2 Dehydration of ettringite 31
2.4.3 Hydration of meta-ettringite 36
2.4.4 Dehydration and hydration modelling of ettringite vs. meta-ettringite 37
2.4.5 Reaction enthalpies of dehydration and hydration 39
2.5 Chemical stability of ettringite relating to thermal energy storage 42
2.5.1 Carbonation of ettringite 42
2.5.2 Ionic substitution phenomenon 46
2.6 Prototypes adapted to ettringite-based materials 50
2.6.1 Matsushita Electric Works, Ltd. Case 50
2.6.2 Swiss Federal Laboratories for Materials Science and Technology (Empa) reactor cases 51
2.6.3 Institut National des Sciences Appliquées de Toulouse (INSA Toulouse) cases 53
2.6.4 Sorbent separating reactor case (Univ. of Stuttgart) 55
2.7 Conclusion 56
2.8 Objectives of the thesis 57
2.9 References 58

Chapter III. Thermodynamics and kinetics study on ettringite 67

3.1 Materials and methodology 69
3.1.1 Preparation of materials 69
3.1.2 Characterization methods 69

3.1.2.1 Particle size analysation 69
3.1.2.2 XRD analysis 69
3.1.2.3 TGA analysis 70
3.1.3 Calculation for thermodynamic equilibrium 71
3.2 Results and discussion 72
3.2.1 Material characterization 72
3.2.2 Kinetics of dehydration and rehydration of ettringite 73
3.2.2.1 Temperature and mass effect on dehydration 73
3.2.2.2 Stepwise dehydration process 75
3.2.2.3 Rehydration enthalpy of meta-ettringite 78
3.2.3 Thermodynamic equilibrium 80
3.2.3.1 Dehydration of ettringite 80
3.2.3.2 Rehydration of ettringite 81
3.2.3.3 Thermodynamic equilibrium of hydration and dehydration 83
3.3 Conclusions 86
3.4 References 87

Chapter IV. Comparative kinetics study on carbonation of ettringite and meta-ettringite based materials 89

4.1 Materials and methods 91
4.1.1 Materials 91
4.1.2 Preparation of samples 91
4.1.3 Accelerated and natural carbonation methods 92
4.1.4 Characterisation methods 93
4.1.4.1 Thermal characterisation 93
4.1.4.2 XRD analysis 94
4.1.4.3 Theoretical CO_2 binding capacity by XRF 95
4.1.4.4 Granulometry 95
4.1.4.5 MIP analysis 95
4.1.4.6 Water isotherm absorption 96
4.2 Results 96
4.2.1 Characterisation of reference materials before carbonation 96
4.2.2 Carbonation results of three binders by TGA 98
4.2.3 Detailed carbonation results of C80P20 by TGA 100
4.2.4 Carbonation results of C80P20 by XRD 101
4.2.4.1 Accelerated carbonation at 50 % RH 101
4.2.4.2 Accelerated carbonation at 70 % RH 102
4.2.4.3 Accelerated carbonation under 90 % RH 103
4.2.5 Carbonation effect on TESC 104
4.3 Discussion 105
4.3.1 Pore size distribution vs. carbonation 105
4.3.2 Comparison of carbonation resistance for three binders 105
4.3.3 Effect of grain size on carbonation 106
4.3.4 Influence of RH 106
4.3.5 Influence of CO_2 concentration 107
4.3.6 Phase assemblage and reaction path 108
4.3.6.1 50 % RH results 108
4.3.6.2 70 % RH results 109
4.3.6.3 90 % RH results 110
4.3.7 TESC vs. CO_2 binding quantity 111

4.4 Conclusion 112

Chapter V. Characterization of an ettringite-based material in an open-mode reactor.....117

5.1 Experimental method 119
5.1.1 Material preparation 119
5.1.2 Thermal characterization 119
5.1.3 Reactor conception 119
5.1.4 Reactor test conditions 121
5.1.5 Data processing method 122
5.2 Results and discussion 124
5.2.1 Ettringite content by XRD 124
5.2.2 TGA-DSC analysis 124
5.2.2.1 Dehydration analysis 124
5.2.2.2 Hydration analysis 126
5.2.3 Reactor performance 128
5.2.3.1 Dehydration tests 128
5.2.3.2 Hydration tests 132
5.2.4 Comparison with other systems from the literature 137
5.3 Conclusions 138
5.4 References 140

Chapter VI. General conclusion and prospects.....141

6.1 Mains results obtained 142
6.2 Prospects 145
6.2.1 Understanding of thermal behaviors 145
6.2.2 Optimization of the composite material containing ettringite 145
6.2.3 Reactor experiments 146

Appendix 149

Chapter I. General introduction

1.1 Background of the energy challenge

In 2019, renewable energy and energy storage take two places in the "Top 10 emerging technologies" classified by the World Economic Forum [1] due to the global energy and climate challenge. The Bloomberg New Energy Finance Report of 2019 [2] indicates that wind and solar will generate about 50 % of the world electricity in 2050 compared with only 10 % for now (Figure I-1). To respond to this increase, more than $10 trillion of new investment is required on renewable energies, which creates unprecedented opportunities and challenges.

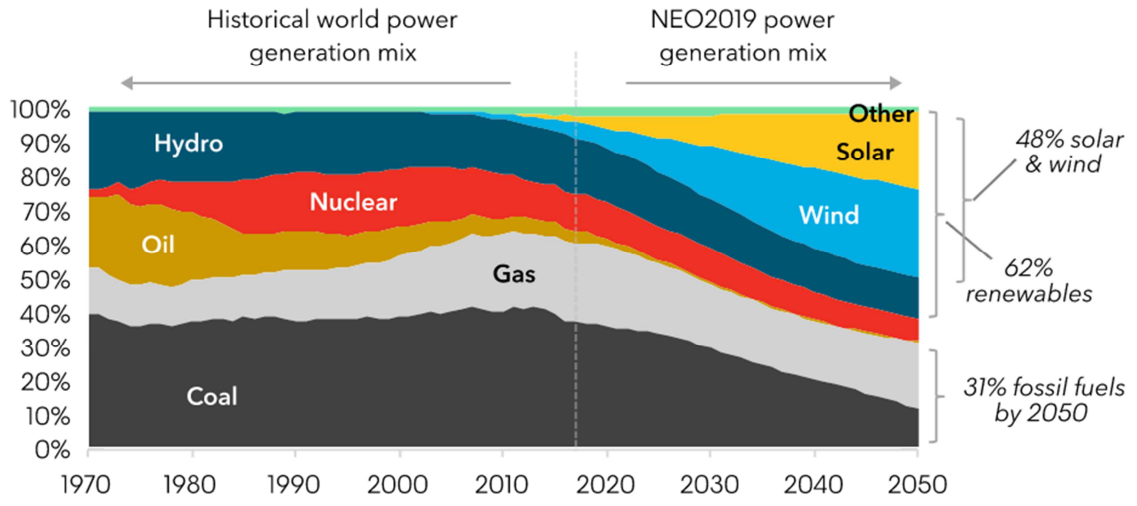

Figure I-1: Global power generation mix [2].

Early in 2009, the EU, as a global leader in advocating net-zero-greenhouse gas emissions, set its target to reduce emissions of 80–95% in 2050 compared to the 1990 levels [3]. At the French level, the "ADEME 2035-2050" strategy commits, by 2050, the final demand of original renewable energy increasing to 46–69 % and reducing 70–72 % equivalent carbon dioxide emission compared to 2010 levels [4]. Therefore, the growing energy demand expected in the next decades and the global awareness about the climate changes lead to new challenges in terms of energy conservation and energy use efficiency.

As to the global demand in Europe, 27 % of the final energy is consumed by households, with space heating accounting for 64 % of final energy consumption in the residential sector [5]. In France by 2018, the final energy consumption of residential buildings represented 28.5 % of total final energy consumption, of which 78 % owes to heating and domestic hot water by about 90 % of CO_2 emissions in the residential buildings [6,7]. It is therefore necessary to

implement various solutions to meet the heat consumption as well as decrease greenhouse gas emissions.

Taking into account the accessibility of resources, solar energy is one of the most potential renewable energy to use for European families (see examples for some cities in France, Table I-1). The integrated solar energy system in individual houses and residential buildings for heating is one of the key solutions to rationalize energy management. However, due to the temporal unbalance between solar supply and thermal energy demand (Figure I-2), it can be interesting to exploit the excess of solar energy by carrying out storage for later heating use as for daily and long-term demand [8].

Table I-1: Accessible solar resources in main French cities [9].

City	Solar radiation[kWh/(m^2·day)]
Paris	3.22
Lyon	3.62
Marseille	4.82
Nice	4.57
Lille	3.20
Strasburg	3.28
Nantes	3.62
Toulouse	4.55

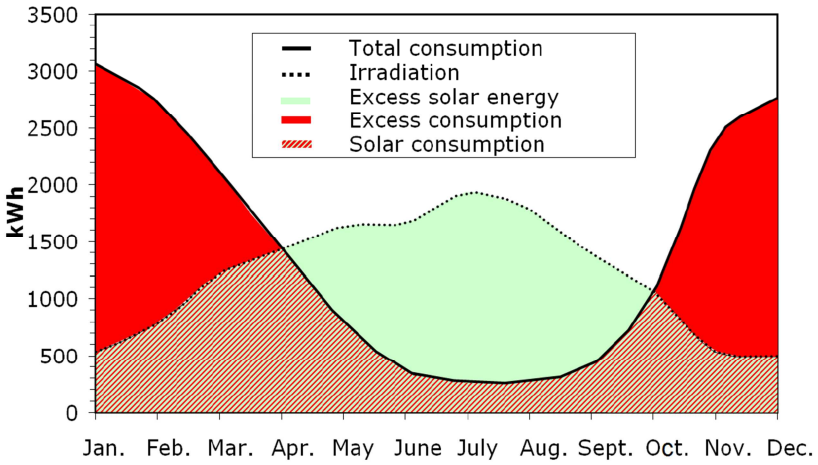

Figure I-2: The seasonal mismatch of between accessible solar energy and heating demand for a family [10].

Under such circumstances, thermal energy storage (TES), including sensible energy storage, latent energy storage, and sorption energy storage, is one of the most reasonable solutions to

rationalize the application of renewable energy by increasing the solar fraction in residential and commercial buildings sectors [11]. TES mainly concerns: 1) a near-term storage of solar energy during daytime for the use in the evening or early morning; 2) a seasonal storage of solar energy during summer to compensate for the over-consumption of thermal energy in winter for different scales (individual house, apartment, district, and city). For such novel solar technologies, the European targeted the effective storage density should be more than 300 kWh/m^3 materials [12].

1.2 TES technologies

In the TES research field, sensible heat and latent heat storage have been widely studied and are at an advanced stage of development presently. However, they are not supposed to be used for the near-term (daily) of high thermal energy demand or long-term energy storage not only for their low energy density but also the unavoidable heat dispersion.

1.2.1 Sensible heat storage

Sensible heat storage denotes a change in temperature of material without phase change and serves mainly in domestic hot water (DHW) and space heating, of which the temperature locates between 40 and 80 °C [13]. The storage medium stores heat through heat transfer by convection, conduction, and radiation. The quantity of stored sensible energy can be described by Equation I-1.

$$Q = \int_{T_1}^{T_2} mC_p dT$$

Equation I-1

where Q is the quantity of thermal energy stored, T_1 and T_2 are the work temperatures, m is the mass of the material, and Cp is its specific heat.

To respond to the temperature demand, the common materials used as heat storage mediums are water, rock materials (including gravel, bricks, pebble…), and soil in real-scale use projects [13]. Additionally, synthetic oil, liquid metals, molten salts, and concrete are used to store thermal energy of high temperature [14], especially in concentrated solar power plants. Table I-2 demonstrates the main characteristics of common sensible heat storage materials.

Table I-2: Several thermal properties of certain materials for low temperature sensible heat storage, extracted from [15].

Material	Thermal conductivity (W/mK)	Volumetric heat capacity (MJ/m^3)	Density (10^3 kg/m^3)
Clay/silt, dry	0.4–1.0	1.5–1.6	1.8–2.0
Clay/silt, water-saturated	1.1–3.1	2.0–2.8	2.0–2.2
Sand, dry	0.3–0.9	1.3–1.6	1.8–2.2
Sand, water-saturated	2.0–3.0	2.2–2.8	1.9–2.3
Gravel/stones, dry	0.4–0.9	1.3–1.6	1.8–2.2
Gravel/stones, water-saturated	1.6–2.5	2.2–2.6	1.9–2.3
Sandstone	1.9–4.6	1.8–2.6	2.2–2.7
Limestone	2.0–3.9	2.1–2.4	2.4–2.7
Water (+ 10 °C)	0.59	4.15	0.999

Water is the most common medium and heat carrier used for sensible heat storage. Water-based storage systems are usually categorized as water tank systems and aquifer storage systems. Water tanks combined with solar collectors are installed on the roof for the daily use of single-family or buried underground due to their large volume for collective use. In the UK, a tower tank storing 2500 tons of water (at just below 100°C, equals 18 MWh of heat) can meet the space heating and DHW demand of 3256 homes, 50 commercial properties, and 3 schools [16]. Aquifer storage directly uses underground water via thermal (cold and hot) wells. Good knowledge of the mineralogy, geochemistry, and microbiology of the subsoil is essential for this type of installation. The temperature of aquifer heat storage ranges from 10 to 20 °C. Less frequently, some projects reported that the storing temperature could reach up to 70 °C [17].

Differing from water, rock-sort materials, being compacted as a bed, need a heat carrier (air or water) to transfer the heat stored. This kind of system can permit higher temperatures compared to water-based systems but with a low energy density due to much lower heat capacity. A representative project of a pebble bed of 300 m^3 was investigated in China to store the surplus heat produced by solar collectors for supplying space heating and DHW during the night [18].

Ground or soil sensible heat storage, also named as borehole thermal energy storage (BTES) or duct heat storage, is constructed by vertical or horizontal tubes inserted into the ground. The surplus solar energy in summer is stored by a U-tube heat exchanger. This type of storage

requires a volume 3 to 5 times bigger than a water-based system [19]. At Drake Landing Solar Community of Canada, a BTES equipping with 144 boreholes (37 m of depth) stores solar thermal energy from 52 homes to meet about 97% of year-round heat [20].

Referring to high-temperature thermal energy storage, working temperature usually excesses 450 °C to keep heat from a concentrating solar power (CSP) plant. Most constructed CSP plants with TES use molten salt mixtures as thermal energy storage materials, such as $NaNO_3$-KNO_3 for "Solar Salt", $NaNO_2$-KNO_3-$NaNO_3$ for "Hitec" and $Ca(NO_3)_2$-KNO_3-$NaNO_3$ for "HitecXL" [21]. These nitrates and nitrites are only suitable for storage temperatures below 600 °C [22]. Instead of salts, a recent investigation [23] demonstrates a concrete to store heat resources at temperatures up to 380 °C. For higher operating temperatures, carbonates salts, fluoride salts, chloride salts, mixed-anion salts, and liquid alkali metals are supposed to be very useful [24].

1.2.2 Latent heat storage

Latent heat storage is to store thermal energy at a constant temperature by the phase change of media. Thus, the used mediums are called phase change materials (PCM). Most common phase changes related to solid-liquid and liquid-vapor and the quantity of heat stored (Q) corresponds to the specific latent enthalpy change (see Equation I-2):

$$Q = m \cdot \Delta H_{fusion} \text{ or } m \cdot \Delta H_{vap}$$

Equation I-2

Where m is the mass of medium and ΔH is the enthalpy change for fusion or vaporization.

The PCMs can be classified as inorganic PCMs and organic PCMs according to chemical properties. Among the inorganic PCMs, ice is mostly used with a long history. Besides, several slat hydrates, like $Na_2SO_4 \cdot 10H_2O$, $Na_2SiO_3 \cdot 5H_2O$, $NaCl \cdot Na_2SO_4 \cdot 10H_2O$, are also reported to be used for thermal energy storage [25]. As for organic materials, low-cost paraffin is the most common PCM used in the building section [26] due to their moderate TES density by latent heat. However, the low thermal conductivity (0.21 to 0.24 W / (m·K)) enforced a large surface area [27,28]. The expanded graphite [29], Kaolin [30], and aluminosilicate clay mineral (Kaolin-like) [31] could enforce the heat transfer rate of paraffin up to 0.89 W / (m·K) with different mass fractions of graphite [30,32]. Frequently, paraffin is packaged in small beads and plastic bags to be integrated into walls in order to minimize the interior tem-

perature changes [26]. Apart from paraffin, esters, fatty acids, alcohol, and glycol compounds for energy storage [27], but 2–2.5 higher in material cost. Besides, two or more PCMs could be mixed in moderate quantity to form a minimum melting eutectic PCM without segregation during the recrystallization. Some eutectic PCMs are presented in Table I-3. These materials usually promise better thermal performance than the single component in the eutectic.

Table I-3: Several inorganic and organic eutectic PCMs, reproduced from [27].

Material	Mass fraction (wt.%)	Melting temperature (°C)	Latent heat (kJ/kg)
$CaCl_2 \cdot 6H_2O + CaBr_2 \cdot 6H_2O$	45 + 55	14.7	140
$C_{14}H_{28}O_2 + C_{10}H_{20}O_2$	34 + 66	24	147.7
$Ca(NO_3)_2\ 4H_2O + Mg(NO_3)_2 \cdot 6H_2O$	47 + 53	30	136
$CH_3COONa \cdot 3H_2O + NH_2CONH_2$	40 + 60	30	200.5
$LiNO_3 + NH_4NO_3 + NaNO_3$	25 + 65 + 10	80.5	113
$CH_3CONH_2 + C_{17}H_{35}COOH$	50 + 50	65	218
Napthalene + benzoic acid	67.1 + 32.9	67	123.4
Triethylolethane + water + urea	38.5 + 31.5 + 30	13.4	160

However, the enthalpy of phase change in a short period, the flammability for most organic PCMs, and also the instability of volume that causing mechanic problems often obstruct their use in the building sector. In addition, the low energy density given by the PCMs (several tens kWh/m^3) results in a very big volume to integrate into buildings.

1.2.3 Heat storage by sorption

Sorption in TES refers to the process that a substance attaches to another. It usually occurs in a heterogeneous (sorbent/sorbate) system, for two phases or more. Depending on the interaction forces, TES sorption can be classified as physical sorption (by Van der Waals force and hydrogen bond) and chemical sorption (by orbital overlap and charge transfer between atoms). Moreover, chemical sorption needs activation energy to excite the process while being contrast for the former one [33].

The whole TES physical/chemical sorption cycle depends on the temperature (T) and gas partial pressure (P) [34], presented in Figure I-3. The storage and release for a TES sorption can be multistep which contains several equilibriums. The material is originally at the state $X_{eq,1}$

(hydrated). To store the first part of the energy, the heat $Q_{in}$is transferred to the sorbent to desorb the sorbate at T_{in} to arrive at the state $X_{eq,2}$. If a follow-up heat Q_{in}^{n} is given at T_{in}^{n}, the material could transform into the state $X_{eq,n}$. Theoretically, the multistep can be merged into a single process ($X_{eq,n}$) if the desorption condition directly is at T_{in}^{n} and P_c. The material then could be stored under the conditions at the right zone of equilibrium $X_{eq,n}$ without losing any energy for a certain period. At releasing date, same as desorption, the sorption of sorbate on/into the sorbent (at the state $X_{eq,n}$) occurs only under the equilibrium conditions (T_{out}^{n} and P_e) for the discharging heat of Q_{out}^{n} until the temperature down to the equilibrium $X_{eq,1}$ at T_e accompanying with total heat amount of $Q_{out} + Q_{out}^{n}$. The physical sorption and a part of chemical sorption could be simplified as a single process that occurs only between the state $X_{eq,1}$and $X_{eq,2}$.

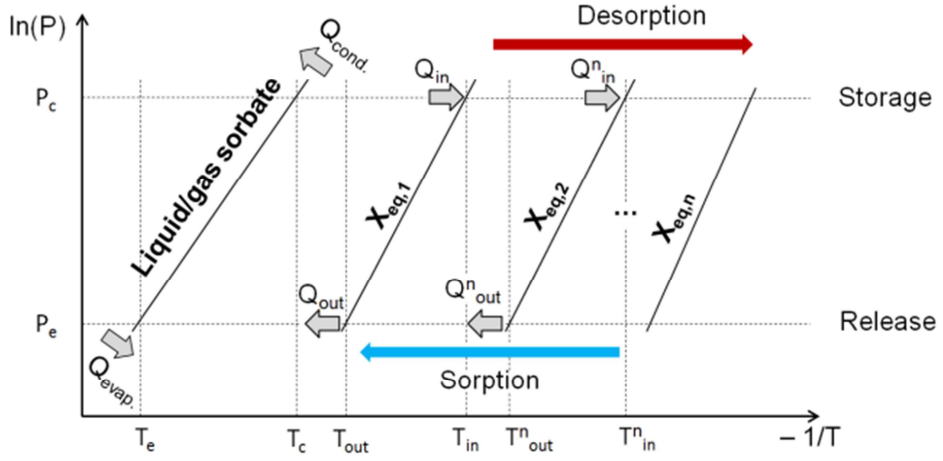

Figure I-3: Theoretical Clausius–Clapeyron sorption cycle, reproduced from [34].

In the literature, the most studied physical sorption materials for TES are silica gel and zeolite [35,36] with water vapor sorbate. Silica gel is a porous silicon dioxide material of high specific surface area from 600 to 800 m^2/g [34]. After sorption, silica gel can easily desorb water vapor at 120 °C in a few hours. However, its energy storage capacity is very limited at about 42 kWh/m^3 [37]. As same as silica gel, zeolite is also a very porous material of different kinds, like type A, X, and Y. Among them, zeolite X has a bigger porosity and higher affinity [34] which results in a good experimental energy storage capacity of 104 kWh/m^3 (zeolite 13X) [35]. Such materials could even release heat at a low water vapor partial pressure.

As for the chemical storage methods, the charging and discharging of heat is by a reversible solid/water vapor reactions: A_xB_y (s) + heat ↔ A_xB_{y-z} (s) + zB (g), x, y, z ≠ 0. Unlike conventional sensible and latent heat storage, the neglecting heat loss guarantees all heat stored. The

typical heat storage materials, that relies on a reversible chemical reaction without sorption, could be oxide-hydroxide ($MgO/Mg(OH)_2$ [39] and $CaO/Ca(OH)_2$ [40–43]), oxide-carbonate ($CaO/CaCO_3$ [38]), reduction/oxidation ($(Mn_{0.75}Fe_{0.25})_2O_3/(Mn_{0.75}Fe_{0.25})_3O_4$ [44] and CoO/Co_3O_4 [45,46]), usually possesses high energy densities under harsh experimental conditions (high operating temperatures, high pressures, and reactants of high purity). These materials are said not suitable for the local applications in the buildings since the available heat from solar energy remains below 150 °C.

The working temperature of thermochemical sorption energy storage (TCES) could be lower than this limit in reactors: such concept is then adaptable to households. The salt hydrates provide a relatively higher theoretical energy density and a long shelf life without heat dissipation since no reaction occurs during storage. Zondag et al. [47] reported a generated thermal power of 150 W (~ 139 kWh/m^3) in order to heat air from 50 to 64 °C by a 17 dm^3 of initial $MgCl_2 \cdot 6H_2O$ material in a packed bed open reactor system. Besides, they also indicated a loss of about 2/3 power to the exit airflow due to the inefficient heat recovery. Later, N'Tsoukpoe et al. [48] evaluated the suitability of 125 salt hydrates and concluded the most promising salt hydrates used for thermochemical energy storage are $MgSO_4 \cdot 7H_2O$, $SrBr_2 \cdot 6H_2O$, and $LaCl_3 \cdot 6H_2O$. Michel et al. [49] experimented with an open mode reactor with 400 kg of $SrBr_2 \cdot 6H_2O$ and obtained a high energy density of 203 kWh/m^3 with a storage capacity of 105 kWh. Zhao et al. [50] exploited an $SrBr_2$ sorbent composited of expanded natural graphite treated with sulfuric acid to store heat at 80 °C. The releasing thermal storage density was about 189 kWh/m^3 composite materials with a discharging power of 91 W/kg composite sorbent. In order to increase the permeability of packed bed, Hongois et al. [51] developed a $MgSO_4$ (15 wt%)-zeolite composite that possessed an energy density of 166 kWh/m^3 released at 25 °C in a packed bed reactor with 200 g of sorption material.

Although all above TCES investigations give interesting and promising results of using salt hydrates to store thermal energy, the techniques are still at the initial phase. Nevertheless, material selection is always a critical point in the development of thermochemical energy storage. N'Tsoukpoe et al. proposed the following 10 criteria need to be considered [48]:

- ✓ High energy density
- ✓ Low material cost
- ✓ Discharging in usable temperature conditions
- ✓ Regeneration temperature as low as possible

- ✓ Non-corrosiveness
- ✓ Environmentally friendly
- ✓ High specific power (affinity of the sorbent for the sorbate, thermal conductivity, etc.)
- ✓ Moderate operating pressure range
- ✓ Cyclability and stability
- ✓ Sustainability

With respect to this guidance, the salt hydrates in Table I-4, being promising in energy density, may be integrated into thermal energy storage systems with solar collectors thanks to the low dehydration temperatures. However as being soluble salts, the said promising candidates risk the over-hydration during the discharging and form a saturated solution, which may corrode the equipment of storage systems and cause security problems. Besides, the material costs of the three salt hydrates are too high to be applied in residential buildings and individual houses [52]. It may be an essential obstacle hindering the development of the energy storage market.

Table I-4: Comparison of the most promising salt hydrates for TES [48,53,54].

Material	Theoretic energy density (kWh/m^3)	Material cost ($€/m^3$)	Dehydration temperature (°C)
$MgSO_4 \cdot 7H_2O/MgSO_4 \cdot H_2O$	639	4 870	150
$SrBr_2 \cdot 6H_2O/SrBr_2 \cdot H_2O$	628	42 000	80
$LaCl_3 \cdot 7H_2O/LaCl_3 \cdot H_2O$	591	38 400	100

1.3 New candidate for TCES

As being difficult to satisfy all criteria [48], compromised materials are thus suggested to be used in thermal energy storage systems. Some investigations [55–57] on a cement-based mineral, ettringite ($3CaO \cdot Al_2O_3 \cdot 3CaSO_4 \cdot 32H_2O$), shows its potentiality for TES. Referring to the guidance of material choice, the high energy density of ettringite (more than 500 kWh/m^3) is quite competitive with the three salt hydrates in Table I-4. The low working (dehydration) temperature of 60–65 °C [55] makes it even possible to store solar energy during the sunny days in winter without mentioning in summer. As being a mineral, it is insoluble in water, which avoids the very risky over-hydration and corrosiveness for the equipment. Moreover, ettringite is non-toxic, non-explosive, and non-flammable, which promotes its safety in experimental study and applications. As a common component in hydrated cement, the material

cost of ettringite (< 1000 €/m^3) is much lower than that of the three most promising salts, zeolite 13X (2 000–3 000 €/m^3), and Silica gel (4 300 €/m^3) [53]. In addition, ettringite could be produced easily in very large quantities and almost everywhere in the world for cementitious compounds containing ettringite. Therefore, it may be a solution to enlarge the potential market of solar thermal energy storage. Up to now, ettringite has been widely studied for its performances in construction like delayed ettringite formation [58] and expansion phenomena [59,60], but less known, as a thermochemical material. Thus, Chapter 2 addresses a review on the physical and chemical properties of ettringite in order to discuss its potentiality in thermal energy storage.

1.4 General layout of the thesis

The thesis is composed by results presented in peer reviewed papers published, or submitted. The chapters shown in this thesis are organized to respond the objectives of the thesis which are going to be presented in **Chapter 2**.

Chapter 2 presents the bibliographic synthesis of the physicochemical properties of ettringite for thermal storage, including ettringite synthesis method, crystal structure, thermal stability and carbonation durability. The existing adapted prototypes for ettringite materials are equally summarized. With the study of research review, several research direction also as the objectives of the thesis are proposed.

Chapter 3 reports the experimental results on the thermodynamics, kinetics, enthalpies of reactions, and stepwise reaction mechanism between different hydration states of synthetic ettringite and meta-ettringite at various partial water vapor pressure and temperatures.

By **Chapter 4**, the carbonation resistance of three ettringite enriched materials has been investigated. The energy storage capacity of the most CO_2 resistant material is also given at different carbonation degree.

Chapter 5 describes the dehydration and hydration kinetics of the selected ettringite-based material in Chapter 4. The reactor energetic performance is also examined in an adapted fixed-bed prototype in open-mode.

Chapter 6 concludes the most important outcomes of this thesis work about the advancement of using ettringite materials for thermal energy storage. Besides the perspectives for future researches on the ettringite materials are proposed.

1.5 References

[1] World Economic Forum. Top 10 Emerging Technologies 2019. 2019.

[2] BloombergNEF. New Energy Outlook 2019. 2019.

[3] European Commission. A clean planet for all - A European long-term strategic vision for a prosperous , modern , competitive and climate neutral economy. Brussels: 2018.

[4] ADEME. Actualisation du scénario énergie-climat 2035–2050 en France. 2017.

[5] Eurostat. Energy consumption in households. 2019.

[6] Production LA et al. Commissariat général au développement durable Bilan énergétique de la France en 2018 Données provisoires 2019.

[7] Les émissions de CO_2 liées à l'énergie en France de 1990 à 2018 - Facteurs d'évolution et éléments de comparaison internationale 2019.

[8] Hongois S et al. Development and characterisation of a new $MgSO_4$−zeolite composite for long-term thermal energy storage. Sol Energy Mater Sol Cells 2011;95:1831–7.

[9] National Renewable Energy Laboratory. NREL's PVWatts Calculator, 2020. https://pvwatts.nrel.gov/ (access on 22 May 2020).

[10] Zondag, A H. Seasonal and daily heat storage for heating & cooling of buildings, 2012. http://www.concreteheat.com/downloads/ (access on 21 May 2020).

[11] Stutz B et al. Storage of thermal solar energy. Comptes Rendus Phys 2017;18:401–14.

[12] Stryi-Hipp G et al. Strategic research priorities for solar thermal technology. 2012.

[13] Xu J et al. A review of available technologies for seasonal thermal energy storage. Sol Energy 2014;103:610–38.

[14] Kuravi S et al. Thermal energy storage technologies and systems for concentrating solar power plants. Prog Energy Combust Sci 2013;39:285–319.

[15] VDI Guideline VDI 4640. Thermal use of the underground – Fundamentals, approvals, environmental aspects. Beuth-Verlag Berlin: 2010.

[16] Eames, P., Loveday, D., Haines, V. and Romanos P. The future role of thermal energy storage in the UK energy system: An assessment of the technical feasibility and factors influencing adoption. London: 2014.

[17] Sanner B et al. Underground thermal energy storage for the German Parliament in Berlin, system concept and operational experiences. Proc World Geotherm Congr Antalya 2005:paper 1438, 1-8.

[18] Zhao DL et al. Optimal study of a solar air heating system with pebble bed energy

storage. Energy Convers Manag 2011;52:2392–400.

[19] Rad FM, & Fung AS. Solar community heating and cooling system with borehole thermal energy storage–Review of systems. Renew Sustain Energy Rev 2016;60:1550–61.

[20] Mesquita L et al. Drake Landing solar community: 10 years of operation. ISES Sol World Congr 2017 – IEA SHC Int Conf Sol Heat Cool Build Ind 2017, Proc 2017:333–44.

[21] Gil A et al. State of the art on high temperature thermal energy storage for power generation. Part 1 – Concepts, materials and modellization. Renew Sustain Energy Rev 2010;14:31–55.

[22] Stern KH. High temperature properties and decomposition of inorganic salts Part 3, nitrates and nitrites. J Phys Chem Ref Data 1972;1:747–72.

[23] Hoivik N et al. Long-term performance results of concrete-based modular thermal energy storage system. J Energy Storage 2019;24:100735.

[24] Mohan G et al. Sensible energy storage options for concentrating solar power plants operating above 600 °C. Renew Sustain Energy Rev 2019;107:319–37.

[25] Sharma SD, & Sagara K. Latent heat storage materials and systems: A review. Int J Green Energy 2005;2:1–56.

[26] Kuznik F et al. A review on phase change materials integrated in building walls. Renew Sustain Energy Rev 2011;15:379–91.

[27] Sharma A et al. Review on thermal energy storage with phase change materials and applications. Renew Sustain Energy Rev 2009;13:318–45.

[28] Farid MM et al. A review on phase change energy storage: Materials and applications. Energy Convers Manag 2004;45:1597–615.

[29] Zhang Z, & Fang X. Study on paraffin/expanded graphite composite phase change thermal energy storage material. Energy Convers Manag 2006;47:303–10.

[30] Lv P et al. Experiment study on the thermal properties of paraffin/kaolin thermal energy storage form-stable phase change materials. Appl Energy 2016;182:475–87.

[31] Zhang J et al. Preparation and thermal energy properties of paraffin/halloysite nanotube composite as form-stable phase change material. Sol Energy 2012;86:1142–8.

[32] Sarı A, & Karaipekli A. Thermal conductivity and latent heat thermal energy storage characteristics of paraffin/expanded graphite composite as phase change material. Appl Therm Eng 2007;27:1271–7.

[33] Kuznik F, & Johannes K. Thermodynamic efficiency of water vapor / solid chemical

sorption heat storage for buildings: theoretical limits and integration considerations. Appl Sci 2020;10:489.

[34] Kuznik F et al. A review on recent developments in physisorption thermal energy storage for building applications. Renew Sustain Energy Rev 2018;94:576–86.

[35] Johannes K et al. Design and characterisation of a high powered energy dense zeolite thermal energy storage system for buildings. Appl Energy 2015;159:80–6.

[36] Zettl B et al. Development of a revolving drum reactor for open-sorption heat storage processes. Appl Therm Eng 2014;70:42–9.

[37] Deshmukh H et al. Study of sorption based energy storage system with silica gel for heating application. Appl Therm Eng 2017;111:1640–6.

[38] Ortiz C et al. The Calcium-Looping ($CaCO_3$/CaO) process for thermochemical energy storage in concentrating solar power plants. Renew Sustain Energy Rev 2019;113:109252.

[39] Mastronardo E et al. Strategies for the enhancement of heat storage materials performances for $MgO/H_2O/Mg(OH)_2$ thermochemical storage system. Appl Therm Eng 2017;120:626–34.

[40] Criado YA et al. Conceptual process design of a $CaO/Ca(OH)_2$ thermochemical energy storage system using fluidized bed reactors. Appl Therm Eng 2014;73:1087–94.

[41] Yan J, & Zhao CY. Experimental study of $CaO/Ca(OH)_2$ in a fixed-bed reactor for thermochemical heat storage. Appl Energy 2016;175:277–84.

[42] Schmidt M, & Linder M. Power generation based on the $Ca(OH)_2$/CaO thermochemical storage system – Experimental investigation of discharge operation modes in lab scale and corresponding conceptual process design. Appl Energy 2017;203:594–607.

[43] Yuan Y et al. $CaO/Ca(OH)_2$ thermochemical heat storage of carbide slag from calcium looping cycles for CO_2 capture. Energy Convers Manag 2018;174:8–19.

[44] Wokon M et al. Investigations on thermochemical energy storage based on manganese-iron oxide in a lab-scale reactor. AIP Conf Proc 2017;1850:200–14.

[45] Singh A et al. Solar thermochemical heat storage via the Co_3O_4/CoO looping cycle: Storage reactor modelling and experimental validation. Sol Energy 2017;144:453–65.

[46] Neises M et al. Solar-heated rotary kiln for thermochemical energy storage. Sol Energy 2012;86:3040–8.

[47] Zondag H et al. Prototype thermochemical heat storage with open reactor system. Appl Energy 2013;109:360–5.

[48] N'Tsoukpoe KE et al. A systematic multi-step screening of numerous salt hydrates for low temperature thermochemical energy storage. Appl Energy 2014;124:1–16.

[49] Michel B et al. Experimental investigation of an innovative thermochemical process operating with a hydrate salt and moist air for thermal storage of solar energy: Global performance. Appl Energy 2014;129:177–86.

[50] Zhao YJ et al. Development of $SrBr_2$ composite sorbents for a sorption thermal energy storage system to store low-temperature heat. Energy 2016;115:129–39.

[51] Hongois S et al. Development and characterisation of a new $MgSO_4$-zeolite composite for long-term thermal energy storage. Sol Energy Mater Sol Cells 2011;95:1831–7.

[52] Chen B et al. Physicochemical properties of ettringite/meta-ettringite for thermal energy storage: Review. Sol Energy Mater Sol Cells 2019;193:320–34.

[53] Cabeza LF et al. Review on sorption materials and technologies for heat pumps and thermal energy storage. Renew Energy 2017;110:3–39.

[54] N'Tsoukpoe KE et al. The concept of cascade thermochemical storage based on multimaterial system for household applications. Energy Build 2016;129:138–49.

[55] Baquerizo LG et al. Impact of water activity on the stability of ettringite. Cem Concr Res 2016;79:31–44.

[56] Ings JB, & Brown PW. An evaluation of hydrated calcium aluminate compounds as energy storage media. NASA STI/Recon Tech Rep N 1982;83.

[57] Struble LJ, & Brown PW. Heats of dehydration and specific heats of compounds found in concrete and their potential for thermal energy storage. Sol Energy Mater 1986;14:1–12.

[58] Stark J, & Bollmann K. Delayed ettringite formation in concrete. Nord Concr Res 2000;23:4–28.

[59] Cohen MD. Theories of expansion in sulfoaluminate - type expansive cements: Schools of thought. Cem Concr Res 1983;13:809–18.

[60] Bizzozero J et al. Expansion mechanisms in calcium aluminate and sulfoaluminate systems with calcium sulfate. Cem Concr Res 2014;56:190–202.

Chapter II. Review on physicochemical properties of ettringite/meta-ettringite

Based on Publication 1:

Physicochemical properties of ettringite/meta-ettringite for thermal energy storage: Review

B. Chen[a,b] , F. Kuznik[a], M. Horgnies[b], K. Johannes[a], V. Morin[b], E. Gengembre[b]

[a] *Université de Lyon, CNRS, INSA-Lyon, Université Claude Bernard Lyon 1, CETHIL UMR 5008, F-69621 Villeurbanne, France*

[b] *LafargeHolcim R&D, 95 rue du Montmurier BP15, 38291 Saint Quentin Fallavier, France*

The review presented in this chapter was published in *Solar Energy Materials and Solar Cells*, 2019, 193, 320-334.

2.1 Introduction

Ettringite, of which chemical formula is $3CaO{\cdot}Al_2O_3{\cdot}3CaSO_4{\cdot}32H_2O$, or $C_6A\bar{S}_3H_{32}$ as known in cement chemistry notation, is also named as calcium trisulfoaluminate hydrate or AFt in whose group ettringite is one of the most important members. It has a lower density (~ 1.77 $g{\cdot}cm^{-3}$) and contains more water (~ 46%) than any other cement-based hydrates. The modulus and the hardness (in-press rigidity) of ettringite are respectively 20.07 GPa and 0.61 GPa [1]. Ettringite crystals are hexagonal prisms, often elongated with different shapes: needle-like (most general), lath-like, or rod-like [2]. After the first report on natural ettringite [3], the successful synthesis of high-purity ettringite and its extensive existence in cementitious hydrates announce the possibility for large use. Natural perfect ettringite is transparent but often "colored" by the presence of impurity of metal elements while synthetic ettringite is a white powder. However, they share the same composition and the same crystal phase structure excepting little variation of water content. Most researches mainly reported ettringite as a building material until a new application as used for thermal energy storage proposed by Ings and Brown [4]. Based on the reported thermal properties in [5,6], ettringite appeared to be a promising material for heat (or cold) storage solutions. Although some advancement has been made in the research of ettringite, such as thermal stability, reversibility [5–7], certain conclusions about the dehydration process [7–9] and enthalpy [5–7] were not exactly identical.

Same as other salt hydrates [10–13], the principal thermochemical operation on ettringite is based on a reversible process with mass change on water (*Equation II-1*):

$$3CaO \cdot Al_2O_3 \cdot 3CaSO_4 \cdot 32H_2O + heat \leftrightarrow 3CaO \cdot Al_2O_3 \cdot 3CaSO_4 \cdot XH_2O + (32 - X)H_2O$$

Equation II-1

Where X ($\neq 0$) is the number of residual water in per phase. During charging cycles, supplied heat from multiple sources, such as solar energy, urban heat system or industrial waste heat, makes ettringite dehydrated to meta-ettringite (partially decomposed phase of ettringite, $3CaO{\cdot}Al_2O_3{\cdot}3CaSO_4{\cdot}XH_2O$) and transferred thermal energy to chemical energy.

For instance, in a single-family house, thermal energy storage using ettringite can be used in summer when solar energy is abundant enough to be collected and transferred as a useful heat resource (*Figure II-1*). Evacuated tube solar air collectors on the roof can provide hot air of high temperature (more than 120 °C) that could easily dehydrate ettringite thanks to the low temperature of dehydration reaction (~ 60 °C) [7]. The higher the temperature of hot air, the bet-

ter the performance of the system and more heat is stored. Moreover, this material is also compatible with existing hot water solar collectors in individual houses as long as a heat exchanger can be installed in the material container. Hot water from solar collector, which temperature could be as high as 100 °C, is therefore supposed to readily withdraw water molecules of ettringite. This good suitability promises the possibility of reducing the installation cost of a solar system for civil heating use.

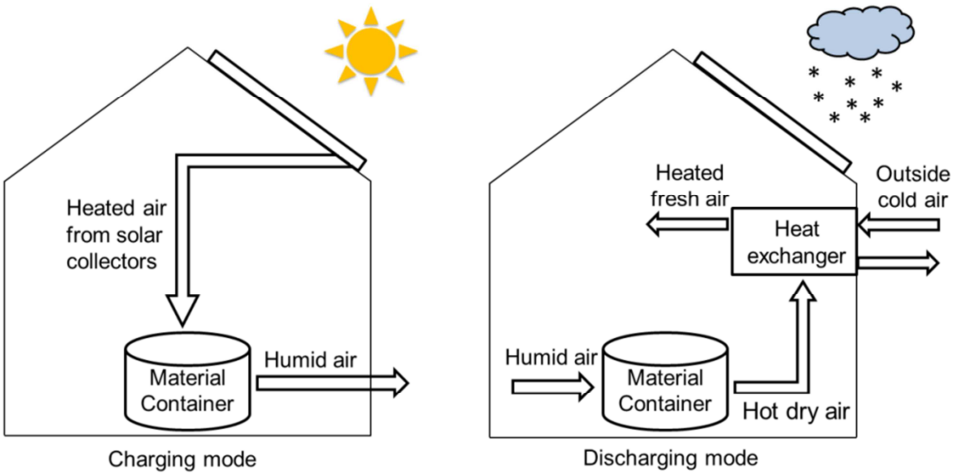

Figure II-1: A possible concept of charging mode (left) and discharging mode (right) of solar thermal energy storage by ettringite materials for a single-family house basing on [10].

Contrary to dehydration, the addition of water (liquid or vapor) on meta-ettringite recrystallizes ettringite and releases the stored energy (chemical energy → thermal energy). The required water vapor can be from inside or outside humid air and generated humid air, of which relative humidity (RH) should be superior to 60% [7]. The released heat of hydration depends strongly on the number of removed water per phase referring to X in *Equation II-1*, typically 1074.1 kJ/mol for 13-hydrate meta-ettringite (Met13, $3CaO{\cdot}Al_2O_3{\cdot}3CaSO_4{\cdot}13H_2O$) and 1316.1 kJ/mol for Met9 ($3CaO{\cdot}Al_2O_3{\cdot}3CaSO_4{\cdot}9H_2O$) by hydration with water vapor [7]. Then produced hot dry air is used to heat fresh cold air from outside through a mechanical heat recovery heat exchanger, which delivers heating to the house [1].

Additionally, recent works [7,14–19] have demonstrated the interest of using certain ettringite-based materials to store heat by chemical processes in a building via solar collectors. Therefore, this review is intended to summarize and analyze the physical- and chemical properties of meta-ettringite/ ettringite for thermal energy storage, including phase structure, material preparation, thermal properties (dehydration and hydration), carbonation and phenomena of ion substitution.

2.2 Formation of ettringite

Ettringite is a rare mineral phase in nature, while it exists commonly and largely in cement paste. Almost all alumina sources, such as $Al(OH)_3$ gel, aluminum sulfate hydrate, C_3A, can be reactive to form ettringite crystals [8,20,21]: with the addition of some calcium and sulfate source, the desired compound can be obtained under agitation with enough water. Once nucleation of ettringite occurred, the growth of ettringite crystal could be very fast. The crystallization completes essentially in a few hours with a form of lath-like or needle-like [22].

2.2.1 Conversion based on solutions

In order to get pure ettringite, analytical grade reagents are recommended. The first step is to make a saturated $Ca(OH)_2$ solution by having an appropriate amount of fresh sintered CaO dissolved in some fresh decarbonized demineralized water (FDDW). After the stoichiometric addition of diluted $Al_2(SO_4)_3$ XH_2O solution (with FDDW) into the former $Ca(OH)_2$ solution which is cooled down in a fridge, the suspension needs to be well stirred for 3 hours for crystal growth as shown in *Equation II-2*. Once the produced compound is filtered in vacuum and washed by FDDW and ethanol, the powder sample is finally dried and stored in a desiccator (containing $CaCl_2$ saturated solution who gives about 35 % RH [23]). All the above operations are under the protection of N_2. Some investigators [6,24] suggested that the initial introduction of sugar in $Ca(OH)_2$ solution was preferable to increase its solubility of about 0.02 to 0.3 mol/l. This solution conversion method was similarly described in other reports [9,23,25,26] and only a trace of monosulfate or calcium carbonate has been detected in several separated studies [27–29].

$$Al_2(SO_4)_3 \cdot XH_2O + 6\,Ca(OH)_2 \leftrightarrow 3CaO \cdot Al_2O_3 \cdot 3CaSO_4 \cdot 32H_2O$$

Equation II-2

Where X = 14–18. $Ca(OH)_2$ and $Al_2(SO_4)_3{\cdot}XH_2O$ are used as CaO and Al_2O_3–SO_3 source respectively.

2.2.2 Conversion based on solids

Different from the solution conversion method, solid reactive oxides are the main precursor to synthesize ettringite. The preparation of these components could be long because of repeated-

ly on-going grinding and calcination until a fine powder. Moreover, a curing of several days for the hydration of cement compositions is necessary.

2.2.2.1 Ettringite conversed by CA or C_3A

CA and C_3A, which are prepared from the calcination of a stoichiometric mixture between Al_2O_3 and CaO (or $CaCO_3$), belong to active aluminates with different contents of calcium. Ettringite crystallizes in an aluminate-rich gel, which is a mixture of an appropriate amount of CaO (not for C_3A) and $CaSO_4 \cdot 2H_2O$ with sufficient FDDW. This process is strongly exothermic. After curing, ettringite samples can be vacuum-filtered under the protection of N_2. Main chemical reactions could be as in *Equation II-3* and Equation II-4 [30]:

$$CaO \cdot Al_2O_3 + 2\,CaO + 3\,CaSO_4 \cdot 2H_2O\ +\ 26\,H_2O \leftrightarrow 3CaO \cdot Al_2O_3 \cdot 3CaSO_4 \cdot 32H_2O$$

Equation II-3

$$3CaO \cdot Al_2O_3 + 3\,CaSO_4 \cdot 2H_2O\ +\ 26\,H_2O \leftrightarrow 3CaO \cdot Al_2O_3 \cdot 3CaSO_4 \cdot 32H_2O$$

Equation II-4

2.2.2.2 Ettringite conversed by $C_4A_3\overline{S}$

There are two different methods: direct and indirect to produce $C_4A_3\overline{S}$ [31]. It is possible to synthesize directly $C_4A_3\overline{S}$ from a stoichiometric mixture of $CaCO_3$, $CaSO_4 \cdot 2H_2O$ and Al_2O_3 at about 1200 °C while the second way is to sinter a mixture of C_3A, gypsum and $Ca(OH)_2$. These two methods have been proved successful to yield high purity $C_4A_3\overline{S}$. An intimate stoichiometric mixture of $C_4A_3\overline{S}$, $CaSO_4$ and $Ca(OH)_2$ is then prepared and hydrated with a water to solid (w/s) ratio of 0.6 using FDDW. After curing at certain conditions, very pure ettringite can be obtained. The hydration process is as *Equation II-5*:

$$4CaO \cdot 3Al_2O_3 \cdot SO_3 + 5\,CaSO_4 + 9\,Ca(OH)_2 + 87\,H_2O \leftrightarrow 3\,(3CaO \cdot Al_2O_3 \cdot 3CaSO_4 \cdot 32H_2O)$$

Equation II-5

Although these solid conversion processes are slow, they result in a product getting rid of other potential chemical impurities. Grusczscinski et al. [32] used commercial pure calcium aluminate sulfate ($C_4A_3\overline{S}$) phase and self-prepared C_3A respectively to synthesize ettringite powder. Zhou et al. [33] prepared a mixture of 0.02 moles of C_3A and 0.06 moles of

$CaSO_4 \cdot 2H_2O$ to react with excessive degassed, deionized water (w/s=11). After 10 days of agitation in a closed vessel, ettringite crystals of about 10–20 μm with traces of amorphous material were harvested. A similar preparation process was also reported with a higher w/s ratio of 20 [7]. Other compounds like $C_6A\bar{S}$ [34] and $C_{12}A_7$ [35] were equally described to obtain pure ettringite.

2.2.2.3 "Alumina, ferric oxide, monosulfate" transformation method

Monosulfate, chemical formula of $3CaO \cdot Al_2O_3 \cdot CaSO_4 \cdot nH_2O$ (n = 12–14), as a hydrate of Portland cement paste, is compound of C_3A, $CaSO_4$ (anhydrite) and water, only in different proportions compared with ettringite. Between these binomials, a mutual transformation can occur with the presence of C_3A (form monosulfate) while with excessive $CaSO_4$ to form ettringite phase (see *Equation II-6* and *Equation II-7*):

$$2\ (3CaO \cdot Al_2O_3) + 3CaO \cdot Al_2O_3 \cdot 3CaSO_4 \cdot 32H_2O + \ 4\ H_2O \leftrightarrow 3\ (3CaO \cdot Al_2O_3 \cdot CaSO_4 \cdot 12H_2O)$$

Equation II-6

$$3CaO \cdot Al_2O_3 \cdot CaSO_4 \cdot 12H_2O + 2\ CaSO_4\ (\text{excessive}) + 20\ H_2O \leftrightarrow 3CaO \cdot Al_2O_3 \cdot 3CaSO_4 \cdot 32H_2O$$

Equation II-7

With respect to this principle, Pan et al. [36] mixed self-prepared CA of high purity with CaO and $CaSO_4 \cdot 1/2H_2O$ by a ratio of w/s=4. After sealed curing of 7 days, pure monosulfate was available. Afterward, AFt could converse via deep hydration of monosulfate with water and excessive gypsum.

2.2.3 Mechanism of formation

Peng and Lou [37] described the relation between the evolution of ion concentration and the formation of ettringite by solid-phase analysis and ion concentration analysis in the aqueous phase. They thought the three above chemical processes had the same chemical mechanism: the minerals dissolved rapidly to produce Ca^{2+}, SO_4^{2-}, OH^-, and then a saturated solution of ettringite was prepared. These ions moved together under the effect of the ion concentration gradient (after nucleation of ettringite). Thus, ettringite crystals could be formed according to the three following steps (*Equation II-8* to*Equation II-10*):

$$AlO_2^- + 2\,OH^- + 2\,H_2O \rightarrow [Al(OH)_6]^{3-}$$

Equation II-8

$$2\,[Al(OH)_6]^{3-} + 6\,Ca^{2+} + 24\,H_2O \rightarrow \{Ca_6[Al(OH)_6]_2 \cdot 24H_2O\}^{6+}$$

Equation II-9

$$\{Ca_6[Al(OH)_6]_2 \cdot 24H_2O\}^{6+} + 3\,SO_4^{2-} + 2\,H_2O \rightarrow \{Ca_6[Al(OH)_6]_2 \cdot 24H_2O\} \cdot (SO_4)_3 \cdot 2H_2O$$

Equation II-10

Brown and LaCroix [38] concluded that the formation rate of ettringite based on C_3A was controlled by a diffusional process with the apparent activation energy of formation of 1 kcal/mol and probably a one-dimension growth to form a needle-like morphology. A liquid interlayer (zone of diffusion) was reported between the solid phase ($C_4A_3\bar{S}$) and the formed crystal of ettringite (Figure II-2) [39]. In this interlayer, whose thickness was dependent on the concentration of ions, a saturated solution of ettringite was created (Equation II-8 andEquation *II-9*). Ettringite then crystallized in the solution of high pH > 10.7 (Equation II-10). Grusczscinski et al. [32] confirmed this interspace by Scanning Electron Microscope (SEM) and ex-situ formation mechanism by the appearance of independent ettringite crystal from C_3A.

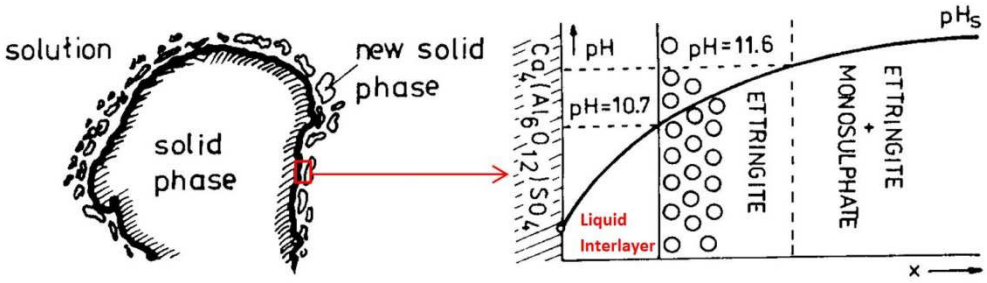

Figure II-2: The formation of ettringite based on C4A3$\bar{S}$ at pH > 10.7 [39]. Equation II-8 and Equation II-9 were supposed to carry out in the liquid interlayer while Equation II-10in the solution of high pH.

2.3 Crystal structure

2.3.1 Structure of ettringite crystals

Aluminum and calcium show respectively chemical valences of +3 and +2 when consist of binaries between Al-O and Ca-O. Based on this knowledge, Bannister et al. [40] on the first time proposed that the crystal structure is constructed on hexagonal (**a** = 11.24 ± 0.02 Å, **c** = 21.45 ± 0.05 Å, space group of D_{4h}^6 ($P6_3$/mmc) and Z=2) with the content of

$12CaO{\cdot}2Al_2O_3{\cdot}6SO_3{\cdot}64H_2O$ via X-Ray patterns for natural ettringite. Some "zeolitic" water molecules were predicted to locate in the channels which are parallel to the c-axis (0001) while aluminum atoms were hypothetically barred in $Al(OH)_6^{3-}$ octahedral groups. Other investigations on the structure of different ettringite crystals confirmed the lattice parameters with little variation due to the source of the specimen (Table II-1Where D is the density, Z-factor = 2, M is the molar mass of hydrate, V is the volume of unit cell calculated based on the lattice parameters from X-ray Diffraction (XRD) and N_A is the Avogadro constant.

Table II-1). Meanwhile, the specific gravities of ettringite ranged generally between 1.75 and 1.78 via the calculation by *Equation II-11*:

$$D = \frac{ZM}{N_A V}$$

Equation II-11

Where D is the density, Z-factor = 2, M is the molar mass of hydrate, V is the volume of unit cell calculated based on the lattice parameters from X-ray Diffraction (XRD) and N_A is the Avogadro constant.

Table II-1: Comparison for lattice parameters of ettringite from different localities

Locality	a (Å)	c (Å)	Specific density	References
Crestmore	22.33 / 2 = 11.165	21.35*	1.78	[41]
Ettringiten	22.48 / 2 = 11.24	21.31	1.762**	[41]
Scawt Hill	11.24	21.45	1.772	[40]
	11.23	10.75 × 2 = 21.50	1.750**	[42,43]
Kalahari Manganese Field	11.223 [a]	21.474 [a]	1.754 [a]	[20]
	11.229 [b]	10.732 [b] × 2 = 21.464	1.753 [b]	[20]
N'Chwanning mine	11.240	21.468	1.749**	[44]
	11.2530	21.6436	1.731**	[29]
Synthetic samples	11.167	21.360	1.9	[45]
	11.23	21.49	1.750**	[9]
	11.167	21.354	1.781**	[46]
	11.229	21.478	1.772**	[47]
	11.211–11.225 [c]	21.451–21.478 [c]	1.753–1.759**	[24]
	11.2220 [d]	21.4327 [d]	1.758**	[23]
	11.2129 [f]	21.4783 [f]	1.757**	[23]
	11.2514	22.6788	1.652**	[29]

* Ettringite from Crestmore contained a detectable amount of CO_2 [41], which therefore probably modified the lattice parameters.

** The parameters were doubled and the specific gravities were calculated with an assigned composition $Al_2O_3 \cdot 6CaO \cdot 3SO_3 \cdot 31H_2O$.

a: Supercell, special gravity calculated with an assigned composition $Al_2O_3 \cdot 6CaO \cdot 3SO_3 \cdot 31H_2O$.

b: Subcell, special gravity calculated with an assigned composition $Al_2O_3 \cdot 6CaO \cdot 3SO_3 \cdot 31H_2O$.

c: The values varied with the ratio of Ca/Al.

d: Dry ettringite (dried at 35% RH over saturated $CaCl_2$ solution).

f: Wet ettringite stored in the mother liquid of synthesis.

McConnell and Murdoch [48] pointed out the similarities in physical parameters between thaumasite and ettringite, and predicted that the structures of these crystals must be closely related. Yet Bezjak and Jelenic [49] thought the layers of Al-O and Ca-O polyhedral were perpendicular to the c-axis with little support from other investigations. Moore and Taylor [42] verified the space group of ettringite (*P*31c) and further proposed a detailed crystal structure: ettringite consists of column structure ($[Ca_6[Al(OH)_6]_2 \cdot 24H_2O]^{6+}$, per half of the unit cell) running parallel to **c** and channel components (SO_4^{2-} and H_2O). The core of the column structure is the aluminum oxide octahedron $[Al(OH)_6]^{3-}$ which is linked to three adjacent calcium atoms by bonds of Al-OH-Ca. The 8-coordinated Ca^{2+} ions are located in a polyhedral (probably a trigonal prism with two additional vertices) composed of four hydroxyls and four H_2O molecules (as shown in *Figure II-3*). This basic structure of ettringite (a nearly cylindrical shape) is oppositely twice the structure of columnar core along the longitudinal axis with a repeatable distance of 10.75 Å (about half of **c**-parameter) and a space group *P*31c.

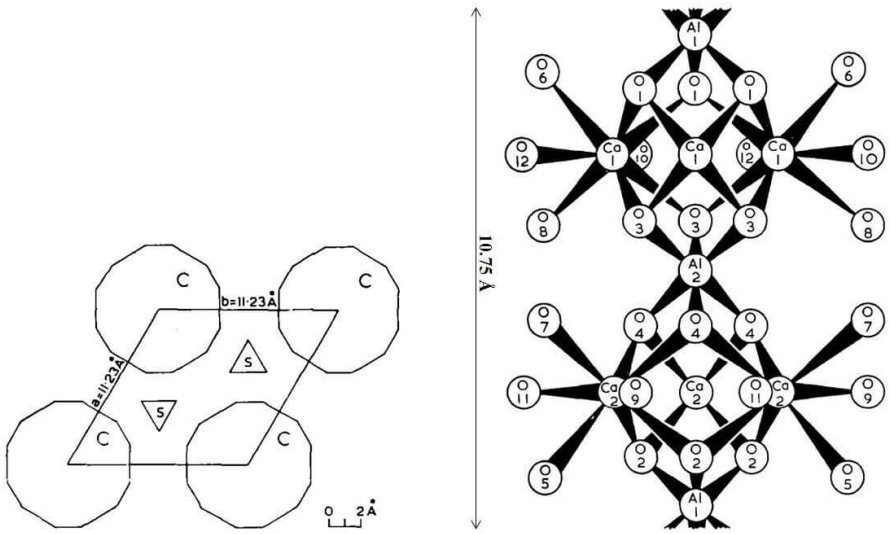

Figure II-3: Section of ettringite unit structure (left): the polygons and the triangles represent respectively the main columns structure ($[Ca_6[Al(OH)_6]_2 \cdot 24H_2O]^{6+}$) and SO_4^{2-} or H_2O groups in channels [50]. Basic unit crystal structure of ettringite in c-axis direction (right): the O represents OH or H_2O group, while Al and Ca atoms are showed by chemical symbols [43,50].

In the channels, three SO_4^{2-} ions and two water molecules ($[(SO_4)_3 \cdot 2H_2O]^{6-}$, per half of the unit cell) occur in four positions, of which the only one for $2H_2O$ group (0.25 possibilities). These components are supposed to be, at least, partially ordered. With the hypothesis of zero-twist between the sulfate tetrahedral and water groups, the arrangement for *P*31c is then inferred as $P6_3$ for ettringite crystals [43]. Moreover, the hydrogen bonds are considered as the liaisons between column structures and channel materials. The positive charge of column structure from Ca^{2+} and Al^{3+} ions is distributed among the H_2O molecule combine with Ca atoms, which means that the whole surface of the column is positively charged [43]. Therefore, every sulfate tetrahedral (negatively charged) interact with all the around columns to keep totally electrically neutral.

Berliner et al. [45] confirmed the basic column structure (*P*31c space group with **a** = 1.11670(5) nm and **c** = 2.13603(13) nm) and channel components proposed by Moore and Taylor [43] via the investigation of a synthetic ettringite by neutron powder diffraction techniques with a reactor-based instrument. Hartman and Berliner [46] synthesized an ettringite having deuterium in place of hydrogen and confirmed again the column structure of a synthetic ettringite was in the *P*31c space group (**a** ≈ 11.16 Å, **c** ≈ 21.35 Å) excepting that oxygen atoms were slightly shifted compared with [43]. The overall column structure based on Al- and Ca-polyhedral remained still unchanged. Renaudin et al. [23] indicated a small difference in lattice parameters between wet and dry ettringite. The crystal of ettringite was showed to become slightly shorter (~ 0.0182 Å) and wider (~ 0.0456 Å) after drying treatment.

In addition, different interatomic distances in the column structure have been also reported in *Table II-2*. Skoblinskaya and Krasilnikov [50] have summarized a similar table for the unit cell of ettringite from the detailed work by Moore and Taylor [43]. However, their synthesis of data would be probably more reasonable with the consideration that the interatomic distances may change more or less during the removal of combined water in the column. Goetz-Neunhoeffer and Neubauer [47] also described a revised ettringite structural model with the considering of 128 positions for H at room temperature. In their proposition, there existed a shift for every atom (Al atoms as a reference at the original point), which had also a certain difference from the values reported in [43,46]; meanwhile, the lengths of chemical bonds were increased or decreased accordingly.

Table II-2 Information about some important interatomic bonds (related to Figure II-3)

Type of bond	[43]		[47]		Comments
	Distance (Å)	Bond angles (°)	Distance (Å)	Bond angles (°)	
O-Al-O	1.82–2.00	84.7–95.6	1.82 –1.88	79.3–96.2	/
O-Ca-O	2.60–2.75	64.7–93.0 (angles above 115° not given)	2.25–2.83	/	Ca(1)–O(10,12) Ca(2)–O(9, 11)
	2.36–2.56		2.35–2.63		Ca(1)–O(6,8) Ca(2)–O(5, 7)
	2.35–2.52		2.36–2.48		Ca(1)–O(1, 3) Ca(2)–O(2, 4)
S-O	1.31–1.56	105.6–113.2	1.44–1.51	105.8–112.9	/

Hartman and Berliner [46] exhaustively studied the hydrogen bond network in ettringite using the ettringite structural refinement model investigated by high-solution time-of-flight neutron powder diffraction techniques. The length of relevant bonds and corresponding angles were summarized in Table II-3. In the unit cell configuration of ettringite (*Figure II-4*), hydrogen bonds ranging from 1.708 to 2.347 Å denoted a longer distance than normal O-H chemical bond (typically 0.962 Å). From the illustration, it was clearly seen that the hydrogen bond network acted very importantly to stabilize the crystal structure of ettringite and meanwhile played a connective role between neighbor column structures. Renaudin et al. [23] reported the environment of sulfate ions and water groups by Raman spectroscopy. In their model, each sulfate ion was adhered in the inter-column space by twelve hydrogen bonds to twelve water molecules bonded to calcium atoms and four hydrogen bonds to four water molecules coordinated to Ca for each channel water molecule.

Table II-3 Hydrogen bonds information in deuterated ettringite [46]

Group	Type of bond	Distance (Å)	Bond angles (°)
Hydroxyls	O-D–O	2.130–2.347	151.0–173.0
Water molecules		1.708–2.223	110.6–173.1

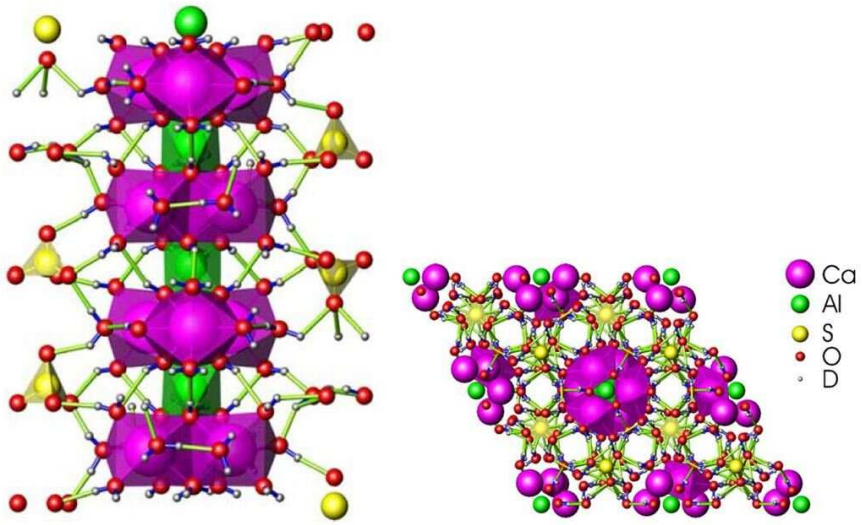

Figure II-4: Hydrogen bonds network along c-axis (left) and perpendicular to c-axis (right) in ettringite crystal. Hydrogen bonds (light green) exist between column structure (water molecules and hydroxyls) and channel components (sulfate ions and water groups) providing the inter-column cohesion. The blue dashes represent O-D chemical bonds [46].

In brief, most investigations agree that the **a**-parameter and **c**-parameter of ettringite locate respectively at 11.165 ~ 11,253 Å and 21.310 ~ 21,679 Å with a specific gravity of 1.750 ~ 1.781. The crystal structure of ettringite is stabilized not only by the chemical bonds like Al-O and Ca-O in the column but also by the network of hydrogen bonds for inter-column distance and adhesion of channel compositions.

2.3.2 Structure of meta-ettringite

Seen that water molecules linked to cations by chemical covalent bonds, the dehydration process to remove these molecules will create vacancies of electrons, which trends to arrange the remaining chemical bonds and produce a new structure formation.

During the water removal process of ettringite, the horizontal thermal expansion was reported twice as the one parallel to the **c**-axis in the range 70–110 °C [51]. With the removal of 34.4% weight after dehydration at 110 °C, the mean refractive index rose from 1.46 (negative) to 1.50 (positive) for Met8[1]. After the arrangement of structure, the dehydrated single crystal was described as an oriented pseudo-morph with approximate cell sides **a** = 8.4 Å, **c** = 10.21 Å accompanying a lattice shrinkage mainly in the plane perpendicular to **c**-axis. The rest compound got a space-group of ***C***6/mmc [40]. Skoblinskaya et al. [52] verified the trends of the growth of the average refractive index during the dehydration process. A meta-ettringite of 18-hydrate with a decrease of inter-column distance (9.73 Å) could still keep a negative

[1] Calculated basing on an initial formula of $3CaO{\cdot}Al_2O_3{\cdot}3CaSO_4{\cdot}32H_2O$.

elongation, which means that the crystal structure of ettringite has been retained. Moreover, the interplanar distance of a further dehydrated meta-ettringite of 12-hydrate arrived 5.2 ~ 5.7 Å (referring to a wide diffuse in X-ray o'grams). Inconsistently, Shimada and Young [25] reported a slight decrease of **c**-parameter (from 21.46 to 21.04 Å after a loss of 15 water molecules) unlike the reported halved value [40] and contrary trend for **a**-parameter, which increased from 11.22 to 11.52 Å. Similar results were also demonstrated for amorphous Met12 by inferring directly occupancies from diffraction data [53]. Differently, another investigation [33] showed that the **c**-parameter down to half after being dehydrated to an 11~13-hydrate (calculated volume = 663.3 $Å^3$ given by [7]) while **a**-parameter markedly decreased from 11.23 to 8.49 Å by Selected Area Electron Diffraction (SAED) patterns, very close to the values reported in [40]. Apart from the thermal process, ettringite has also been reported owing to a reversible transformation to an amorphous phase under 3 GPa with the reduction of both **a**- and **c**-parameter [44].

What's more, the specific surface area (SSA) by Brunauer-Emmett-Teller (BET) theory increased at least 7.8% after the dehydration of ettringite to a 13-hydrate [33], which was indicated to keep long-range order under an in-situ observation [53]. Mantellato et al. [26] demonstrated that AFt phase was possible to lose 12 water molecules at moderate temperature and 0% RH, which did not modify its SSA. The coordination number of Ca and Al was reported respectively to reduce from 6 to 4 after the total dehydration (Met0) [25,50,52]. Baquerizo et al. [7] proposed a negative correlation (*Equation II-12*) between density and water content for ettringite and meta-ettringite:

$$Density = 2600 - 29.25X$$

Equation II-12

Where X presents the water molecule number in the unit structure.

The above section suggests, more or less, the change of the lattice parameter of ettringite after dehydration. The reported variations of lattice parameters were indeed not identical. Whereas, the reduction tendency of **c**-parameter seems to be the same point in different investigations, while for **a**-parameter is still not clear (increase or decrease). Overall, the removal of chemically combined water molecules in column structures could essentially make the crystallinity reduced until to be amorphous companying an increase of density.

2.4 Thermal properties of ettringite and meta-ettringite

The phenomenon of mutual transformation accompanied by water mass change for the binomial, ettringite and meta-ettringite, have been already successfully confirmed for the storage of thermal energy by previous works [6,7,54]. Thanks to its high content of water, the ideal energy storage density could be higher than 500 kWh/m^3 (for Ett32 ↔ Met9 [7]). However, the released heat strongly depends on the quantity and status of absorbed water. Theoretically, water vapor gives a higher value than liquid water with a difference of 40.65 kJ/mol H_2O at 25 °C (the enthalpy of condensation of water vapor).

The decomposition of ettringite here mainly relates to the reaction with water to reform a new crystal, which can reform ettringite under certain conditions. Dehydration, often referring to thermal dehydration, is also named as the process of storing energy, which means only the partial or total removal of water molecules in ettringite crystal. The thermal characterization of the dehydration process mainly describes the thermodynamic analysis, using Thermogravimetric Analysis (TGA) and Differential Scanning Calorimetry (DSC) with different heating rates and temperatures, often accompanied XRD analysis, Fourier-transform infrared spectroscopy (FTIR) or Raman spectroscopy analysis. As a thermodynamic and kinetic process, the dehydration of ettringite is not only temperature-dependent also humidity- and time-dependent.

2.4.1 Decomposition of ettringite

Ettringite has been reported to exist in its aqueous solution up to 90 °C [55] giving the little solubility of ettringite in water [9,56]. Similarly, under saturated steam (100 % RH), ettringite was more resistant than under dry condition: no obvious change at 93 °C. However, at 149 °C, ettringite decomposed to monosulfate [57], which was calculated to be more stable than trisulfate hydrate (ettringite) during its formation above 70 °C [58]. A hydrogarnet phase ($3CaO{\cdot}Al_2O_3{\cdot}6H_2O$, C_3AH_6) was further detected at 232 °C in the autoclave. This process of hydrothermal decomposition has been detailed by three endothermic steps, as the following *Equation II-13* to *Equation II-15* [35]:

$$C_6A\bar{S}_3H_{32}(s) \rightarrow C_4A\bar{S}H_{12}\,(monosulfate) + 2\,C\bar{S}H_{0.5} + 19H(l) \quad 111 < T < 190\,°C$$

Equation II-13

$$C_4A\bar{S}H_{12}\ (s) \rightarrow C_3AH_6(s) + C\bar{S} + 6H(l) \quad 190 < T < 280\ °C$$

Equation II-14

$$3\ C_3AH_6\ (s) \rightarrow C_4A_3H_3(s) + 5\ CH(s) + 10H(l) \quad 280\ °C < T$$

Equation II-15

Some other investigations [31,51] also supported that ettringite decomposed to monosulfate in the range 114–150 °C with high pressures while in contact with aqueous phase. Somehow, the thermal stability of ettringite was enhanced in a solution. From another side, ettringite was confirmed to be definitely stable by a heat treatment at 80 °C in distilled water for 12 hours [28] and even at 107 °C with a pressure of 150 kPa [59]. By the calculation of the stable zone for ettringite in the CaO-Al_2O_3-SO_3-H_2O system at 25, 50, and 85 °C respectively, Damidot and Glasser [60,61] indicated that ettringite was chemically less stable at a higher temperature. Kaufmann and his co-workers [62] indicated that ettringite in a CSA cement block was calculated stable up to 90 °C under steam treatment and it decomposed experimentally to monosulfate under steam curing condition at temperatures far below 100 °C for a CSA cement system. The monosulfate phase was considered unstable and decomposed to katoite ($Ca_3Al_2(SiO_4)_{3-x}(OH)_{4x}$ x = 1.5–3) if at a higher temperature (> 100 °C).

2.4.2 Dehydration of ettringite

Without contact with an aqueous phase, ettringite was supposed to dehydrate itself into meta-ettringite when heated. This process of Ett30 to Met12 manifested that the Arrhenius law only gave a good approximation at 55–70 °C with the growth of meta-ettringite from the surface to internal that controlled by a rate-limiting step at the interface between ettringite and meta-ettringite [63]. However, the reported dehydration temperature and process from different researches were not identical. Ings and Brown [4] found three endothermic peaks for this process by using DSC; only the third peak at about 100 °C showed a large quantity of heat (426.8 J/g) compared with 33.5 J/g at 33 °C and 405.8 J/g at 90 °C. Moreover, the endothermic process started at the very beginning (about 30 °C) according to the DSC curve. This “advanced” dehydration at low temperature was also demonstrated in other studies [5,6,9].

As for in Thermogravimetry (TG), the removal of 30.7 water molecules were detected for a synthetic ettringite: 21–22 water molecules lost up to 70 °C and another 9–10 H_2O were lost between 70 and 1000 °C [8]. Perkins and Palmer [9] assigned that the dehydration in TGA were separated to three steps: first loss of about 23 water molecules (33 % of mass loss) be-

tween 40 and 180 °C, then 3 molecules in the range 200–280 °C and others 3 between 280 and 500 °C. A similar process was also reported by Jiménez and Prieto [29] for natural and synthetic ettringite accompanied by some difference in the mass loss of water may due to their different initial water content and the perfection degree of crystals. Natural ettringite was still indicative in XRD after a heat treatment at 260 °C for 7h by TG [20], which also declared the different behaviors between synthetic and natural ettringite. Furthermore, Abo-El-Enein et al. [64] concluded that the morphology of ettringite affected the dehydration process, which may explain why the weight loss obtained from the thermal analysis was often smaller than the loss calculated based on chemical composition. Besides the main dehydration peak at 110 °C, Ogawa and Roy [31,65] divided the location of peaks at less than 350 °C by DSC with a low heating rate (1 °C/min): one at 160 °C and the other at 250 °C. As no obvious change of X-ray patterns for the samples heated at temperatures both above, these peaks corresponded exactly to the further removal of water after 110 °C.

Moreover, a large sample of ettringite (at the level of grams) seemed much more resistant in an oven than a small one (in order of milligram) in the TGA or DSC. Ettringite was indicated stable below 66 °C and decomposed partially at 93 °C in a drying oven [57]. According to Struble and Brown [6], several grams of ettringite that dehydrated in an oven at 56 °C only lost 14 % of mass after 72 h while 27% loss for a sample of 1 mg at 51 °C during 40 minutes by TGA. This resistance was overcome by a doubled temperature for 2 h in the oven. Else, a couple of days and 0% RH were necessary to remove about 21 water molecules per phase at 40 °C or much longer at 25 °C [5]. Abo-el-Enein et al. [64] determined the mass loss of ettringite at different temperatures under 100 °C, and especially an approximate removal of 20 water molecules per phase at 58 °C [66]. Shimada and Young [25] demonstrated the effect of temperature on the same ettringite samples (at the level of grams): a 3-water-molecules loss at 60 °C, then the progressive loss of 20–21 H_2O at 70–80 °C and 24–25 at 100–120 °C. Zhou and Glasser [54] showed that the temperature of dehydration was directly related to environment humidity. Baquerizo et al. [7] also indicated that a higher temperature was required in a high humidity system than in a dry environment. According to [16], ettringite in CSA paste could lose totally its crystallinity at 60 °C and low RH (3–8 %) for 3 days, which verified the disappearance of ettringite peaks in XRD for some CSA blocks after drying at 90 °C [62].

The natures of matter are always related to structure, so does ettringite. Considering its structure, the removal of water from ettringite may be separated roughly into two parts: zeolitic water in the channels and covalently combined water in the columns.

i. Zeolitic water of ettringite in the channels

For a single-phase, ettringite theoretically contains 32 molecules of water, 30 of which are regularized in the columns networks and only 2 are linked loosely in the channels as "zeolitic water". A few reports stated an ettringite containing 36 molecules of water, from which 6 were zeolitic water molecules [67], but easy to lose and decrease to 30 when dried at 25 °C. This loss of channel water controlled by RH at around 18 °C would not change properties even down to 0.05 P_S (standard pressure) [50]. Renaudin et al. [23] confirmed that no structural modification occurred after losing these zeolitic waters except a slight increase in **a**-parameter and a decrease of **c**-parameter.

ii. Column water of ettringite

The remained water ($n \leq 30$) is known as structural components for the network of ettringite. If n goes below 30, the crystal undergoes structural modification. This process was then detailed by Skoblinskaya et al. [52] by 3 divided steps for the removal of water.

The first loss of 12 H_2O linked to Ca atom ($n= 30 \rightarrow 18$) was said to not change the crystal structure since the residual 18-hydrate kept the same negative elongation and refractive index. Moreover, the typical peaks of ettringite were still very recognizable in X-ray diffraction patterns. However, **a**-parameter decreased approximately from 11.23 Å to 9.73 Å considering that the broadening of diffraction lines could lead to an inaccurate determination.

The next loss of 12 H_2O also from Ca atom ($n = 18 \rightarrow 6$) required harsher experimental conditions. Firstly, very low pressure (20 Pa) was necessary to withdraw 6 H_2O located at the main apex of Ca-polyhedral. This process distorted the ettringite structure, the columns were relatively arranged and the decomposition product was said to be amorphous, of which **a**-parameter was about 8.5 Å [33]. Differently, Bannister et al. [40] indicated that the odd layer-lines of a rotation photograph of ettringite dehydrated at 110 °C along the c-axis were weak, which corresponded to a sideways shrinkage of lattice but very little change along the c-axis. The increase of **a**-parameter and the contrary change of **c**-parameter during the dehydration of ettringite at 70 °C were also described by Shimada and Young [25]. Then, a high temperature (180 °C) made n down to 6. Meanwhile, the second reduction of **a**-parameter was considered to cause the collapse of channels and brought the columns closer. As a result, new chemical bonds might be arranged between SO_4^{2-} and columns. The halved **c**-parameter [40] was prob-

ably caused by the strengthening of remained Ca-O bonds after the re-distribution of electrons of Ca.

The withdrawal of the last 6 water molecules started at 180 °C or higher and 0.8 Pa. Chemical bonds could be surely reorganized because of the absence of OH groups between Al and Ca atoms. However, these new bonds were said to exist neither in all ettringite crystals nor in the whole volume of crystalline. If the dehydration went rapidly (about 120s), fewer bonds were constructed while ruptures inside the crystals and voids formed with increasing expansion of crystals [52]. Briefly, the process of dehydration of ettringite can be summarized in Table II-4.

However, this gradual dehydration process related to the structure of ettringite has not been confirmed by dynamic characterization methods, such as Differential Thermal Analysis (DTA) [54], TG and DSC [4–7,29]. Being in contrast to stepwise dehydration, the work of [53] demonstrated that the removal of water molecules linked to different atoms occurred simultaneously at 50 °C. Briefly, the existence of stepwise dehydration process still needs to be verified by experimental methods.

Table II-4: Structure and water number per unit cell of ettringite during withdrawal process [25,43,50,52]

Step number	Position and form of bond of water molecules		Interatomic distance (Å)		The number of water molecules of a given form of bond	The number of remaining water	Coordination number of Ca (Al)	Condition to withdraw corresponding water molecules
1	Water in channels	/	Ca-O	5.06 and 7.47	1.7	30	8 (6)	Temperature: 18 °C Pressure: ~ 0.05 P_s
2	Water in columns	In the additional vertices of the trigonal prisms	Ca-O	2.60–2.75	12	18	8 (6)	First 6 molecules: Temperature: 18 °C Pressure: ~2 0 Pa
3		In the main vertices of trigonal prisms	Ca-O	2.36–2.56	12	6	5 (6)	Temperature: 18–180 °C Pressure: ~ 20 Pa > P > ~ 0.8 Pa
4		In a hydroxyl form in the Al and Ca polyhedral of columns	Al-O	1.82–2.00	6	0	4 (4)	Temperature: > 180 °C Pressure: ~ 0.8 Pa

2.4.3 Hydration of meta-ettringite

Hydration of meta-ettringite, the reversible process of dehydration, refers to the regain of moved water molecules and reforms hydrates of a higher degree than that of the dehydrated material, and often reproduces ettringite crystals from amorphous phases. This process is usually characterized by Sorption Calorimetry, Dynamic Vapour Sorption (DVS), DSC, TGA and XRD. Same as dehydration of ettringite, the hydration of meta-ettringite is also temperature-, humidity- and time-dependent. Moreover, the hydration process has been indicated releasing the majority of heat within 10 seconds while in contact with liquid water [4].

Bannister et al. [40] reported that the dehydration process was reversible if the residual material (after treatment at 110 °C) was left in moist air for a sufficiently long period. This phenomenon has even been confirmed for the product after TG analysis up to 1000 °C [5], which is supposed to be similar with the hydration of cement material. Giving by [51], the dehydration process of ettringite was reversible at a low temperature for ettringite. Kira et al. [68] also concluded that the short-range order structure of ettringite heated up to 500 °C could recrystallize by the hydration above 60% RH at 20 °C. Zhou and Glasser [54] completed the hydration at different determined temperature (< 120 °C) with an error of ± 2.5–5 °C. Moreover, low temperature and high humidity environment seemed to favor the crystallization of ettringite and reduce the time of formation. The maximum water molecule number of hydrated ettringite in per phase (n_{max}), which negatively correlated to the dehydration degree, could increase up to 36.5 [50] containing about 6 “zeolitic” water molecules [67]. In fact, the excessive water molecules might be adsorbed in crystal defects or just on the crystal surfaces, for which the quantification and localization were difficult. This dehydration/ hydration cycle was repeatable for massive ettringite samples (1–2 g), and after several cycles, ettringite was still able to be reformed in moist nitrogen gas from dehydrated products at 40 °C and 0 % RH [5]. Some gypsum was detectable by X-ray patterns during the hydration experiments [54]. All these hydration processes probably started with some condensation in the defects or on the surface. Hence, a local through-solution nucleation mechanism led to the reformation of ettringite [54]. Baquerizo et al. [7] executed the hydration of Met9 to determine the relation between hydrate state and enthalpy of mixing by isothermal sorption and sorption calorimetry at 25 °C. Furthermore, the results seemed to suggest a possible gradual hydration process: A peak of exothermic enthalpy (17 kJ/mol H_2O) appeared while n was supposed to be between 12 and 14 showing a probably relative change of structure. Continually, the hydration process

could be considered as stable between n = 14 and 30 since the enthalpy stabilized at about 13.3 kJ/mol H_2O while the sorption of two "zeolitic" water molecules only released 6.0 kJ/mol H_2O

Some investigators [16,62] also reported this reversibility of ettringite in CSA cement paste along with a harmful effect on the mechanic performance of the sample. This damage may be caused by the change of ettringite morphology relating to the variation of **a**- and **c**-parameters and a possible change of crystal structure [33] during the cycle process of dehydration and rehydration.

2.4.4 Dehydration and hydration modelling of ettringite vs. meta-ettringite

As mentioned above, the dehydration and hydration processes are related inseparably to humidity and temperature. In addition, the reversible phenomenon between ettringite and meta-ettringite has been already reported to be repeatable under different humidity conditions [5].

The detailed work by Zhou and Glasser [54] firstly demonstrated the thermal stability of ettringite under a controlled environment (temperature and water vapour pressure), with a delimitation that the decomposition/ reformation of ettringite started only if the sample weight loss/gain exceeded 1% in 24h. Under low fixed vapor pressures, typically at 800 Pa, the water molecule number per formula dropped from 30.2 to 10.2 with temperature up to about 60 °C. Meanwhile, the crystallinity of ettringite reduced digressively according to XRD patterns. The same results were reproduced at a higher water vapor pressure while the temperature of dehydration to arrive at an approximate water content must go higher, such as 95 °C for 4666 Pa and 105 °C for 5.3×10^4 Pa to attain $n_{H2O} = 13$. The discussion of the stability of ettringite under different conditions was illustrated in *Figure II-5*.

At the left part of curves (zone of reformation), ettringite was both persistent and stable, which means that ettringite did not decompose, and the decomposed ettringite, meta-ettringite, would spontaneously recrystallize to ettringite. On the right of the curves (zone of decomposition), the phenomenon was exactly contrary. The formula of meta-ettringite was said to be Met10–13 while Ett30–32 for ettringite. An important outcome of this study was that the reversible reaction occurred with a marked hysteresis (the zone between curves). The reformation of ettringite went under a relatively higher water vapor pressure compared with that of the decomposition process. In the hysteresis zone, when starting from saturated water vapor pressures, crystal ettringite would not undergo decomposition unless the zone of de-

composition is reached. Whereas once decomposed, amorphous meta-ettringite would not reform to ettringite unless the zone of reformation was reached. Tambach et al. [69] proposed a fundamentally thermodynamic reason for hysteresis phenomenon using molecular simulations: the hysteresis zone was somehow a free-energy barrier, which interrupted a continuous transition between two binomial hydrates. Thus, an increase or decrease in terms of humidity or temperature (or both) were necessary to overcome this barrier, which seems to be suitable for the transformation between ettringite and meta-ettringite [7].

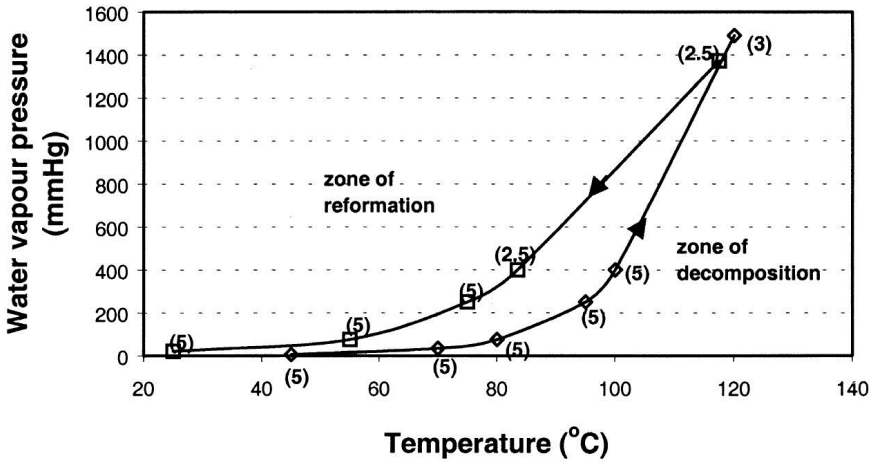

Figure II-5: Curves of the decomposition (right, equation of best fit ln P = –1.61 + 0.075T) and reformation (left, equation of best fit ln P = 1.89 + 0.047T) of ettringite as function of various water vapour pressures and temperatures based on experimental results. The numbers in the parentheses described the uncertainties of temperatures [54].

Baquerizo et al. [7] also modelled the practical stability of ettringite under different conditions (*Figure II-6*) based on experimental results and theoretical extension by Van't Hoff equation. The general location of different zones and the curves agreed with the former model [54] but differed below 60 °C, especially for reformation. Moreover, the theoretical thermodynamic curve of stability for ettringite and meta-ettringite has been plotted without hysteresis.

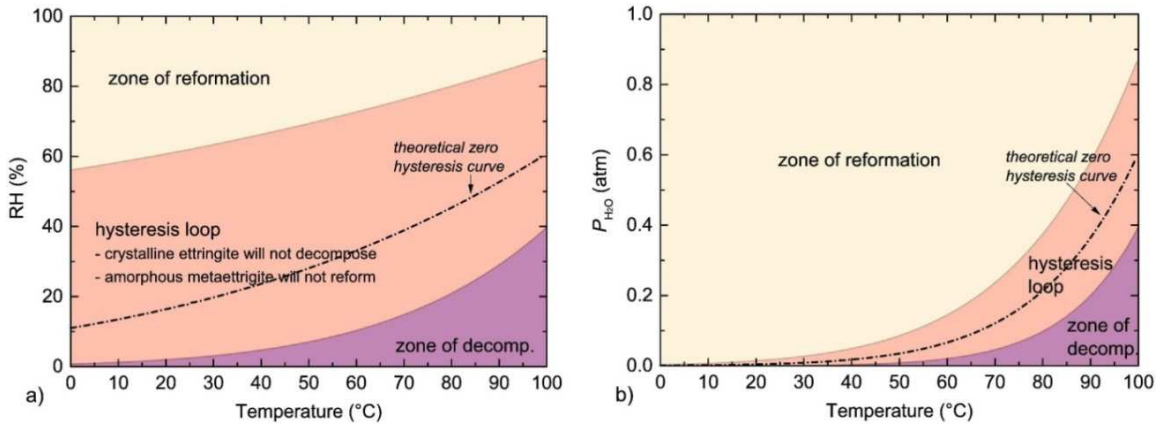

Figure II-6: Curves of reformation (equation of best fit: RH = 56.608 + 0.186T + 0.001T^2) and decomposition (equation of best fit: RH = 0.327 + 0.108T - 0.002T^2 + 4.8E-5T^3) as function of: temperature and left) RH or right) P_{H2O} showing the separated zones. Dashed line represents the theoretical stability limit of ettringite [7].

Thus, we can estimate that at 25 °C, ettringite would reform from meta-ettringite when RH > 62 %, whereas at 70 °C ettringite is said unstable at < 15% RH. The formula of ettringite considered as Ett30–32 on the curve of reformation while Met13 for meta-ettringite on the curve of decomposition. As a fact, these results were based on a small quantity of ettringite powder. So the removal process of water can be considered to occur under a constant condition without different local partial conditions in the samples. However, for a massive compact sample, the outcome could be very different [62]. On the other hand, seen from different investigations [7,31,50,52,54], intermediate products between ettringite and Met10–13 were existed, such as Met17.2, Met20.5, Met25.9, which were indistinguishable in the present modelling diagrams. As the reason of the marked hysteresis, these partially dehydrated products are predicted to locate in a narrow zone around the curve of the "decomposition" for dehydration process. Similarly, a narrow zone exists around the reformation curve for the hydration process. Therefore, it is probably difficult to definitely separate the different zones for each intermediate product, which may also explain why they were not stepwise detectable in TGA or DSC with a typically high speed of scan temperature (10 °C/min) [7,20,29,70].

2.4.5 Reaction enthalpies of dehydration and hydration

Given by the high water content and different chemical environment for water molecules in ettringite, the enthalpies of dehydration and hydration are related to the water content of initial and final hydrates. Meanwhile, the special heat capacity would also change in the function of water content.

Ings and Brown [4] completed heat investigation on the reversible hydration reaction of ettringite, of which a "latent heat" of only 21 J/g was exhibited at 64 °C with sealed sample pans in DSC. However, with the temperature of dehydration rising up, the exothermic heat increased obviously, such as 405.8 J/g for 100 °C. The thermal capacity of synthetic ettringite indicated by Struble and Brown [5,6] was approximately 1.3 J/(g·K), which showed the little potential for sensible heat storage regarding 4.19 J/(g·K) for water. More importantly, they determined the enthalpy of chemical change of ettringite was about 600 J/g phase (decomposition occurred at temperatures from 30 to 70 °C), which preliminarily showed the interest for thermal energy storage. However, this value (600 J/g ettringite, equals to 2100 J/g H_2O) was thought unreasonable since it was smaller than the enthalpy of vaporization of water (2257 J/g H_2O) [7]. Otherwise, it means that the removal of water from the crystal structure needs less energy than water evaporation. Jiménez and Prieto [29] demonstrated the different enthalpies

of dehydration for natural and synthetic ettringite using TG and DSC: the natural one needed 2066 J/g for removal of 23 water molecules per phase at 190 °C while the synthetic consumed 1498 J/g to release 19 molecules. In comparison to the investigation of Baquerizo et al. [7] (973.3 J/g for producing Met9.3 at 60 °C and 997.2 J/g for Met8.3 at 65 °C based on synthetic ettringite), these values were obviously higher. This may be due to the more perfect crystal structure or a higher crystallinity. Because the dehydration of crystal is partly controlled by the escaping rate of water, which means that the crystal size and perfectivity affect the penetration resistance for water molecules and more energy is necessary to overcome this obstruction. Since the first report by Struble and Brown [6], some investigations on the energy storage capacity of ettringite have been realized. The principal results are summarized in Table II-5.

Although the dehydration/ hydration processes are not identical, according to the number of water molecules released/ gained, the promising future for the energy storage by ettringite could still be seen clearly. There exists a distinct mismatch of enthalpy during the reversible processes owing to the condensation of water. Note that: if humid air is used to hydrate meta-ettringite, the same amount of heat should be theoretically released. However, the quantity of released heat during the hydration process was reported to have trends to reduce with the number of cycles (dehydration/ rehydration) going up but no change for complete heat release time [4]. As indicated by Fopah-Lele and Tamba [12], the hydration of most of the salt for energy storage underwent an inconsistent reversible process. The stoichiometrically removed water from salt was insufficient to dissolve all solid phase and re-crystallize salt crystal. This is similar to ettringite as a complex sulfate, which could be seen more or less from the investigation [4]. The small enthalpy was very likely owing to the incomplete hydration by self-released water. Hence, two or more XRD-discernible solid phases (ettringite and lower hydrates) should exist at this transition point. Furthermore, unlike salts, the over-hydration (form a saturated solution, not a hydrate) caused by excessive water from humid air is not noticeable for ettringite thanks to its low dissolubility. Contrarily, the high humidity or pressure of water vapor may help to form a higher water content phase [50,52], which could release more heat by forming more “zeolitic” water.

Table II-5: Different dehydration and rehydration reactions for ettringite and corresponding enthalpies

Process	Reaction	ΔH (kJ/mol)	ΔH (kJ/mol H_2O)	Mass of Samples (powder)	Reference
Dehydration	Ett32 (s) → Met12 (s) + 20H_2O (g)	+ 630	+ 31.5	~1 mg	[6]
		+ 1135*	+ 56.7*	/	[7]
	Ett32 (s) → Met13 (s) + 19H_2O (g)	+ 753 (±126)	+ 39.8 (±6.6)	~1 mg	[5]
		+ 1074*	+ 56.5*	/	[7]
	Ett31 (s) → Met9.3 (s) + 21.7H_2O (g)	+ 1204 (60 °C)	+ 55.5	5.53 mg	[7]
	Ett31 (s) → Met8.7 (s) + 22.3H_2O (g)	+ 1233 (65 °C)	+ 55.2	8.93 mg	[7]
	Ett (s) → Met (s) + 19H_2O (g)	+ 1878 (130 °C)	+ 98.8	~20 mg	[29]
Hydration	Met15.5 (s) + 16.5H_2O (l) → Ett32 (s)	– 241	– 14.6	Several grams	[6]
		– 205*	– 12.4*	/	[7]
	Met10.5 (s) + 21.5H_2O (l) → Ett32 (s)	– 385	– 17.9	Several grams	[6]
		– 279*	– 13.0*	/	[7]
	Met11 (s) + 21H_2O (l) → Ett32 (s)	–238.5	– 11.4	38–50 mg	[7]
	Met9 (s) + 23H_2O (l) → Ett32 (s)	– 286	– 12.4	492 mg	[7]
	Met 9 (s) + 23H_2O (g) → Ett32 (s)	– 1316.1	– 57.2	~80 mg	[7]

*: Calculated values basing on a hydration process in calorimetry from [7].

2.5 Chemical stability of ettringite relating to thermal energy storage

2.5.1 Carbonation of ettringite

Calcium carbonate mineral is one of the main products for the carbonation of a cementitious material, which contains three polymorphs: aragonite, vaterite, and calcite. Once a cementitious component carbonated, the process is irreversible since the relevantly lower Gibbs free energy of calcium carbonate than initial non-carbonated phases under ambient conditions. To ensure the reversibility of meta-ettringite approaches the initial point, the alkaline phase needs to be avoided any presence of active components including CO_2. As Robl et al. [71] stated, dry ettringite samples did not carbonate significantly under the CO_2 environment, while contrary for hydrated ettringite. From this fact, the role of water in the carbonation of ettringite is important. But how does water severe in this process?

The dissolution of CO_2 in water releases H^+ ions and produces a slightly acidic solution (see *Equation II-16*).

$$CO_2 + H_2O \leftrightarrow H^+ + HCO_3^- \quad K_a = 2.5 \times 10^{-4}$$

Equation II-16

This solution can nearly attack all alkaline cement components, including ettringite. Generally, CO_2 can enter the hydrated cement matrix in two ways: penetration by gas phase or diffusion by CO_3^{2-} ions from the dissolution of CO_2 and from carbonate solid phases. The difference between a pore solution in the hydrated cement matrix and pure water for the dissolution of CO_2 are [22]:

- ✓ that CO_2 has a bigger solubility in an alkaline pore solution than other gases;
- ✓ that the solubility of CO_2 is influenced by pressure, pH and temperature;
- ✓ that the alkalinity promotes the solubility of CO_2 compared with in neutral water.

Pajares and his coworkers [72] indicated the harmful effect of carbonate ions, respectively from $CaCO_3$ and $MgCO_3$ silica gel saturated solution, on the structure of ettringite at ambient temperature. But the presence of $Ca(OH)_2$ could evidently delay the carbonation of ettringite. The same phenomenon caused by carbonate ions at different temperatures had been also reported [73].

Detailed works by Grounds et al. [74] on the carbonation of ettringite described that the carbonation effect by atmospheric CO_2 was enhanced at increasing temperatures with constant

humidity. According to XRD and TG analysis, the calculated variation of weight for decomposition products suggested the carbonation reaction was *Equation II-17*:

$$3CaO \cdot Al_2O_3 \cdot 3CaSO_4 \cdot 32H_2O + 3\ CO_2$$
$$\leftrightarrow 3\ CaSO_4 \cdot 2H_2O + 3\ CaCO_3 + 2\ Al(OH)_3 + 23H_2O$$

Equation II-17

This process was confirmed by other investigations [75,76]. Considering the quantity of produced components during the carbonation process, the mechanism could be described as two stages [74]: The first step was the one-dimensional diffusion of CO_2, which agreed with the relationship α^2=kt (Equation II-18[2]). In this stage, CO_2 diffused along the channels and broke the charge balance at the column surface. Meanwhile CO_3^{2-} became competitive to SO_4^{2-}. And ettringite crystal probably split, which initiated further reactions at created defects. The corresponding equation for the second step was $1-(1-\alpha)^{1/3}$=kt (Equation II-19). This process indicated a controlled reaction by reducing the area of reaction interface or reducing volume in cylindrical or lath-like structures. During the second stage, carbonate penetrated into and along the column material, which caused the disruption of the main structure with the rapid formation of calcium sulfate, calcium carbonate, and amorphous aluminum hydroxide.

Similarly, Nishikawa et al. [75] agreed that the carbonation process could be described by two phases and proposed a following numerical relationship (*Equation II-20*):

$$[1-(1-\alpha)^{1/3}]^N = kt$$

Equation II-20

Where N was the index of the rate-determining step: if N= 1, different from [74], the equation suggested a dissolution step of CO_2 at the surface; if N=2, a diffusion-controlled step through product-layer was presented. In addition, at the final step of dry-condition (without pre-mixed with water, but the water was produced before by carbonation reaction) and through the whole process of wet-condition (pre-mixed by w/s = 3), the diffusion-controlled step (N = 2) was always predominant. However, their synthetic ettringite samples had been dried in a vacuum of 0.4 Pa for 1 week. Under such conditions, ettringite was supposed to dehydrate to a lower hydrate [52], which still maintained the main structure of ettringite crystal and distinguishable in XRD. This prediction was supported by the disappearance of a large endothermic

[2] α: decomposition proportion of ettringite; t: time; k: constant

peak of ettringite in TG [75]. Detailed works by Chen et al. [76] integrated directly CO_2 partial pressure, water vapor pressure, and temperature together (*Equation II-21* and *Equation II-22*). The increase of CO_2 pressure (from 6660 to 40000 Pa) and of water vapor pressure (27–1227 Pa) could obviously accelerate linearly the carbonation of ettringite. Moreover, the effect of temperature at 10–50 °C was very important for the carbonation kinetic.

$$v = \frac{\mathrm{dx}}{dt} = k_0 e^{39907/RT} P_{H2O} P_{CO2}$$

Equation II-21

When under water vapor saturated state, the equation could be simplified as following:

$$v = \frac{\mathrm{dx}}{dt} = k_0' e^{-E_a/RT} P_{CO2}$$

Equation II-22

Where v is the carbonation speed, x the carbonation rate, t the time of reaction (h), k_0 and k_0' the carbonation reaction rate constants, E_a the apparent activation energy, R the gas constant, T the temperature (K) of reaction and P_{H2O}, P_{CO2} for water vapor and CO_2 partial pressure (Pa) respectively.

The above carbonation kinetics (*Equation II-22*) was accompanied by the following chemical mechanism (*Equation II-23* to *Equation II-25*):

$$H_2O + * \rightarrow H_2O^*$$

Equation II-23

$$H_2O^* + CO_2 \rightarrow {H_2CO_3}^*$$

Equation II-24

$$\frac{1}{3}(CaO \cdot Al_2O_3 \cdot 3CaSO_4 \cdot 32H_2O) + {H_2CO_3}^* \leftrightarrow CaSO_4 \cdot 2H_2O + CaCO_3 + \frac{1}{3} Al_2O_3 \cdot XH_2O + \frac{1}{3}(26 - X)H_2O + H_2O^*$$

Equation II-25

Where * was the active center. In this process, H_2O was not reactive but could attend the carbonation process like a catalyst. Moreover, the CO_2 capture step was the rate-determining step. Therefore, the fraction of reactive H_2CO_3 was much smaller than that of H_2O.

Developed from the above investigations on ettringite powders, carbonation experiments on pellets (2.5 mm thick) pressed to about 80% theoretical density with parallel carbonation study on pure ettringite powder (< 250 μm) were executed by Zhou and Glasser [77]. The observed acceleration of carbonation on powder samples with both increasing relative humidity and temperature was in good agreement with [76]. Inconsistent with powder samples, compacted pellets gave additionally monosulfate phase since the condensation of water in the pores and inter-crystal space. Additionally, the quantity of condensation water depended on pore geometry and pore volume. Another important outcome of this report was the study on the evolution of carbonation products with depth up in the pellets, shown in *Figure II-7*.

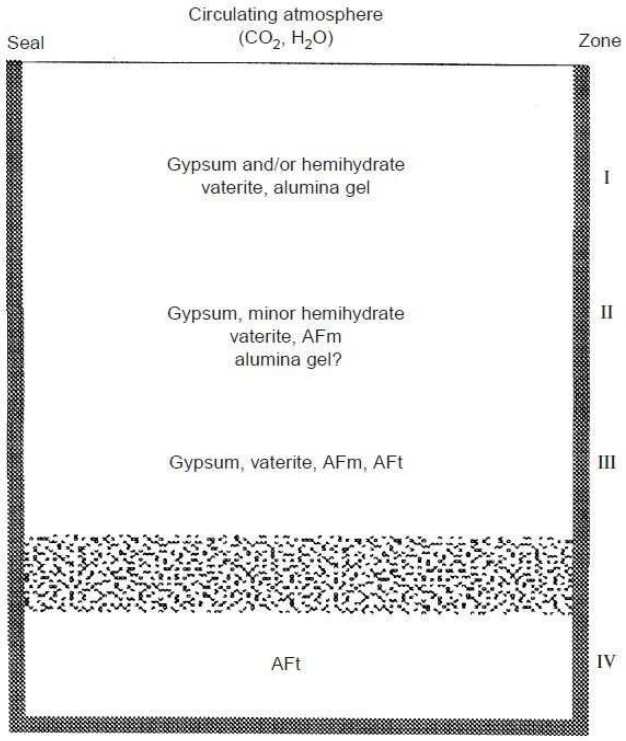

Figure II-7: Schematic of layered zones developed spontaneously in carbonated ettringite pellets at 25–40°C and 68–88% RH. The sides and bottom were sealed to guarantee CO_2 and H_2O penetrate only from the top [77].

As a product of carbonation, the liberated water made the pore space flooded in the reactive layer reducing geometric contact surface of CO_3^{2-}-water interface and disfavored the carbonation process. Considering slower escape of water in pellets than in loose powder, a water-rich zone was supposed to form between zone III and IV (dot zone). This could explain the nucleation and crystallization of monosulfate, which matched well with the thermal decomposition of ettringite at 100% RH or in water. However, the remained AFt phase may already contain carbonate structure said to be recognizable through the slight shift of diffraction peak in XRD patterns as described by Hirabayashi et al. [78]. The same interpretation was also referred via FTIR spectra analyses for synthetic ettringite [9,36]. Damidot and Glasser [79]

proved that CO_3^{2-} ions had great the possibility to substitute into ettringite phases, especially at the boundaries of the stability zone of ettringite (*Figure II-8*, a-b-h-g-f) through the calculation for the stability of ettringite in CaO-Al_2O_3-$CaSO_4$-$CaCO_3$-H_2O system at 25 °C.

Moreover, an ettringite-based material, CSA cement paste powder (63 μm), has been recently examined under 4% CO_2 at 25 °C and 65% RH [16]. After exposure for 10 days, 71 % ettringite was carbonated to hemihydrate, amorphous aluminum hydroxide, and calcium carbonate (aragonite and vaterite) without the formation of monosulfate as reported before. On the other hand, as the binomial of ettringite, the carbonation resistance and corresponding mechanism are still barely discussed in detail for meta-ettringite. However, there is no doubt that ettringite is needed to be protected from CO_2 if used as an energy storage material.

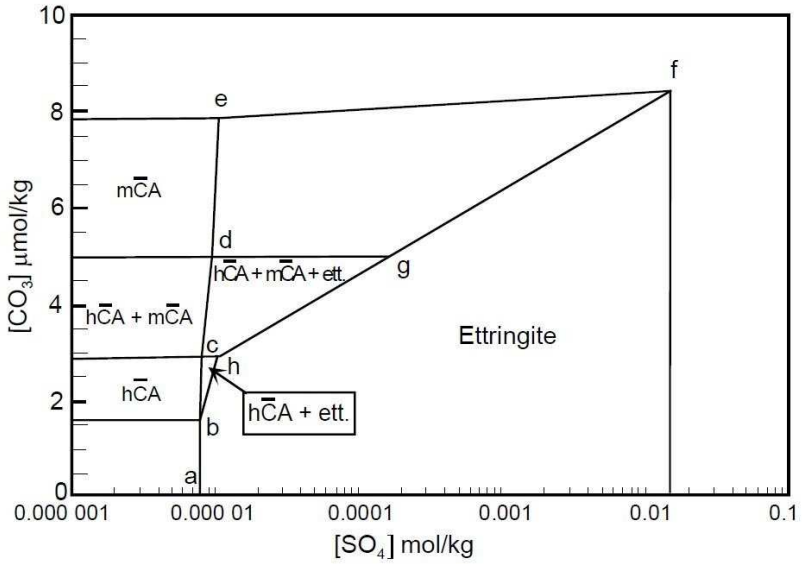

Figure II-8: Stability zones of ettringite as function of various sulfate and carbonate concentration of CaO-Al_2O_3-$CaSO_4$-$CaCO_3$-H_2O system at 25 °C [22].

2.5.2 Ionic substitution phenomenon

Due to the capacity of co-existing with substitutes in the crystal structure, whether partial or total, ettringite was considered as a good host phase [80]. Some substitutions exist in nature while others are synthesizable or presumed to base on electronic charge balance and similar ion radius (*Table II-6*). Exchanges can be made with cations and anions, such as chromate, arsenate [81], or selenate [82] for sulfate; lead, cadmium, cobalt for calcium [83] and iron, chromium for aluminum [6]. Tashiro et al. [84] reported that some heavy metal oxides and hydroxides, like Cr_2O_3, Fe_2O_3, $Cu(OH)_2$, ZnO and $Pb_2O(OH)_2$ promoted the crystal growth of ettringite and produced some changes in microstructure by adding 5 % by weight of above

additives. Morphology of these ettringites was almost identical and no evident difference showed in XRD patterns [22].

Table II-6: Total or partial ionic substitutions in the structure of ettringite basing on detailed work from [4,6,80,81,83,85–100].

Replaced ion	Acceptable ionic size (Å)	Total or partial substitution		
		Natural existing	Obtained by synthesis	Suspected but un-proven
Ca^{2+}	0.90–1.42	/	Cd^{2+}, Sr^{2+}	Co^{2+}, Ni^{2+}, Ba^{2+}, Pb^{2+}, Mg^{2+}, Mn^{2+}, Cu^{2+}, Zn^{2+}
Al^{3+}	0.42–0.76	Si^{4+}, Fe^{3+}, Cr^{3+}, Mn^{3+}	Ti^{3+}	Ni^{3+}, Co^{3+}, Ga^{3+}
SO_4^{2-}	0.62–3.71	$B(OH)_4^-$, CO_3^{2-}, SO_3^{2-}	OH^-, Cl^-, I^-, MoO_4^-, CrO_4^{2-}, SeO_4^{2-}, SeO_3^{2-}, VO_4^{3-}, AsO_4^{3-}, $HCOO^-$	BrO_3^-, ClO_3^-, IO_3^-, NO_3^-
OH^-	0.62–1.38	/	/	O^{2-}

Coordination, size, and electronegativity were likely the principal indicators that result in the observed differences among the oxyanions. These substitution phenomena most probably occurred by the reason of that, those particle surfaces of ettringite exhibited a net negative charge [101]. Therefore, the incorporation of anions in the bulk is much more important than surface adsorption. The extent of the solid solution with ettringite was thought to be inversely proportional to the difference in size and electronegativity of the oxyanion compared with SO_4^{2-} [102]. Thus, the uptake of MoO_4^{2-} was ignorable or even non-existent, which could be attributed to a large size and made it unstable. However, a solid solution is probably determined by more factors than just size and electronegativity. Ettringite showed amity to CrO_4^{2-} and SeO_4^{2-}, of which substituted ettringite reflected a similar solubility compared with a pure one [96]. Kumarathasan et al. [103] also had synthesized X-ray diffraction phase pure products with chromate and selenate, substituted completely sulfate in ettringite, and with a partial substitution for arsenate, borate, and vanadate. Zhang and Reardon [97] established the removal of B, Cr, Mo, and Se oxyanions from high pH waters by incorporation into ettringite. Else, ettringite showed an anion affinity in the order of $B(OH)_4^- > SeO_4^{2-} > CrO_4^{2-} > MoO_4^{2-}$, which corresponded to the work of [102]. Borate was verified as an oxyanion to incorporate easily into ettringite with supporting of the existence of several natural borate-substituted ettringites [98]. However, SO_4^{2-} was still preferable to form ettringite than other ions like

SeO_4^{2-} [82]. Therefore, the formation of ettringite follows this affinity order when diverse oxyanions present in a mixed solution. Equally, CO_3^{2-}-, IO_3^{2-}-, Cl^--ettringite had also been reported [4,6,104]. It seems thus reasonable to hypothesize that, a partially or completely substituted ettringite would contain two or more types of oxyanion in a mixed solution without adequate sulfate ions supply.

The competing effects in ettringite are reported not only for anions but also for cations to replace aluminum and calcium in the column structures. Respecting to electron balance, Al was possible to be replaced by Ti^{3+}, Ga^{3+}, Cr^{3+}, Mn^{4+}, Si^{4+}, Fe^{3+} or Ge^{4+}, and Ca^{2+} by Sr^{2+} or Pb^{2+} [99]. Some nature minerals containing cation substitutes are also well known as members of the ettringite group. Among them, thaumasite ($Ca_6[Si(OH)_6]_2{\cdot}24H_2O\}(SO_4)_2(CO_3)_2$) and jouravkite ($Ca_6[Mn(OH)_6]_2{\cdot}24H_2O\}(SO_4)_2(CO_3)_2$) have close a-axial length compared with ettringite. Synthesis of naturally existing Cr^{3+}-ettringite, which owned similar properties with ettringite has been respectively reported by several investigations [6,27]. A structural model for Sn^{4+} uptake by ettringite was developed based on the crystallographic parameters. Preliminary experiments further supported that ettringite could be a host phase for Sn^{4+} even without respect to equal electric exchange to Al^{3+} [105]. Similarly, Si^{4+}, Ge^{4+}, and Mn^{4+} have been equally mentioned to replace Al^{3+} in [99].

In fact, most substituted ettringite probably share analogous physical and chemical properties, which account on their similar structures such as solubility, alkalinity, and large water content. Struble and Brown [6] studied thermal dehydration properties on several substituted ettringite and found that the measured enthalpies were ranged between 418 joules and 962 joules per gram of sample. For example, a Fe-substituted ettringite lost more H_2O molecules and had a bigger thermal decomposition enthalpy (800 J/g) than a normal ettringite (600 ± 100 J/g) under same condition [5]. If considering differently, the enthalpies of removing per mole of water were respectively 37.8 kJ/mol H_2O for ettringite and 46.8 kJ/mol H_2O for Fe-substituted ettringite. Besides, Fe-substituted ettringite could also sustain dehydration and hydration loops but with a diminution of liberated heat (about 56% lower than that of normal ettringite) [4]. Antao et al. [20] reported that the dehydration of sturmanite (ideal empirical formula: $4CaO{\cdot}Fe_2O_3{\cdot}0.5B_2O_3{\cdot}2CaSO_4{\cdot}33H_2O$) at 150 °C gave an enthalpy of 1660 J/g with 41.6 % weight loss (28.7 H_2O) while 641 J/g for ettringite of 40.4 % loss (26.6 H_2O) at 170 °C.

Kumarathasan et. al [103] investigated the heat of dehydration for a series of oxyanion substituted ettringite and the enthalpy value varied with the oxyanion ratio in per phase (*Table II-7*). They considered that the value of the $(SO_4)_{3.3}$ phase was indeed as same as that reported by Struble and Brown [6]. Basing on this indication, most of the oxyanion substituted ettringites got a higher dehydration heat than a normal one and the value depended on the substitution degree of sulphate. Furthermore, the $B(OH)_4^-$ phases demonstrated the largest dehydration heat and approximately doubled the one of a normal ettringite. It was said that this evident increase came from the whole stronger hydrogen bonds in the borates, which could be seen from the FTIR study [103]. In addition, thaumasite could present a higher dehydration enthalpy (1215 J/g) than ettringite (930 J/g) in DSC (50–250 °C) [106].

Table II-7: Dehydration heat for different oxyanion substituted ettringite from [103]

Oxyanion mole ration from chemical analysis [a]	Heat of dehydration [b] (J/g)	Weight loss [c] (wt. %)	Possible corresponding theoretical formula of substituted ettringite
$(SO_4)_{3.3}$	600	45	$Ca_6Al_2(SO_4)_3(OH)_{12}\cdot 26H_2O$
$(SO_4)_{2.6}(AsO_4)_{0.3}$	830	45	$Ca_6Al_2(AsO_4)_2(OH)_{12}\cdot 26H_2O$
$(SO_4)_{3.0}[B(OH)_4]_{1.0}$	1180	45	$Ca_6Al_2(SO_4)_2[B(OH)_4](OH)_{12}\cdot 26H_2O$
$(SO_4)_{2.2}[B(OH)_4]_{1.2}$	1230	47	
$(SO_4)_{1.5}[B(OH)_4]_{1.4}$	1280	51	
$(SO_4)_{2.5}(CrO_4)_{0.6}$	840	47	$Ca_6Al_2(CrO_4)_3(OH)_{12}\cdot 26H_2O$
$(SO_4)_{2.7}(CrO_4)_{1.3}$	580	45	
$(CrO_4)_2$	470	39	
$(SO_4)_{2.8}(SeO_4)_{0.5}$	940	47	$Ca_6Al_2(SeO_4)_3(OH)_{12}\cdot 26H_2O$
$(SO_4)_{1.7}(SeO_4)_{1.2}$	880	46	
$(SeO_4)_{2.5}$	760	43	
$(SO_4)_{2.8}(VO_4)_{0.5}$	520	58	$Ca_6Al_2(VO_4)_2(OH)_{12}\cdot 26H_2O$

a: Normalized to 6 Ca.

b: For the endotherm with a maximum at 100–140 °C by DSC.

c: Loss on ignition at 850 °C for 18 hours.

With this understanding, some physical and chemical natures of ettringite may be modified by total or partial replacement of cations, anions, or both. Especially for thermal properties, a divalent or trivalent metallic substitution can possibly change the chemical environment of combined water groups. Thermal performance is thereby changed by the modification of rele-

vant chemical bonds. Similarly, the modification by oxyanions may also make ettringite more resistant from CO_2 because of having smaller mobility for a substitute anion than CO_3^{2-}.

2.6 Prototypes adapted to ettringite-based materials

Besides thermal characterizations by TGA and DSC, the reactor test is necessary to examine the energy performance of materials aiming at enlarging the scale (from grams to kilograms) of energy storage. Kuznik et al. [107] classified mainly the reactors to fixed bed reactors and fluidized bed with respect to the movement of solid reactants. Both kinds of reactors can ensure good heat and mass transfer. However, it is believed that fluidized bed reactors are most suitable if the kinetics of heat and mass transfers between absorbent and absorbate are limited at the bed scale and not at the particle scale [107]. Indeed, most researches on reactors for ettringite-based materials to store thermal energy are fixed-bed cases [14,15,18,108].

2.6.1 Matsushita Electric Works, Ltd. Case

Early in 1983, Kazuo et al. [108] presented a conception of heat recover method basing on ettringite particles (*Figure II-9*). To store solar energy, the lid (3) with insulating property is opened. Mirror (4) attached to the inner face of the lid (3) reflects solar light to heat up ettringite grains (2) to meta-ettringite. After 5 hours of exposure, the temperature could rise to 70 °C. Moreover, the box (1) containing ettringite grains may be tilted to increase the amount of received sunlight. Once dehydration is done, the lid (3) is closed and water is supplied through the pipe (5) into the box (1) to hydrate meta-ettringite. This water is not only used to react with meta-ettringite but also to carry produced heat. The heated water is then stored in the tank (7) via pipe (6). When needed, hot water in the tank can be taken out by vortex extraction pipe (8) to be multi-used. Besides, (9) is a drain pipe.

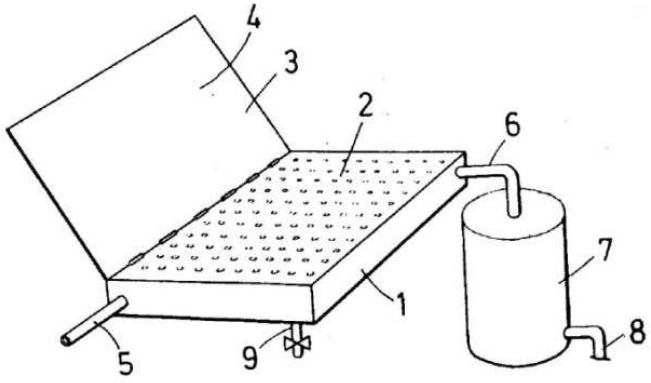

Figure II-9: Schematic diagram of energy recover device [108].

2.6.2 Swiss Federal Laboratories for Materials Science and Technology (Empa) reactor cases

In 2010, Pelletier et al. [109] obtained a maximum content of ettringite in the final hydrated paste via varying the proportion among CSA-clinker, anhydrite and Ordinary Portland cement (OPC). Kaufmann and Winnefeld [14,110] then used this system to develop special CSA concrete cylinders in order to analyze thermal performance by calorimeter for the heat releasing process [110]. The blend used in the concrete is composed of 78 wt. % CSA-clinker and 22 wt. % gypsum. In 2011, a concrete block (50 × 40 × 30 cm^3) integrated copper pipes (*Figure II-10* left) is developed to be a demonstrator. The cooper pipes were designed to channel heat-carrier to dehydrate the concrete (> 80°C) and collect produced heat during rehydration. The small sample blocks are pre-heated before the hydration by water. The first results of rehydration were positive that they could heat up to 80 °C within an hour [110]. In *Figure II-10* b, a prototype composed of 16 slabs (50× 10 × 3 cm^3) is hydrated by humid air (90% RH at 20°C) at 2 m/s. The temperature increases from 23 to 37 °C within 1.5 hours.

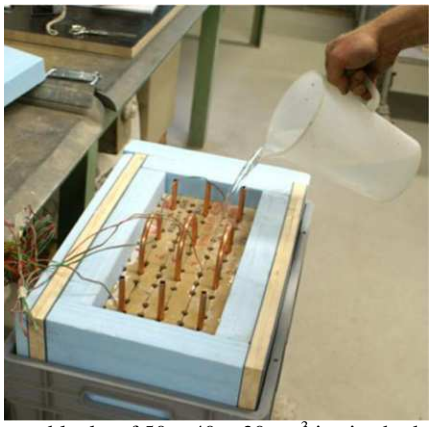

(a) concrete blocks of 50 × 40 × 30 cm^3 in size hydrating by suction of water

(b) concrete blocks of 16 slabs of 50×10×3 cm^3 by sorption of humid air (90 % RH)

Figure II-10: First lab scale prototypes at EMPA [110].

In 2015, a real scale of ettringite based-concrete thermal energy storage system (24 blocks measuring 6 m^3 in size) was installed in a garage of a private house (*Figure II-11*) [110] by Empa's Concrete/Construction Chemistry laboratory. The system is connected to solar energy collectors that produce hot heat-carrier flow (mostly water, > 80 °C) in summer. Then the concrete blocks are dehydrated by the heat carrier via heating coils (copper pipes in *Figure II-12* a). During the dehydration of blocks, the emission of water vapor of ettringite takes place to store heat. In the meantime, water vapor is drawn by the pump and collected in the steam condenser (*Figure II-11*). When heating is needed, water is continually added to the containers. The dehydrated concrete reacts with water to convert ettringite, thereby releasing stored

chemical energy as heat. The excessive water flows into the holes to fill the container below and hydrate the low part of concrete blocks (Figure II-12 b-d). The released heat is occupied with cold heat-carrier flowing in the copper pipes for house heating use. This system of storing energy is environmentally friendly excepting the CO_2 emissions during manufacture and transport. Moreover, the low cost of concrete (< 400 Swiss francs) makes the system very cost-effective. However, several things are still not clarified:

- ✓ Do the cracks due to transformation between ettringite and meta-ettringite will improve the energy performance of concrete blocks or the opposite effect?
- ✓ Does the quantity of releasing heat matches the lab experimental results or not?
- ✓ The number of function cycles (dehydration/hydration cycles).
- ✓ How to optimize the systems?

(a) concrete blocks of 3 columns by 8 levels (b) final embedded set-up

Figure II-11: First 1:1 scale thermal energy storage prototype by ettringite-based material (concrete) in a private house garage in Seelisberg, Switzerland [110].

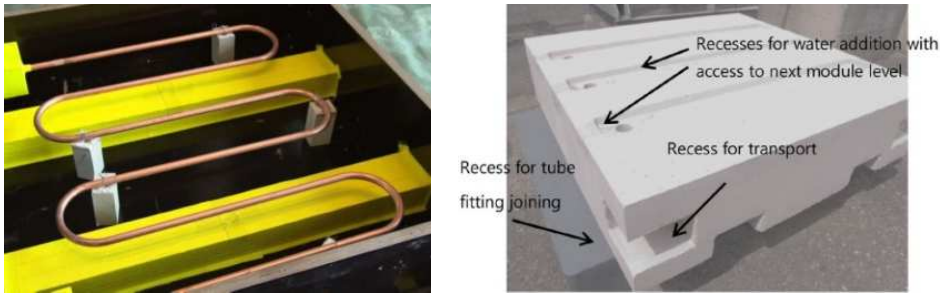

(a) Integrated copper pipe in the block (b) Hardened concrete block

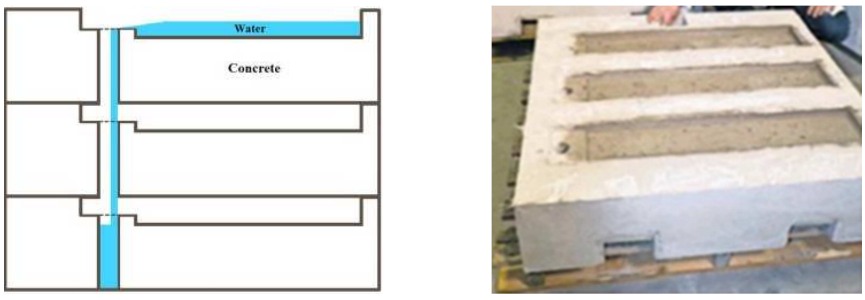

(c) Schematic diagram of hydration (d) Experiment photo of hydration

Figure II-12: Hydration method for concrete blocks [110,111]

2.6.3 Institut National des Sciences Appliquées de Toulouse (INSA Toulouse) cases

Ndiaye et al. [18,112] used 95 % CSA Alipre, 4 % lime, and 1 % aluminum powder to prepare a high ettringite contained aerated cement paste cylinder (68 % ettringite) showing in *Figure II-13*. The porosity of material arrives at 76 % and 8.8×10^{-14} m^2 for air permeability. For characterizing the thermal performance of materials, the investigators studied two kinds of reactors.

The first one is equipped with a metal tube across the center of cylinder sample (*Figure II-14* a). To dehydrate the material, hot heat transfer fluid (heat-carrier) from a thermostat (*Figure II-14* (c)) passes through a metal tube and heats the ettringite material to emit water vapor. A nitrogen gas goes from top to bottom to take away the water vapor. Reversibly, humid nitrogen from a bubbler (*Figure II-14* c) is introduced by the humidification valve to hydrate material and release heat. Cold heat fluid occupies the heat by the metal tube which works as a heat exchanger. By this method, 61 kWh/m^3 was achieved while 44% of heat converted [18].

In order to improve the performance, the heat exchanger, metal tube, is moved away to increase the energy transfer efficiency (see *Figure II-14* b). Here, the heat-carrier also works as a mass carrier. The experimental results showed a better yield from 44 % to 71 % with a performance of 117 kWh/m^3 [18]. Compared to the first kind of reactor, not only the energy performance but also the operability is progressed.

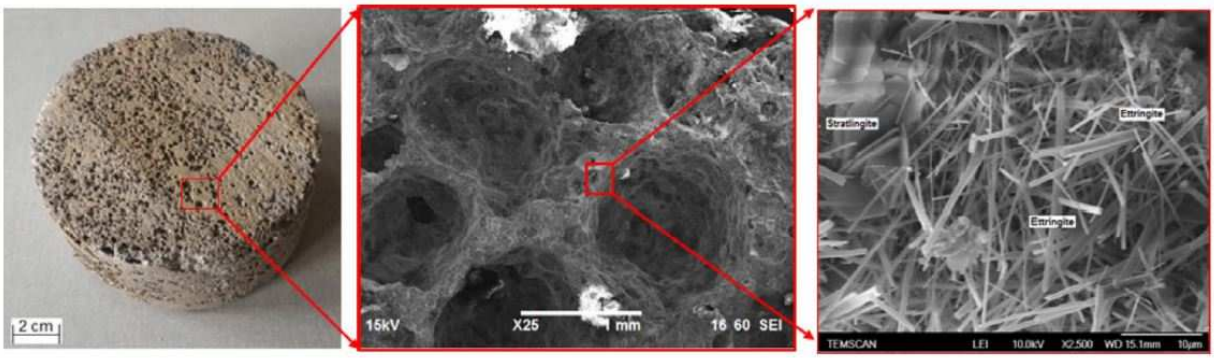

Figure II-13: Aerated high ettringite-based material and its microscopy photo by SEM [18]

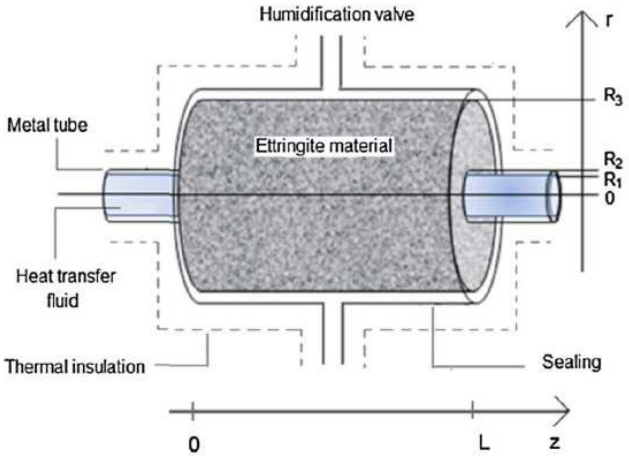

(a) Schematic diagram of prototype I

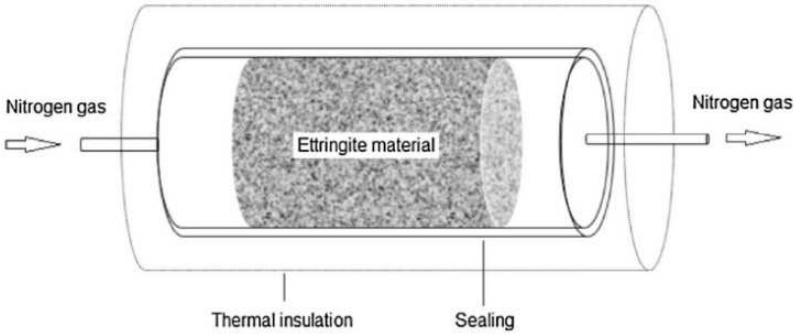

(b) Schematic diagram of prototype II

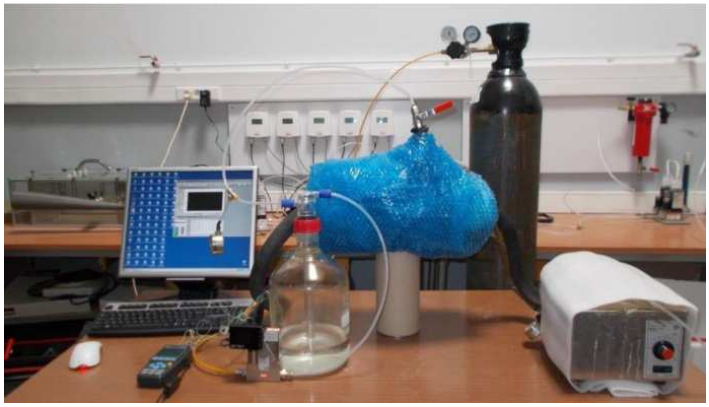

(c) Experimental set-up

Figure II-14: Designs and experimental set-up of INSA Toulouse cases [18].

2.6.4 Sorbent separating reactor case (Univ. of Stuttgart)

Mette et al. [113] investigated a sorbent separating reactor (external reactor, *Figure II-15*). During operation, energy storage material is filled from the top material inlet (Figure II-15 b). Then humid air enters from the side (flow channel) by the homogenous way to hydrate material. Thanks to the small width, the pressure loss is very low. Once the temperature of outlet air decreases, the material is drawn up into the material reservoir (*Figure II-15* a) and the reactor is refilled by new material. The heat exchanger is used to recover the produced heat in the air. The contrary process, dehydration of material, is similar. Somehow, this concept may be concluded as a semi-fixed bed reactor. The limited quantity of material presenting in the reactor reduces the heat loss and economizes the sensible heat during the charging/discharging cycles. Although the authors design this reactor for the zeolite case, the concept design is still very interesting and useful for ettringite materials in granular or powder form.

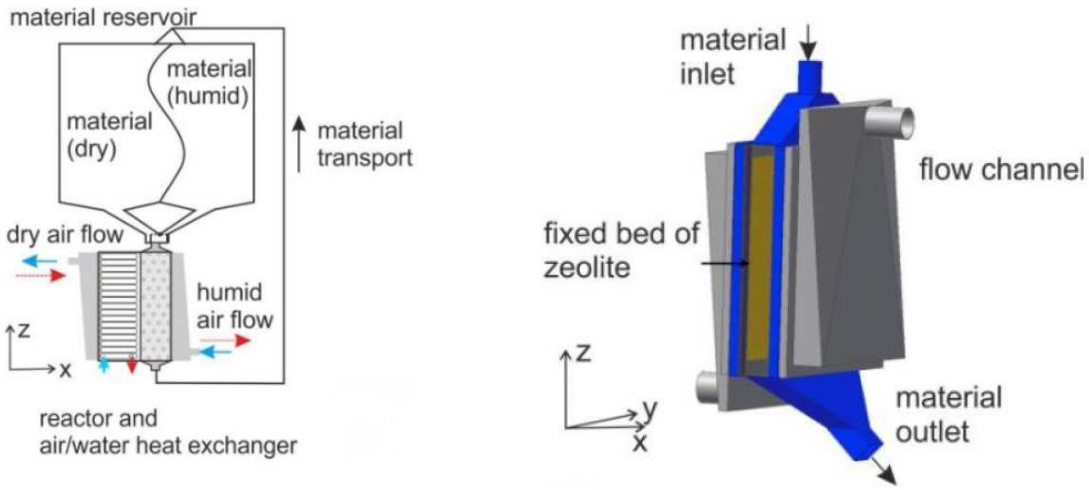

(a) schematic diagram (left) with blue arrow for charging and red arrow for discharging

(b) 3D-view of external reactor design

Figure II-15: A sorbent separating reactor; adapted from [113].

2.7 Conclusion

Despite that the use of ettringite for thermal energy storage has not been scooped deeply out; this chapter synthesizes its relevant thermal properties, preparation methods, chemical durability, etc. In comparison to other materials for energy storage, such as zeolite, $MgSO_4$, NaOH, ettringite promises a theoretically higher rehydration enthalpy thanks to the larger water content. Given that the lack of standards for an acceptable prescribed minimum of phasic releasable energy and necessary thermo-physical properties to determine, the researches on ettringite are still insufficient for applications of storing heat. No identical enthalpies of thermal procedures and few studies on the prototypes of large volume have been reported. Moreover, technical problems, facing heat exchangers, carbon-resistance, and absorption including the instability of adsorbent and variability of systems during rehydration/ dehydration processes, increase uncertainty for big scale applications. In terms of the material and reactor, several unknowns and variabilities about ettringite need to be clarified.

- ✓ **The thermodynamics of dehydration and rehydration of ettringite need to experiment** as the function of partial water vapor pressures and temperatures. Besides, **the kinetics of dehydration and rehydration (including the enthalpies) need to be studied under different conditions** to ensure the energy performance of ettringite.

- ✓ As being difficult for industrial productions of pure ettringite in large quantities, ettringite-based materials are recommended to be used for thermal energy storage. However, the carbonation is the common issue for cement-based materials, especially for ettringite-based used in the storage of heat with the circulation of ambient air. Therefore, **the investigation on the durability (mechanical and chemical) of ettringite-based materials is necessary in order to validate one potential material for energy storage study.**

- ✓ The already-known properties of ettringite are probably not adaptable for ettringite-based materials, which are mostly considered as cement materials. In these materials, ettringite is no longer a single phase and has the possibility to react with other compounds under certain conditions. Most investigations were executed on ettringite powders, which minimize the effect of the dynamic process. Thus, a very different result could be seen if the form of sample changes without mentioning the change of a chemical environment. Therefore, **thermal kinetics of the chosen material under**

various temperatures and partial water vapor pressures are required to be investigated for both dehydration and hydration.

- ✓ As for the reactors, it needs to be designed to adapt not only to material but also its form. For the moment, reported reactors for ettringite materials are only suitable for blocks. To hydrate materials, water vapor is suggested to be used rather than liquid water because of a 3 times larger quantity of released energy. Moreover, ettringite material in granular form is recommended to increase the surface of reaction. Therefore, **a new reactor should be designed in open mode with consideration of the kinetics of hydration/dehydration of material. The experiments should be carried out for charging/discharging tests under operating conditions.**

Briefly, by making a general survey of the significant advance on the thermochemical energy storage concept, the investigation on ettringite for energy storage seems to be insufficient. However, it can affirmatively make a follow-up and even surpass other actually existed materials in the near future because of the large capacity of storage and low cost by gaining from cement materials. This thermochemical storage concept based on ettringite will become a competitive technology with the development of material and system optimization.

2.8 Objectives of the thesis

The purpose of this thesis work is related to the conclusion obtained in section 2.7, which is going to investigate the impact of water activity, temperature, and carbonation effect on the stability and durability of ettringite materials. The main objectives are listed as follows:

- ✓ Experimental study on the ettringite hydrate states as a function of water vapor partial pressures and temperatures for thermodynamics and kinetics.
- ✓ Investigation of the carbonation durability of three ettringite-based materials in order to validate the most potential material for thermal energy storage.
- ✓ The thermal kinetics of the chosen material needs to be studied at operating conditions. Besides, the porotype tests require an adapted open-mode design for the reactor in order to carry out dehydration / hydration experiments under the application operating conditions.

2.9 References

[1] Yang DY, & Guo R. Experimental study on modulus and hardness of ettringite. Exp Tech 2014;38:6–12.

[2] Walker DD et al. Innovations and uses for lime, ASTM; 1992.

[3] Lehmann J. Über den Ettringit, ein neues Mineral in Kalkeinschlüssen der Lava von Ettringen (Laacher Gebiet). Neues Jahrb Für Mineral Geol Und Paläontologie 1874:273–5.

[4] Ings JB, & Brown PW. An evaluation of hydrated calcium aluminate compounds as energy storage media. NASA STI/Recon Tech Rep N 1982;83.

[5] Struble LJ, & Brown PW. Heats of dehydration and specific heats of compounds found in concrete and their potential for thermal energy storage. Sol Energy Mater 1986;14:1–12.

[6] Struble LJ, & Brown PW. Evaluation of ettringite and related compounds for use in solar energy storage. Prog Rep Natl Bur Stand Washington, DC Cent Build Technol 1984.

[7] Baquerizo LG et al. Impact of water activity on the stability of ettringite. Cem Concr Res 2016;79:31–44.

[8] Grounds T et al. The use of thermal methods to estimate the state of hydration of calciumtrisulphoaluminate hydrate $3CaO{\cdot}Al2O_3{\cdot}3CaSO_4{\cdot}nH_2O$. Thermochim Acta 1985;85:215–8.

[9] Perkins RB, & Palmer CD. Solubility of ettringite ($Ca_6[Al(OH)_6]_2(SO_4)_3{\cdot}26H_2O$) at 5–75 °C. Geochim Cosmochim Acta 1999;63:1969–80.

[10] Hongois S et al. Development and characterisation of a new $MgSO_4$−zeolite composite for long-term thermal energy storage. Sol Energy Mater Sol Cells 2011;95:1831–7.

[11] N'Tsoukpoe KE et al. A systematic multi-step screening of numerous salt hydrates for low temperature thermochemical energy storage. Appl Energy 2014;124:1–16.

[12] Fopah-Lele A, & Tamba JG. A review on the use of SrBr2·6H2O as a potential material for low temperature energy storage systems and building applications. Sol

Energy Mater Sol Cells 2017;164:175–87.

[13] Sahoo DK et al. Determination of thermodynamic stability of lanthanum chloride hydrates (LaCl3.xH2O) by dynamic transpiration method. J Alloys Compd 2014;588:578–84.

[14] Kaufmann J, & Winnefeld F. Cement-based chemical energy stores, 2011.

[15] Cyr M et al. Energy storage/withdrawal system for a facility, 2015.

[16] Ndiaye K et al. Durability and stability of an ettringite-based material for thermal energy storage at low temperature. Cem Concr Res 2017;99:106–15.

[17] Ndiaye K et al. Modelling and experimental study of low temperature energy storage reactor using cementitious material. Appl Therm Eng 2017;110:601–15.

[18] Ndiaye K et al. Experimental evaluation of two low temperature energy storage prototypes based on innovative cementitious material. Appl Energy 2018;217:47–55.

[19] Ndiaye K et al. Thermal energy storage based on cementitious materials: A review. AIMS Energy 2018;6:97–120.

[20] Antao SM et al. DTA, TG, and XRD studies of sturmanite and ettringite. Can Mineral 2002;40:1403–9.

[21] Brykov AS et al. Hydration of portland cement in the presence of aluminum-containing setting accelerators. Russ J Appl Chem 2013;86:793–801.

[22] Glasser FP. The stability of ettringite. Int. RILEM Work. Intern. Sulfate Attack Delayed Ettringite Form., RILEM Publications SARL; 2002, p. 43–64.

[23] Renaudin G et al. A comparative structural study of wet and dried ettringite. Cem Concr Res 2010;40:370–5.

[24] Terai T et al. Synthesis of ettringite from portlandite suspensions at various Ca/Al ratios. Inorg Mater 2007;43:786–92.

[25] Shimada Y, & Young JF. Structural changes during thermal dehydration of ettringite. Adv Cem Res 2001;13:77–81.

[26] Mantellato S et al. Impact of sample preparation on the specific surface area of

synthetic ettringite. Cem Concr Res 2016;86:20–8.

[27] Perkins RB, & Palmer CD. Solubility of $Ca_6[Al(OH)_6]_2(CrO_4)_3 \cdot 26H_2O$, the chromate analog of ettringite; 5–75 °C. Appl Geochemistry 2000;15:1203–18.

[28] Shimada Y, & Young JF. Thermal stability of ettringite in alkaline solutions at 80 °C. Cem Concr Res 2004;34:2261–8.

[29] Jiménez A, & Prieto M. Thermal stability of ettringite exposed to atmosphere: Implications for the uptake of harmful ions by cement. Environ Sci Technol 2015;49:7957–64.

[30] Taylor HF. Cement chemistry. Thomas Telford; 1997.

[31] Ogawa K, & Roy DM. C4A3S hydration ettringite formation, and its expansion mechanism: I. expansion; Ettringite stability. Cem Concr Res 1981;11:741–50.

[32] Grusczscinski E et al. The formation of ettringite at elevated temperature. Cem Concr Res 1993;23:981–7.

[33] Zhou Q et al. Metaettringite, a decomposition product of ettringite. Cem Concr Res 2004;34:703–10.

[34] Mehta PK, & Klein A. Formation of ettringite by hydration of a system containing an anhydrous calcium sulfoaluminate. J Am Ceram Soc 1965;48:435–6.

[35] Šatava V, & Vepřek O. Thermal decomposition of ettringite under hydrothermal conditions. J Am Ceram Soc 1975;58:357–9.

[36] Pan GY et al. Research of dehydrated calcium sulphoaluminate hydrates (AFm) and its hydration. J Wuhan Univ Technol 1997;19:28–30.

[37] Peng J, & Lou Z. Study on the mechanism of ettringite formation. Journal-Chinese Ceram Soc 2000;28:511–5.

[38] Wencil Brown P, & LaCroix P. The kinetics of ettringite formation. Cem Concr Res 1989;19:879–84.

[39] Havlica J, & Sahu S. Mechanism of ettringite and monosulphate formation. Cem Concr Res 1992;22:671–7.

[40] Bannister F et al. Ettringite from Scawt Hill, Co. Antrim. Mineral Mag 1936;24:324–9.

[41] Murdoch J, & Chalmers RA. Ettringite ("Woodfordite") from Crestmore, California. Am Mineral 1960;45:1275–8.

[42] Moore AE, & Taylor HFW. Crystal structure of ettringite. Nature 1968;218:1048.

[43] Moore AE, & Taylor HFW. Crystal structure of ettringite. Acta Crystallogr Sect B 1970;26:386–93.

[44] Clark SM et al. Effect of pressure on the crystal structure of ettringite. Cem Concr Res 2008;38:19–26.

[45] Berliner R et al. Quasielastic neutron scattering study of the effect of water-to-cement ratio on the hydration kinetics of tricalcium silicate. Cem Concr Res 1998;28:231–43.

[46] Hartman MR, & Berliner R. Investigation of the structure of ettringite by time-of-flight neutron powder diffraction techniques. Cem Concr Res 2006;36:364–70.

[47] Goetz-Neunhoeffer F, & Neubauer J. Refined ettringite ($Ca_6Al_2(SO_4)_3(OH)_{12}\cdot 26H_2O$) structure for quantitative X-ray diffraction analysis. Powder Diffr 2006;21:4–11.

[48] McConnell D, & Murdoch J. Crystal chemistry of ettringite. Mineral Mag 1962;33:59–64.

[49] Bezjak A, & Jelenic I. Crystal structure investigation of calcium aluminium sulphate hydrate-ettringite. Croat Chem ACTA 1966;38:239.

[50] Skoblinskaya NN, & Krasilnikov KG. Changes in crystal structure of ettringite on dehydration. 1. Cem Concr Res 1975;5:381–93.

[51] Hall C et al. Thermal decomposition of ettringite $Ca_6[Al(OH)_6]_2(SO_4)_3\cdot 26H_2O$. J Chem Soc Faraday Trans 1996;92:2125–9.

[52] Skoblinskaya NN et al. Changes in crystal structure of ettringite on dehydration. 2. Cem Concr Res 1975;5:419–31.

[53] Hartman MR et al. The evolution of structural changes in ettringite during thermal decomposition. J Solid State Chem 2006;179:1259–72.

[54] Zhou Q, & Glasser FP. Thermal stability and decomposition mechanisms of ettringite

at < 120 °C. Cem Concr Res 2001;31:1333–9.

[55] Lieber W. Ettringite formation at elevated temperatures. Cem Kalk-Gips 1963;9:364–5.

[56] Warren CJ, & Reardon EJ. The solubility of ettringite at 25 °C. Cem Concr Res 1994;24:1515–24.

[57] Mehta PK. Stability of ettringite on heating. J Am Ceram Soc 1972;55:55–7.

[58] Babushkin VI et al. Thermodynamics of silicates. Springer; 1984.

[59] Nerád I et al. The CaO-Al_2O_3-$CaSO_4$-H_2O system equilibrium states. Cem Concr Res 1994;24:259–66.

[60] Damidot D, & Glasser FP. Thermodynamic investigation of the CaO-Al_2O_3-$CaSO_4$-H_2O system at 50 °C and 85 °C. Cem Concr Res 1992;22:1179–91.

[61] Damidot D, & Glasser FP. Thermodynamic investigation of the CaO-Al_2O_3-$CaSO_4$-H_2O system at 25 °C and the influence of Na_2O. Cem Concr Res 1993;23:221–38.

[62] Kaufmann J et al. Stability of ettringite in CSA cement at elevated temperatures. Adv Cem Res 2016;28:251–61.

[63] Pourchez J et al. Kinetic modelling of the thermal decomposition of ettringite into metaettringite. Cem Concr Res 2006;36:2054–60.

[64] Abo-El-Enein S et al. Thermal and physiochemical studies on ettringite II: dehydration and thermal stability. Cemento 1988;85:121–32.

[65] Ogawa K, & Roy DM. C_4A_3S hydration, ettringite formation, and its expansion mechanism: II. Microstructural observation of expansion. Cem Concr Res 1982;12:101–9.

[66] Hekal EE, & Abo-El-Enein SA. Effect of compression on microstructure and thermal stability of ettringite. Proc. 8th Int. Conf. Cem. Microsc., Orlando, FL, USA: 1986, p. 227–243.

[67] Pollmann H. Characterization of different water contents of ettringite and kuzelite. Proc. 12th Int. Congr. Chem. Cem. Montr. Canada, 2007.

[68] Kira K et al. Dehydration and rehydration of ettringite. Gypsum Lime 1981;1981:7–13.

[69] Tambach TJ et al. A molecular mechanism of hysteresis in clay swelling. Angew Chemie 2004;116:2704–6.

[70] Grier DG et al. Rietveld structure refinement of carbonate and sulfite ettringite. Adv X-Ray Anal 2002;45:194–9.

[71] Robl TL et al. The effect of carbonation reactions on the long term stability of products made from dry FGD materials. Prepr. Pap. Am. Chem. Soc. Div. Fuel Chem., United States: 1996.

[72] Pajares I et al. Evolution of ettringite in presence of carbonate, and silicate ions. Cem Concr Compos 2003;25:861–5.

[73] Carmona-Quiroga PM, & Blanco-Varela MT. Ettringite decomposition in the presence of barium carbonate. Cem Concr Res 2013;52:140–8.

[74] Grounds T et al. Carbonation of ettringite by atmospheric carbon dioxide. Thermochim Acta 1988;135:347–52.

[75] Nishikawa T et al. Decomposition of synthesized ettringite by carbonation. Cem Concr Res 1992;22:6–14.

[76] Chen X et al. Kinetic study of ettringite carbonation reaction. Cem Concr Res 1994;24:1383–9.

[77] Zhou Q, & Glasser FP. Kinetics and mechanism of the carbonation of ettringite. Adv Cem Res 2000;12:131–6.

[78] Hirabayashi D et al. Carbonation behavior of pure cement hydrates under supercritical carbon dioxide conditions–12199, WM Symposia, 1628 E. Southern Avenue, Suite 9-332, Tempe, AZ 85282 (United States); 2012.

[79] Damidot D, & Glasser FP. Thermodynamic investigation of the CaO-Al_2O_3-$CaSO_4$-$CaCO_3$-H_2O closed system at 25°C and the influence of Na_2O. Adv Cem Res 1995;7:129–34.

[80] Dhoury M. Influence of lithium and boron ions on calcium sulfoaluminate cement hydration : application for the conditioning of boron ion exchange resins. Université Montpellier, 2015.

[81] Wang W et al. Synthesis and thermodynamic properties of arsenate and sulfate-arsenate ettringite structure phases. PLoS One 2017;12:e0182160.

[82] Guo B et al. Characterization of the intermediate in formation of selenate-substituted ettringite. Cem Concr Res 2017;99:30–7.

[83] Bonen D, & Sarkar SL. The effects of simulated environmental attack on immobilization of heavy metals doped in cement-based materials. J Hazard Mater 1995;40:321–35.

[84] Tashiro C et al. The effects of several heavy metal oxides on the formation of ettringite and the microstructure of hardened ettringite. Cem Concr Res 1979;9:303–8.

[85] Albino V et al. Potential application of ettringite generating systems for hazardous waste stabilization. J Hazard Mater 1996;51:241–52.

[86] Atkins M, & Glasser FP. Application of portland cement-based materials to radioactive waste immobilization. Waste Manag 1992;12:105–31.

[87] Berardi R et al. Chemical effects of heavy metals on the hydration of calcium sulphoaluminate 4CaO·3Al2O3·SO3. J Therm Anal Calorim 1997;50:393–400.

[88] Chrysochoou M, & Dermatas D. Evaluation of ettringite and hydrocalumite formation for heavy metal immobilization: Literature review and experimental study. J Hazard Mater 2006;136:20–33.

[89] Dunn PJ et al. Charlesite, a new mineral of the ettringite group, from Franklin, New Jersey. Am Mineral 1983;68:1033–7.

[90] Glasser FP, & Zhang L. High-performance cement matrices based on calcium sulfoaluminate–belite compositions. Cem Concr Res 2001;31:1881–6.

[91] Guo B et al. Selenite and selenate uptaken in ettringite: Immobilization mechanisms, coordination chemistry, and insights from structure. Cem Concr Res 2017;100:166–75.

[92] Hassett DJ et al. Synthesis and characterization of selenate and sulfate-selenate ettringite structure phases. Mater Res Bull 1990;25:1347–54.

[93] Peacor DR et al. Sturmanite, a ferric iron, boron analogue of ettringite. Can Mineral 1983;21:705–9.

[94] Peysson S et al. Immobilization of heavy metals by calcium sulfoaluminate cement. Cem Concr Res 2005;35:2261–70.

[95] Pollmann H. Capability of cement-itious materials in immobilization process of hazardous waste materials. Proc. 15th internatio-nal Conf. Cem. Microsc., 1993, p. 108–126.

[96] Klemm WA, & Bhatty JI. Fixation of heavy metals as oxyanion-substituted ettringites. Skokie, IL USA: Portland Cement Association New York; 2002.

[97] Zhang M, & Reardon EJ. Removal of B, Cr, Mo, and Se from wastewater by incorporation into hydrocalumite and ettringite. Environ Sci Technol 2003;37:2947–52.

[98] McCarthy GJ et al. Synthesis, crystal chemistry and stability of ettringite, a material with potential applications in hazardous waste immobilization. MRS Proc 1991;245:129.

[99] Taylor HFW. Crystal structures of some double hydroxide minerals. Mineral Mag 1973;39:377–89.

[100] Gougar MLD et al. Ettringite and C-S-H Portland cement phases for waste ion immobilization: A review. Waste Manag 1996;16:295–303.

[101] Myneni SCB et al. Oxyanion behavior in alkaline environments: Sorption and desorption of arsenate in ettringite. Environ Sci Technol 1997;31:1761–8.

[102] Cornelis G et al. Leaching mechanisms of oxyanionic metalloid and metal species in alkaline solid wastes: A review. Appl Geochemistry 2008;23:955–76.

[103] Kumarathasan P et al. Oxyanion substituted ettringites: Synthesis and characterization; and their potential role in immobilization of As, B, Cr, Se and V. MRS Proc 1989;178:83.

[104] Möschner G et al. Solubility of Fe–ettringite ($Ca_6[Fe(OH)_6]_2(SO_4)_3 \cdot 26H_2O$). Geochim Cosmochim Acta 2008;72:1–18.

[105] Bonhoure I et al. EXAFS study of Sn(IV) immobilization by hardened cement paste and calcium silicate hydrates. Environ Sci Technol 2003;37:2184–91.

[106] Drábik M et al. Thermoanalytical events and enthalpies of selected phases and systems

of the chemistry and technology of concrete part I. calcium-silicate-aluminate-sulfate hydrates. Ceram - Silikaty 2014;58:184–7.

[107] Kuznik F et al. A review on recent developments in physisorption thermal energy storage for building applications. Renew Sustain Energy Rev 2018;94:576–86.

[108] Kazuo S et al. Method For Heat Recovery. JPS5895195(A), 1983.

[109] Pelletier L et al. The ternary system Portland cement–calcium sulphoaluminate clinker–anhydrite: Hydration mechanism and mortar properties. Cem Concr Compos 2010;32:497–507.

[110] Kaufmann J, & Winnefeld F. Seasonal heat storage in calcium sulfoaluminate based hardened cement pastes – experiences with different prototypes. J Energy Storage 2019;25.

[111] TV program “Einstein.” Wunderbeton als Wärmespeicher. SRF TV 2015:March 12.

[112] Ndiaye K et al. Development of a cementitious material for thermal energy storage at low temperature. Constr Build Mater 2020;242:118130.

[113] Mette B et al. Experimental and numerical investigations of different reactor concepts for thermochemical energy storage. Energy Procedia 2014;57:2380–9.

Chapter III. Thermodynamics and kinetics study on ettringite

Based on Publication II:

Investigation on ettringite as a low-cost high-density thermochemical heat storage material: thermodynamics and kinetics

B. Chen[1, 2], K. Johannes[1], L. Ratel[1], M. Horgnies[2], V. Morin[2], F. Kuznik[1]

[1] *Univ Lyon, CNRS, INSA-Lyon, Université Claude Bernard Lyon 1, CETHIL UMR 5008, F-69621, Villeurbanne, France*

[2] *LafargeHolcim Innovation Center, 95 rue du Montmurier BP15, 38291 Saint Quentin Fallavier, France*

The work presented in this chapter was submitted in *Solar Energy Materials and Solar Cells*.

This chapter aims at the development and thermal characterization of pure ettringite powder to study physicochemical properties of ettringite, such as reversible reaction enthalpies, thermodynamic equilibrium, and kinetics of reactions.

As detailed in Chapter 2, the main conversion method of ettringite can be based on solutions and solids. In order to ensure the high purity of ettringite, an adapted solution method is developed with analytical grade materials. The synthetic samples are then ground and analysed the size distribution. To study the thermodynamic and kinetics of dehydration and hydration, the experiment conditions are designed with consideration of real-world scenarios, especially the temperatures of heat resources from solar collectors for charging (dehydration) and room temperatures in winter during the discharging. The partial water vapor pressures are set to maximize the hydration of meta-ettringite for kinetics and changes continuously for the thermodynamics in order to study the variation of the water molecule number in the phases. Thanks to the TGA-DSC equipment coupled with humidity generator, the heat flow of processes can be registered to estimate the enthalpy of reactions.

This chapter is written in the form of a scientific article, which has been submitted. The experimental methods, including the ettringite synthesis and characterization method are firstly presented. Then, the main involved theories for the calculation of thermodynamics are detailed. The experimental results are arranged and discussed to address the particular phenomenon observed in this study.

Individual contribution of involved authors

Together with Dr. Kévyn Johannes (HDR) and Dr. Larysa Ratel, I designed the experiment plan. Then, I performed all experiments and analysed the data. After the scientific discussions with Prof. Frédéric Kuznik, Dr. Kévyn Johannes (HDR) and Dr. Larysa Ratel, I wrote the manuscript. All the authors participated in the revision of the manuscript. Prof. Frédéric Kuznik, Dr. Kévyn Johannes (HDR), Dr. Matthieu Horgnies (HDR) and Dr. Vincent Morin are the supervisors of this study.

3.1 Materials and methodology

3.1.1 Preparation of materials

Aiming at obtaining ettringite of high purity, all reagents used were analytical grade. Calcite was firstly calcined at 1000 °C for 4 h. Once the purity has been confirmed by XRD, CaO dissolved in fresh cold distilled CO_2 free water. The saturated $Ca(OH)_2$ solution was then mixed with $Al_2(SO_4)_3 \cdot 14H_2O$ (8.2 wt.% Al_2O_3) under the stir and N_2 protection at 10 °C for 2h to produce ettringite crystals. After decanting for 3 days, the precipitates were vacuum filtered and washed by cold distilled CO_2 free water and ethanol for two times. At last, the purity of ground solids was defined by XRD and the remains were stored in a desiccator containing saturated $CaCl_2$ solution and N_2 for later use.

3.1.2 Characterization methods

3.1.2.1 Particle size analysation

From laser granulometry analysis on the particle size (Figure III-1), the synthetic ettringite powder is mostly smaller than 125 µm. The mean diameter is about 28 µm.

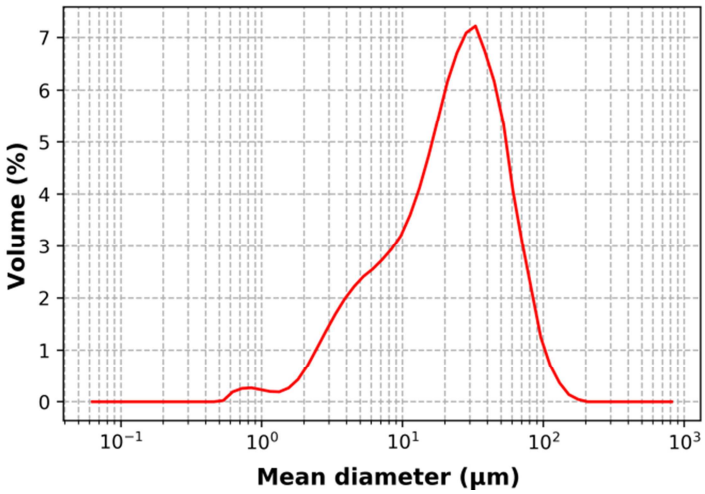

Figure III-1: Size distribution of ettringite particles.

3.1.2.2 XRD analysis

X-ray diffraction analysis (XRD) used in this contribution was to follow the phase assemblage. It was equipped with a Philips/PANalytical X'Pert Pro-MPD Powder Diffractometer

with an X'Celerator detector (CuKα radiation beam, 40 kV and 40 mA). The scanned range is between 2θ = 5–65 ° by a step of 0.25 ° for 40 min in the ambient environment.

3.1.2.3 TGA analysis

The thermal stability of ettringite was characterized by TGA (Mettler TGA/DSC 3+) from 30 to 1000 °C with a heating rate of 10 K/min under a nitrogen flow of 20 ml/min. The quantity of water and carbonate in the samples were then determined thanks to different decomposition temperatures. The water molecule number per mole of ettringite could be calculated by Equation III-1 with the assumption of a perfect metal oxides structure ($3CaO{\cdot}Al_2O_3{\cdot}3CaSO_4$) before 550 °C:

$$n_{H2O} = \frac{(m_i - m_{550\,°C})}{M_{H2O}} \Big/ \left(\frac{m_{550\,°C}}{M_{metal\ oxides}}\right)$$

Equation III-1

Where m_i is the initial mass of sample in TGA, M is the molar mass of substances and n is the water molecule number.

The dehydration and hydration processes were monitored by TGA-DSC (Sensys Evo TG-DSC, Setaram Instrument) coupling with a gas humidity generator (Wetsys, Setaram Instrument). The micro-balance of the instrument was protected by helium. For dehydration, certain amounts of samples were heated at different temperatures with 10 K/min under target humilities controlled by Wetsys with an N_2 flux of 50 ml/min. In terms of hydration, meta-ettringite was firstly produced by dehydrating ~3 mg of ettringite at 80 °C then cooled down to set hydration temperature in dry N_2 environment. Once the temperature stabilized, the humidity generator injected humid N_2 flow containing the target quantity of water vapor into the TGA-DSC for hydrating meta-ettringite. During the thermodynamic experimentations, the end of each process is defined as: the variation of weight is less than 0.04 % during the last hour. It should be noticed that the Wetsys needed about 20 minutes to reach the set values. During all processes, the evolutions of sample masses were continuously recorded. The same white experiments were executed for every thermal characterization. Thanks to the variation of mass, water molecule number in per ettringite molecule could be extrapolated, neglecting the trace of impurities, by Equation III-2:

$$n_{H2O} = \frac{\Delta m / M_{H20}}{m_i / M_{ettringite}}$$

Equation III-2

Where Δm is the variation of mass during certain operations in TGA. The hydration advancement could be inferred as Equation III-3:

$$Hydration\ advancement = \frac{m_{water\ gain}}{m_{ettringite} - m_{meta-ettringite}}$$

Equation III-3

3.1.3 Calculation for thermodynamic equilibrium

The dehydration and hydration process of ettringite can be expressed as Equation III-4:

$$3CaO \cdot Al_2O_3 \cdot 3CaSO_4 \cdot 32H_2O \xrightarrow{\Delta} 3CaO \cdot Al_2O_3 \cdot 3CaSO_4 \cdot XH_2O + (32 - X)H_2O\ (g)$$

Equation III-4

Where X (≠ 0) is the number of residual water molecule in meta-ettringite. The variation of Gibbs free energy ($\Delta_r G^0$) for the above chemical reversible reaction at temperature T could be expressed as $\Delta_r G^0 = -RT\ln K_{eq}$ (Equation III-5). As water vapor being the only reactive gaseous phase in the process, the equilibrium constant K_{eq} could be then simplified as Equation III-6.

$$K_{eq} = \left(P_{eq}(H_2O)/P^o\right)^{32-X}$$

Equation III-6

Where P_{eq} is the partial water vapor pressure (PWVP) at the equilibrium and P^0 is the standard pressure, equivalent 100 kPa. For a reaction at constant temperature and pressure, the Gibbs free energy equation can also be specified in terms of changes in variation of enthalpy $\Delta_r H^o$ and entropy $\Delta_r S^o$ as Equation III-7:

$$\Delta_r G^o = \Delta_r H^o - T\Delta_r S^o$$

Equation III-7

Hereby the correlation of water vapor and temperature for the thermodynamic equilibrium of dehydration and hydration processes is extracted by Equation III-8:

$$\ln K_{eq} = \ln\left[\left(\frac{P_{eq}(H_2O)}{P^o}\right)^{32-X}\right] = -\frac{\Delta_r H^o}{RT_{eq}} + \frac{\Delta_r S^o}{R}$$

Equation III-8

This can be arranged in the form of linear equation as Equation III-9:

$$\ln P_{eq}(H_2O) = -\frac{\Delta_r H^o}{(32-X)RT_{eq}} + \frac{\Delta_r S^o}{(32-X)R} + \ln P^o$$

Equation III-9

The van't Hoff plot of Equation III-9 demonstrates that the logarithmic water vapor pressure is linearly proportional to $\frac{1}{T_{eq}}$ with the slop of $-\frac{\Delta_r H^o}{(32-X)R}$ and intercept of $\frac{\Delta_r S^o}{(32-X)R} + \ln P^o$.

3.2 Results and discussion

3.2.1 Material characterization

The purity of synthesized ettringite is 99.6 % with a trace of $Ca(OH)_2$. The impurity is less than 0.5 % and no need to be accurate in the calculations. No calcium carbonate is detected in XRD (Figure III-2), which is also confirmed in the TGA result: no peak locates between 550 and 1000 °C (Figure III-3) where carbonates are supposed to decompose. The synthetic sample undergoes a total weight loss of 44.8 % (till 1000 °C). Therefore, the synthesized ettringite phase averagely contained 30.6 water molecules (chemical formula: $3CaO{\cdot}Al_2O_3{\cdot}3CaSO_4{\cdot}30.6H_2O$), neglecting the impurity traces. The dehydration could be mainly divided into two stages of water removal. The first step occurs between 30–200 °C with a loss of 36.3 %, which corresponds to 24.8 water molecules. The maximum water removal rate locates at around 130 °C. At the second stage, between 200 and 550 °C, the water loss is 7.9 %, equivalent to 5.4 H_2O.

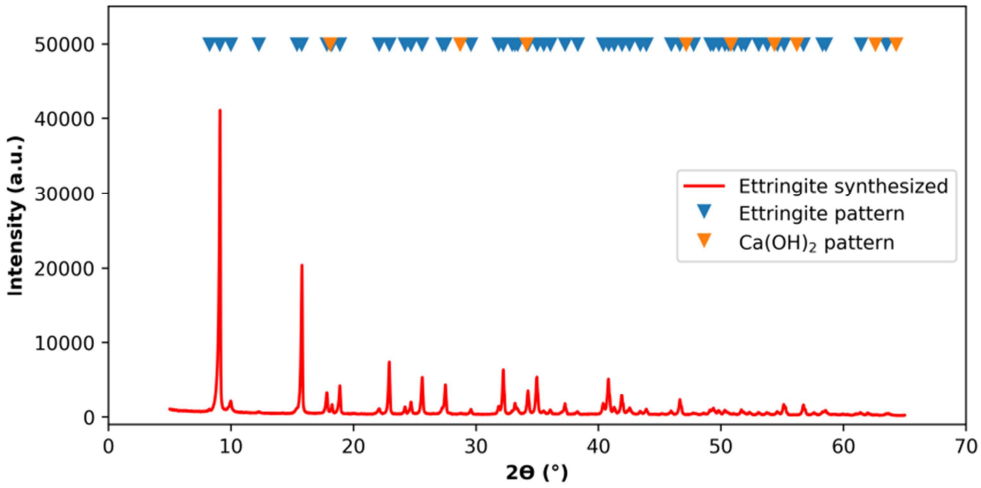

Figure III-2: XRD analysis of synthetic ettringite.

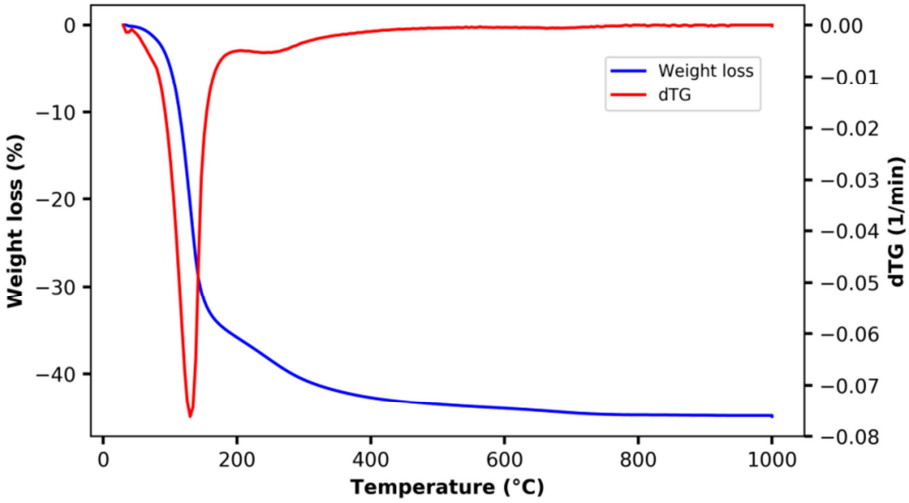

Figure III-3: TGA analysis of synthetic ettringite.

3.2.2 Kinetics of dehydration and rehydration of ettringite

3.2.2.1 Temperature and mass effect on dehydration

Figure III-4 represents the weight loss curves during isothermal dehydration in dry nitrogen for around 10 mg ettringite at different temperatures. The dehydration mostly occurs during the first hour. A higher dehydration temperature leads to a faster dehydration process and higher mass loss. The results are very reproducible at the same dehydration temperature (80 °C). Additionally, a small quantity of samples could accelerate the dehydration behavior but with a similar final water loss level (Figure III-5). The analysis results about dehydration are detailed in Table III-1. The enthalpies, which are proportional to the loss of water molecule number, stabilize around 1260 kJ/mol. It should be noted that the dehydration continued slow-

ly after 15 hours in a dry nitrogen environment. However, the rate is very low and the heat flow is too small to be detected (see in Figure III-7). Considering the rate of dehydration and also the possible damage of the column structure of ettringite caused by high temperature, the dehydration temperature and sample mass are settled at 80 °C and 3 mg for the remaining experiments presented in this chapter. Moreover, under humid N_2, the increase of PWVP only decreases slightly dehydration rate and degree at 80 °C (Figure III-6); because the variation of RH from 4 to 12 mbar H_2O (g) is very little, from 0.8 to 2.6 % RH. Comparing to the 34.1% weight loss at 80 °C in dry N_2, the dehydration at 8 mbar H_2O (g) leads to a lower level of 31.2 %.

Table III-1: Results of isothermal dehydration of ettringite in dry N_2 flux.

Dehydration temperature (°C)	Mass of sample (mg)	Mass loss (%)	Number of residual water molecules	Enthalpies (kJ/mol)
60	10.32	32.2	8.6	1248
80	10.76	33.8	7.5	1241
	10.30	33.5	7.7	1262
	6.70	33.9	7.4	1257
	3.18	34.1	7.3	1290
100	10.48	36.2	5.9	1348

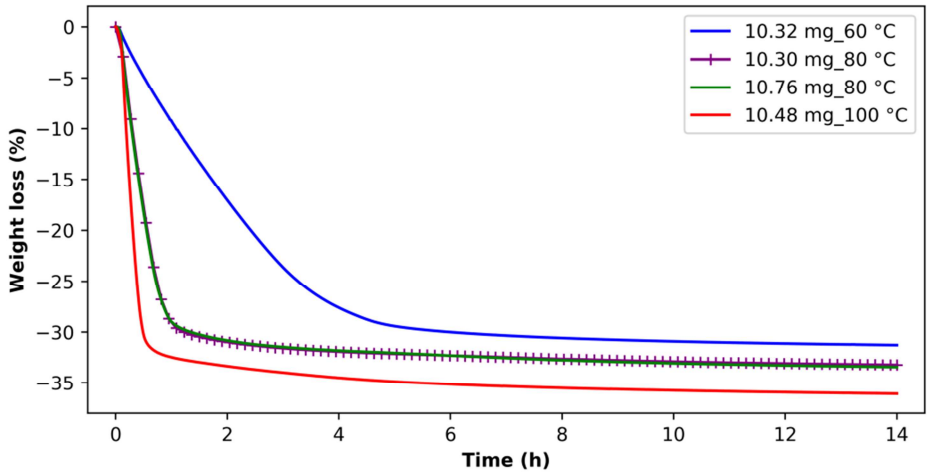

Figure III-4: The effect of dehydration temperature on the dehydration behavior of ettringite in dry N_2.

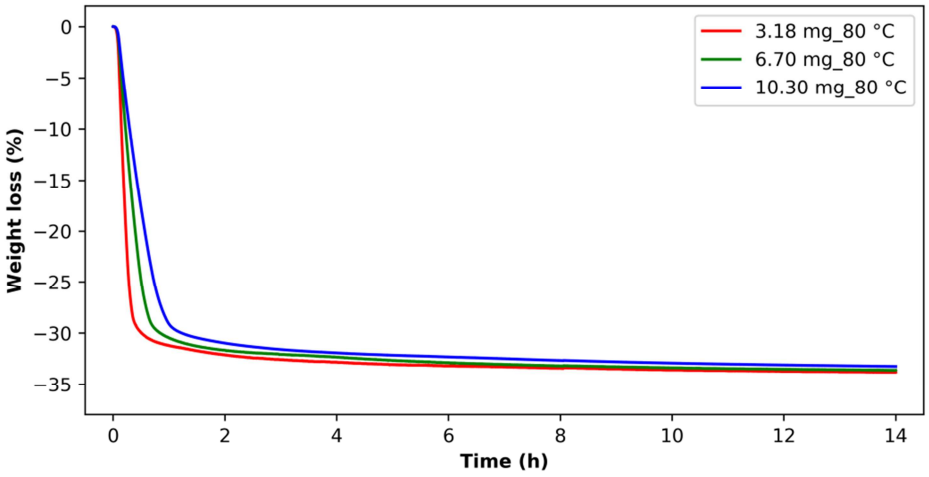

Figure III-5: The mass on the dehydration behavior of ettringite in dry N_2.

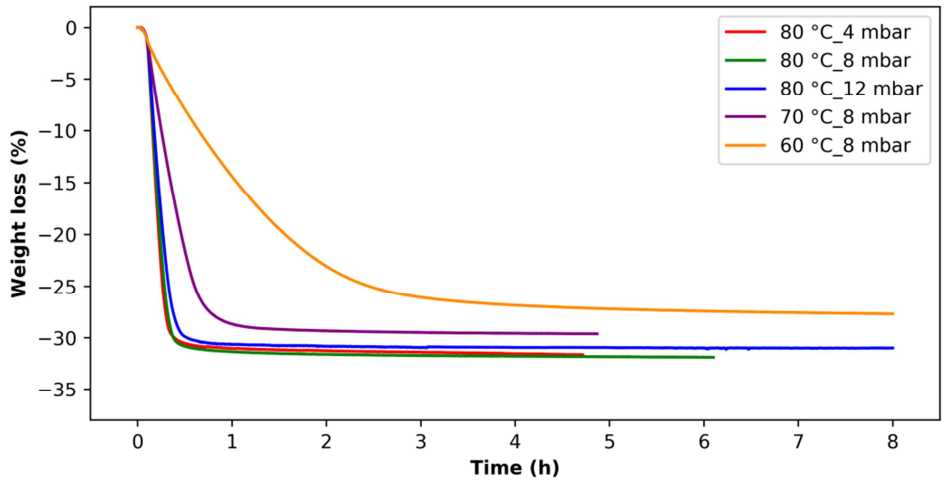

Figure III-6: The PWVP effect on the dehydration behavior of ettringite in humid N_2.

3.2.2.2 Stepwise dehydration process

Given by Figure III-7 the profile of isothermal weight loss curve demonstrates that, the main loss of weight is very continuous without any plateau. However, the peaks on the curve of heat flow derivation (dHF) indicate the rate variation of heat-consuming during the endothermic process at 80 °C in TGA-DSC. The endothermic heat flow change is supposed to be caused by the rupture of different chemical bonds of hydroxyl groups on calcium and oxygen atoms. According to the positions of dHF peaks on time, the weight loss could be separated into four parts corresponding to different losses of water molecule numbers (Table III-2). This process is consistent with theoretical inference in [1–3]. To remove the residual water molecules, a higher dehydration temperature is required. It should be noted that this stepwise dehydration is not like a mono-variant system: no clear boundaries (plateaus) have been detected for each step in the TG signal.

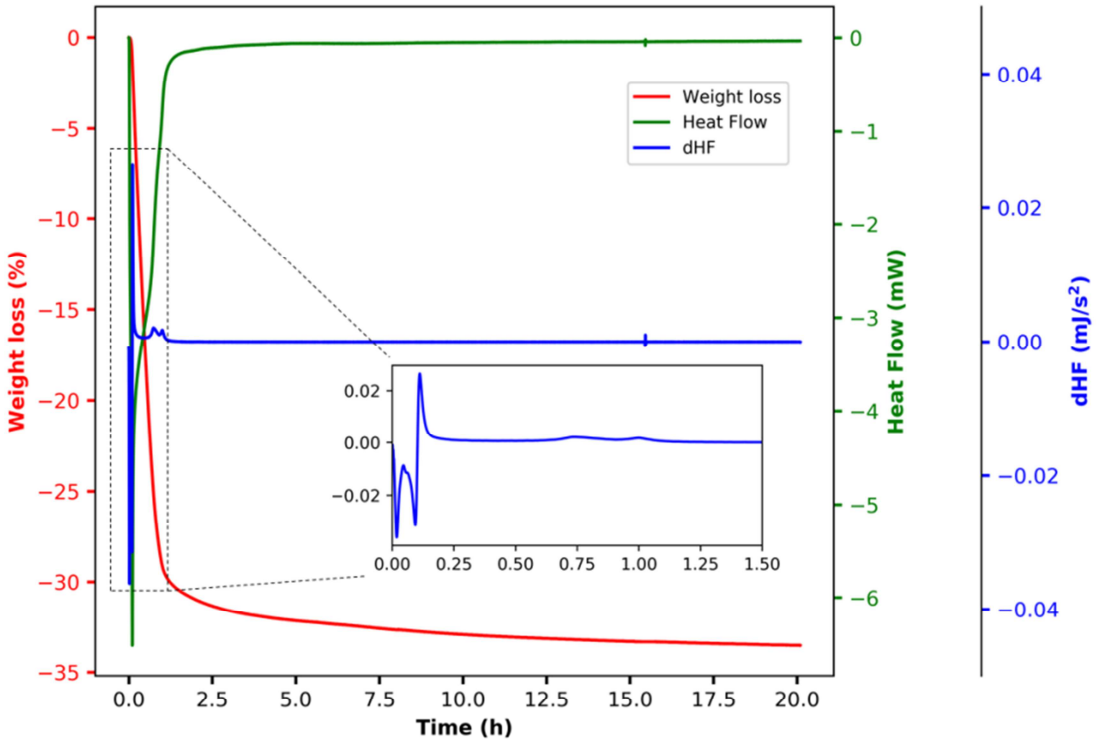

Figure III-7: Possible stepwise dehydration process at 80 °C (dry N_2).

Table III-2: Experimental confirmation on the stepwise dehydration process of ettringite at 80 °C in N_2 flow.

Theoretical inference [1–3]			Experimental results in this study	
Component description	Number of removed water molecules	Location	Component description	Number of removed water molecules
$3CaO{\cdot}Al_2O_3{\cdot}3CaSO_4{\cdot}\mathbf{3}2H_2O$			$3CaO{\cdot}Al_2O_3{\cdot}3CaSO_4{\cdot}\mathbf{30}.6H_2O$	
$3CaO{\cdot}Al_2O_3{\cdot}3CaSO_4{\cdot}\mathbf{30}H_2O$	2	Inter-column channel	$3CaO{\cdot}Al_2O_3{\cdot}3CaSO_4{\cdot}\mathbf{30}H_2O$	0.6
$3CaO{\cdot}Al_2O_3{\cdot}3CaSO_4{\cdot}18H_2O$	12	In the additional vertices of the trigonal prisms	$3CaO{\cdot}Al_2O_3{\cdot}3CaSO_4{\cdot}17.8H_2O$	12.2
$3CaO{\cdot}Al_2O_3{\cdot}3CaSO_4{\cdot}12H_2O$	6	In the main vertices of the trigonal prisms.	$3CaO{\cdot}Al_2O_3{\cdot}3CaSO_4{\cdot}11.7H_2O$	6.1
$3CaO{\cdot}Al_2O_3{\cdot}3CaSO_4{\cdot}6H_2O$	6	In the main vertices of the trigonal prisms.	$3CaO{\cdot}Al_2O_3{\cdot}3CaSO_4{\cdot}7.5H_2O$ *(dehydration process not completed)*	4.2
$3CaO{\cdot}Al_2O_3{\cdot}3CaSO_4$	6	Al and Ca polyhedral	N/A	N/A

3.2.2.3 Rehydration enthalpy of meta-ettringite

Figure III-8 presents the hydration profile of meta-ettringite (from 2.96 mg ettringite as calculation reference) at 20°C and 21 mbar PWVP in order to complete the reversible reaction. During the first 30 minutes, the sorption of water vapor was very rapid given by the slope of curve "degree of hydration advancement" and the instantaneous heat release power could reach up to 1.4 mW. Then the heat flow decreased to about 0.3 mW with a linear increase of mass. After about 2.5 hours, the hydration slowed down and heat release trended to 0 progressively. At 7 hours, the heat liberated by the sorption of water vapor was too weak to be detected by the instrument. The final hydration advancement stabilized at 1.14 which could be converted to around 40 % for weight gain. About 6 % extra weight growth is due to over-hydration compared to mass loss during dehydration. The over-hydration owns to adsorption of zeolitic water molecules which could be as many as 6 instead of 2 in normal ettringite crystal [4]. The cumulated enthalpy of the hydration process is 1370 kJ/mol (~ 547 kWh/m^3 by the mass density of 32-hydrate ettringite) for forming Ett32.4. This final value is indeed bigger since the continuous absorption of 3.6 water molecules (n_{H2O} = 32.4 → 36). However, due to the limitation and incertitude of measurement, the extra heat released is not counted. This kind of over absorption is found in all rehydration experiments if the RH > 76% (Figure III-9). Moreover, the degree of over absorption depends on water vapor pressure. The higher the water vapor is, the more significant the over-hydration. The rate of hydration is similar when hydration advancement inferior to 0.12, which may be attributed to the absorption of water vapor at the surface of particles. Then, it depends on the conditions (temperature and water vapor pressure). The results about rehydration experiments are concluded in Table III-3.

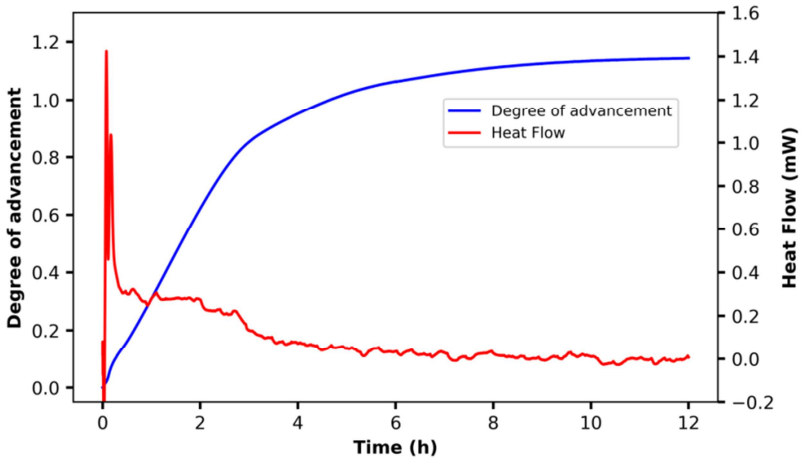

Figure III-8: Degree of advancement and heat flow measured during the hydration of meta-ettringite at 20°C and 21 mbar (90 % RH).

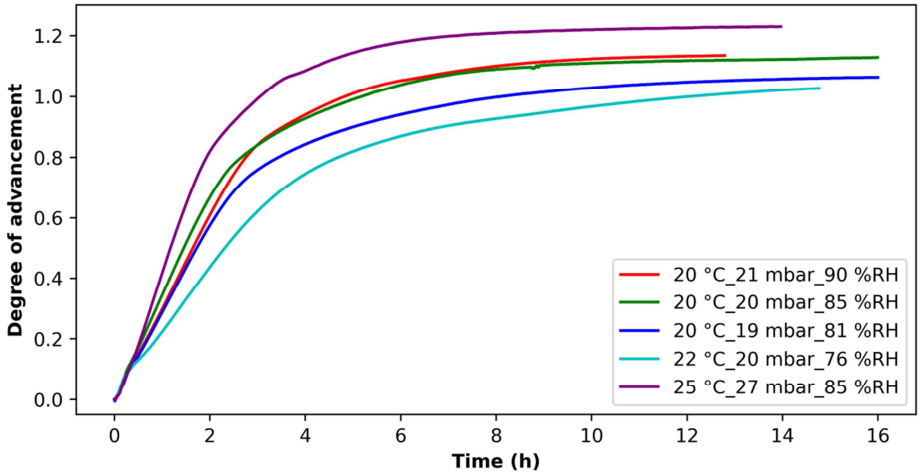

Figure III-9: Variation of the degree of advancement during the hydration of meta-ettringite at various temperatures and PWVPs.

Table III-3: Enthalpies of hydration and regained water molecule number at different temperatures and PWVPs.

Hydration temperature (°C)	PWVP (mbar)	Initial Weight of sample (mg)	Water molecule loss	water molecules gained	Final water molecule number	Enthalpies* (kJ/mol)	Enthalpies (kJ/mol H_2O)
25	27	2.48	22.8	28.1	35.9	1330 (29.6)	60.9
22	20	2.44	23.7	24.4	31.1	1058 (25.8)	55.9
20	21	2.96	23.9	27.4	34.1	1370 (32.4)	53.3
	20	2.84	23.9	27.0	33.7	1341 (31.8)	53.5
	19	2.82	23.8	27.2	33.9	1214 (28.5)	55.9

* The value in the bracket presents the water molecule number in the reformed phase for the corresponding enthalpy.

3.2.3 Thermodynamic equilibrium

3.2.3.1 Dehydration of ettringite

The dehydration of ettringite refers to the loss of zeolitic water in the channel structure and chemically bonded water in the column structure. The number of water molecules (n_{H2O}) in per ettringite and meta-ettringite phases were obtained from several experiments under the ranges of 25–80 °C and 0 (dry N_2 environment)–32 mbar.

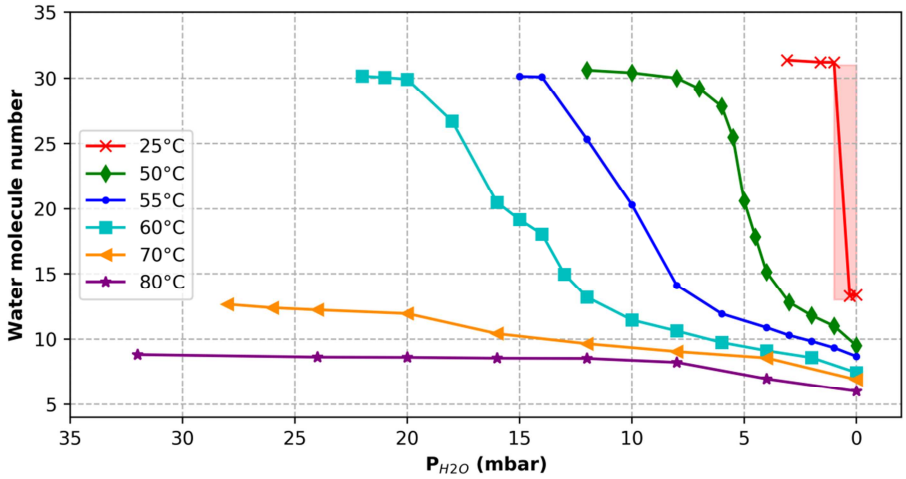

Figure III-10: Evolution of water molecule number in ettringite/meta-ettringite during the dehydration at various temperatures and water vapor pressures.

Figure III-10 shows the corresponding results of water molecule numbers as a function of temperature and PWVPs. The PWVPs, at which ettringite (Ett30) starts to dehydrate, are different at various temperatures. The higher the temperature is, the bigger the water vapor pressure. At ambient temperature (25 °C), ettringite is stable at P_{H2O} as low as 1 mbar (3.2 % RH). Then it dehydrates very slowly to a 13.2-hydrate at 0.3 mbar (1 % RH) for more than one week in TGA-DSC. When temperature increases to 50 °C, ettringite is at P_{H2O} down to 8 mbar, similarly 14 mbar for 55 °C and 20 mbar for 60 °C. Before these PWVPs, the loss of weight is due to the removal of zeolitic water in the channels between ettringite column structures. After these PWVPs, it has been observed that weight loss varies for each change of the PWVPs. The sample shows a bi-variant behavior during the dehydration at 50, 55, and 60 °C at low PWVPs. The equilibrium values of weight loss depend on both temperature and PWVP. Systematic repetitions of experiments have been performed in order to verify whether the obtained experimental values of weight loss corresponded to equilibrium values. At 70 °C and 80 °C, ettringite dehydrates directly to meta-ettringite under given conditions. The water

molecule number in the dehydrated phases are 12.6 for 70 °C at 28 mbar and 8.8 for 80 °C at 32 mbar. This could be explained by that the dehydration energy given is higher than the activation energy of thermodynamic equilibrium to form intermediates observed at 50–60 °C.

Seen from the results of water being regularly removed at 50, 55, and 60°C, the slope break of curves, locating at $n_{H2O} \approx 12$, indicates a different mechanism of losing water molecules before and after this point. When n_{H2O} is higher than 12, the absolute value of the slope of curves is higher than the one of $n_{H2O} < 12$, which means a relatively smaller activation energy needed to remove water molecules until equal to 12. According to [1–3], after the removal of 18 water molecules from Ett30 to Met12, there still remains 6 H_2O bound in the Ca polyhedral of the columns. Comparing to the former bond length of Ca-OH in Ett30, this interatomic distance could be shorter due to the arrangement of structure for a smaller coordination number of Ca. This reorganization may increase the dehydration activation energy for water molecules remained, which leads to a smaller water molecule number removed when $n_{H2O} < 12$. The n_{H2O} at 0 mbar (dry N_2 environment) is lower than the ones in the kinetic study, eg. here $n_{H2O} = 6$ instead of about 7.5 for dehydration at 80 °C. Because a much longer time is required to achieve the thermodynamic equilibrium. The last 6 H_2O correspond to those molecules bonded in the Al and Ca polyhedral [1–3], which means more energy (a higher temperature) is necessary to make them detached than other H_2O in the ettringite crystal.

Overall, four zones can be distinguished in Figure III-10. The first zone is characterized by the continuous removal of zeolitic water of the ettringite. The second zone (light-redden area in Figure III-10) at low temperature (curve at 25 °C) and low water vapor pressure where there is no equilibrium points and can be interpreted as a mono-variant zone (see more in the Section 3.2.3.3). The isotherm at 25 °C is step-shaped meaning that the water vapor pressure of dehydration transformation in this zone is a function of the temperature. In the third zone, at higher temperatures (50–60 °C) and higher water vapor pressure (3–22 mbar) for $13 < n_{H2O} < 30$, the continuous change of the water molecule number with water vapor pressure. Finally, the fourth zone is characterized by the continuous change of water molecules ($6 < n_{H2O} < 13$) with the water vapor pressure for a fixed temperature. This zone can be interpreted as the stability domain for the meta-ettringite phase.

3.2.3.2 Rehydration of ettringite

After being dehydrated to meta-ettringite, the rehydration of ettringite is executed at different temperatures with the continuous growth of water vapor pressures (Figure III-11). At 15 °C, the start point of meta-ettringite is n_{H2O} = 7.4. Once water pressure is presented, the water molecule number per phase increases gradually to 12.1 until P_{H2O} = 8 mbar. Then a plateau is formed between 8 and 10 mbar for Met12.2. After that, a sharp rise is observed even the very small step of the water pressure set (0.2 mbar). The next change point seems to locate at 11 mbar (n_{H2O} = ~ 23) and water vapor is then absorbed steadily to produce higher hydrates. Comparing with the rehydration at 15 °C, the n_{H2O} increases regularly but more slowly at 20 °C since a higher hydration temperature. A similar plateau of n_{H2O} ~ 12 is observed between 12 and 14.5 mbar. After the sudden increase to n_{H2O} = 23 at 15 mbar, the slope of rising reduces at the interval of 15–19 mbar. Differing in the former two cases, the hydration at 25 °C does not reach a plateau after the slow absorption of water vapor to arrive n_{H2O} = 13. After n_{H2O} equivalent to 24, a bigger water vapor pressure step is necessary to make a similar increase in water molecule number in the phase than the ones at 15 and 20 °C. As has been expected, the regular increase of the n_{H2O} has been observed at 30 °C until 25 mbar but the value of n_{H2O} = 12 is not achieved because of required high water vapor pressures.

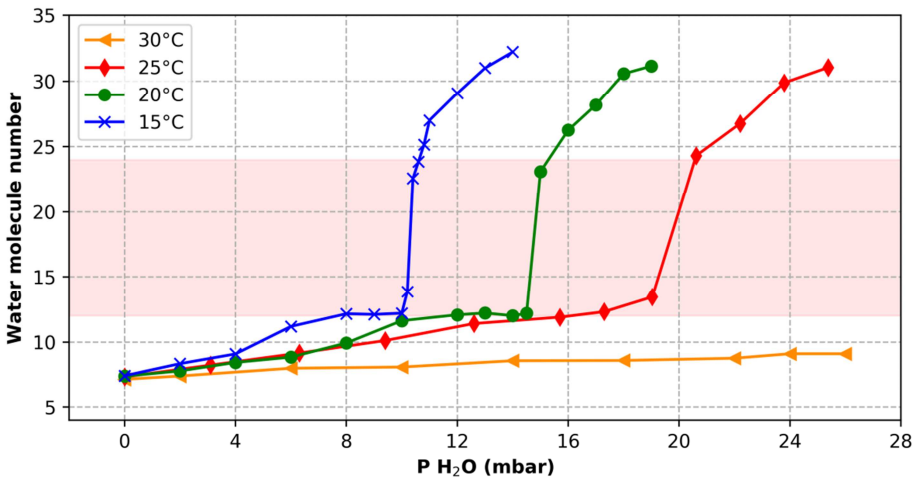

Figure III-11: Evolution of water molecules number in the phases during the hydration at various temperatures and water vapor pressures.

To summarize, the rehydration process can be separated to different steps according to the slope breakpoints: 1) similar to the results of dehydration of ettringite, the water molecules number changes ($7.4 < n_{H2O} < 12$) are observed for each change of the water vapor pressure in the meta-ettringite domain of stability; 2) dramatic increase step to yield a 24-hydrate without any equilibrium points (the light-redden zone in Figure III-11 indicating that the water vapor pressure of a hydration transformation in this zone is a function of the temperature; 3) the last

step to form higher hydrate ettringite for $24 < n_{H2O} < 32$ which can be characterized by a slow kinetic of a reformation of Ett30 [5].

3.2.3.3 Thermodynamic equilibrium of hydration and dehydration

Because of the hysteresis between the hydration and dehydration of ettringite [5], the thermodynamic equilibriums are going to be discussed separately for hydration and dehydration. Figure III-12 extracts the main results of the thermodynamic equilibrium for hydration of meta-ettringite at different temperatures and PWVPs. The process has been carried out in the hydration direction shown in Figure III-12. The water molecule number in the phase increases from 8.4 to 12.2 during the bi-variant behavior. Once stepped in the light-redden zone, it involves a mono-variant change to 23.8-hydrate until to the upper limit of the cyan curve. After that, the samples continue to hydrate in bi-variant behavior including the absorption of zeolitic water. This variation of hydration mechanism is quite different from [5] as mono-variant from the whole process, but similar to the hydration of soluble anhydrite (AIII-$CaSO_4$) to hemihydrate ($CaSO_4 \cdot 0.5H_2O$) [6].

The slopes and intercepts for corresponding curves of hydration are summarized in Table III-4. The activation energy generally decreases with the increasing n. When the water molecule number in the phase is smaller than 12, the activation energy is around 69.5 kJ/mol H_2O. Then the enthalpy value decreases to about 51.6 kJ/mol H_2O for the corresponding dramatic increase of the hydration in Figure III-11. The absorption of zeolitic water contributes 47.9 kJ/mol H_2O. The total exothermic hydration produces 1226.9 kJ/mol (equivalent to 52.0 kJ/mol H_2O). This value is somehow underestimated because of the difficulty to achieve an exact same level of water molecule number for the thermodynamic equilibrium.

The hysteresis reported in [5] between ettringite dehydration and rehydration has been also identified by comparing the results in Figure III-12 and Figure III-13. The dehydration temperatures are much higher for the same water vapor pressures for the reversible process in the hydration or a lower water vapor pressure at the same temperatures. The dehydration activation energy increases erratically to 87.4 kJ/mol H_2O when the n_{H2O} decreases. Same as hydration, the ettringite in dehydration is also proved as a bi-variants system with respect to the thermodynamic study. It should note that the result of dehydration at 25 °C seems to be mono-variant from Ett30 to Met13.3. Therefore, it has not been presented in Figure III-13 and Table III-4.

In the literature, the physically deduced model by Baquerizo et al. [5] limited the hydration of meta-ettringite occurring as mono-variant behavior for Met13 + 17 H_2O → Ett30 (partially shown in Figure III-12. The mathematical approach is $lnP = -6.488 \times 10^3/T + 29.21$. In this study, experimental results demonstrate the variation of van't Hoff equations with the increase of water molecule number. Same as mono-variant for 12.2- to 23.8-hydrate, the approach is $lnP = -6.627 \times 10^3/T + 29.69$, which is very comparable. These similar slopes of curves present similar activation energy of hydration. However, for the higher hydrates of 26.7 and 29.9 H_2O (Table III-4), the results show a slight shift. As for the dehydration of Ett30 to Met13 [5], the model equation is concluded as $lnP = -9.912 \times 10^3/T + 37.30$ (partially shown Figure III-13, while $lnP = -9.875 \times 10^3/T + 37.27$ in this experimental study for ettringite starting to lose structural water. Same as hydration, the dehydration conditions in this investigation are also found stricter than reported in [5]. The curves of different dehydration gather around the physical model as well as hydration curves. It means that once a dehydration temperature of RH given far from equilibrium, these steps could barely be observed. That's why the stepwise dehydration of ettringite is difficult to be proved in the classic experimental studies of TGA and DSC [5,7,8].

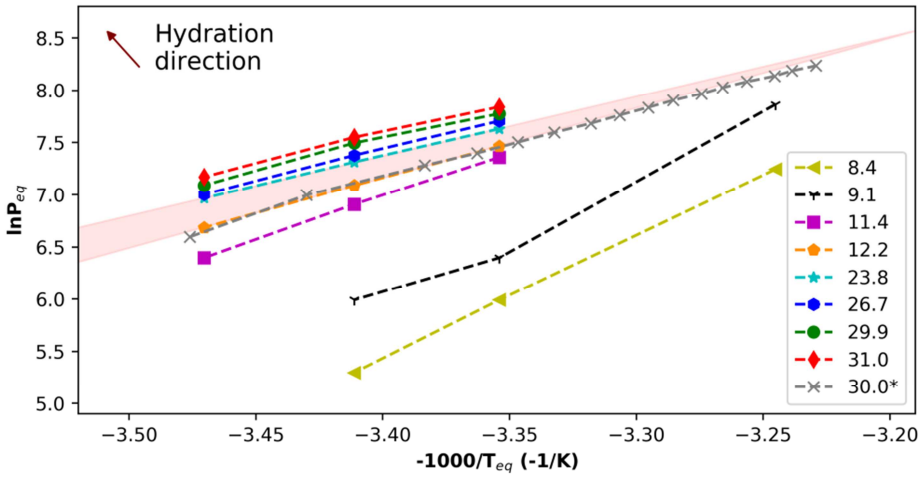

*Figure III-12: Thermodynamic equilibrium of ettringite hydration, in which * is the reversible process of Met13 ↔ Ett30 adapted from [5].*

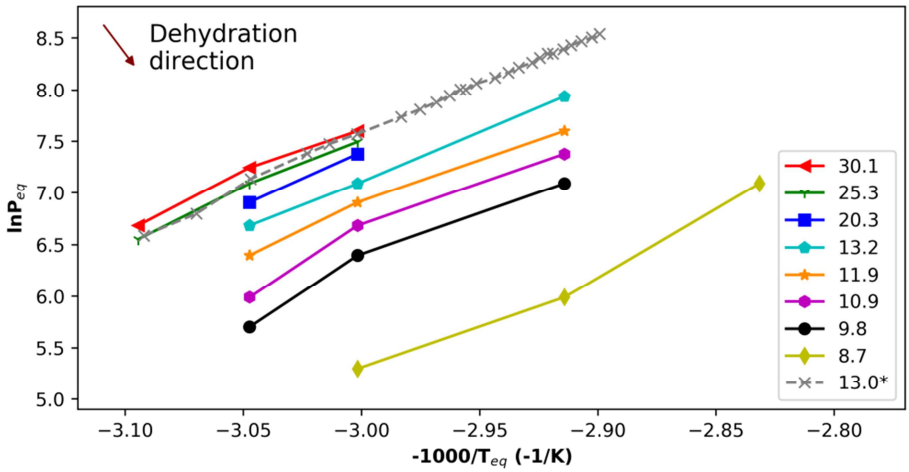

*Figure III-13: Thermodynamic equilibrium of ettringite dehydration, in which * is the reversible process of Ett30 ↔ Met13 adapted from [5].*

Table III-4: Thermodynamic equilibrium results during hydration of meta-ettringite.

Processes	n	Slope (-10^3/K)	Intercept (SI)	R^2	Activation energy ($\Delta_r H^0$, kJ/mol H_2O)
Hydration	8.4	8.402	34.54	0.990	69.8
	9.1	8.423	35.18	0.998	70.0
	11.4	8.266	35.09	0.999	68.7
	12.2-b[1]	6.696	29.93	1.000	55.7
	12.2-m[2]	6.627	29.69	1.000	55.1
	23.8-b[3]	5.709	26.78	1.000	47.5
	26.7	6.034	27.95	0.999	50.2
	29.9	5.889	27.55	0.991	49.0
	31.0	5.758	27.17	0.996	47.9
Dehydration[4]	30.1	9.875	37.27	0.986	82.1
	25.3	10.174	38.06	0.995	84.6
	20.3	10.28	38.22	/	85.4
	13.2	9.442	35.45	0.999	78.5
	11.9	8.890	33.53	0.992	73.9
	10.9	10.08	36.79	0.968	83.8
	9.8	10.08	36.51	0.968	83.8
	8.7	10.51	36.78	0.979	87.4

[1] Upper limits for the bi-variant zone from 7.4 to 12.2 H_2O

[2] van't Hoff plot for the mono-variant zone from 12.2 to 23.8 H_2O

[3] Lower limits for the bi-variant zone from 23.8 to 32 H_2O

[4] The dehydration results at 25 °C (mono-variant) is not used to the bi-variant behaviour

3.3 Conclusions

The present chapter presents the thermal performance of ettringite for heat storage processes. The water vapor pressure and temperature are the two key parameters for the kinetics and thermodynamics of dehydration and hydration. Specially, the thermodynamics of hydration for meta-ettringite is separated into 3 stages: Met7.4 → Met12 → 24-hydrate → higher hydrates including EttX. While for dehydration, the 3 steps are: Ett30.6 → Ett30 → Met12 → Met6 in thermodynamics. The deduced activation energy for hydration reduced when the water molecule number increasing. However for dehydration, the values increase erratically to 87.4 kJ/mol H_2O when n_{H2O} is as low as 8.7. In terms of the kinetics investigation, the removal of water in ettringite is proved as stepwise at 80 °C in nitrogen, which is identical with its crystal structure: Ett30.6 → Ett30 → Met18 → Met12 → Met7.5. Due to being a bi-variant system for dehydration at high temperatures (> 50 °C), this stepwise process is continuous without clear plateaus for each stage. The temperature affects not only the rate of dehydration but also the water removal degree: the higher the temperature is, the higher the rate and the water removal degree are. For rehydration of ettringite, the over-absorption of water is very common when the RH > 76 % without forming a liquid solution. The hydration enthalpy could be 1370 kJ/mol (~ 547 kWh/m^3) for forming Ett32.4 under the operating condition (20 °C and 90 % RH), which is very competitive to other energy storage materials. Therefore, ettringite is very suitable for storing thermal energy; especially during hydration, the no risk of forming an apparent saturated solution makes it easy to control the variation of relative humidity for hydration.

3.4 References

[1] Skoblinskaya NN, & Krasilnikov KG. Changes in crystal structure of ettringite on dehydration. 1. Cem Concr Res 1975;5:381–93.

[2] Skoblinskaya NN et al. Changes in crystal structure of ettringite on dehydration. 2. Cem Concr Res 1975;5:419–31.

[3] Shimada Y, & Young JF. Structural changes during thermal dehydration of ettringite. Adv Cem Res 2001;13:77–81.

[4] Pollmann H. Characterization of different water contents of ettringite and kuzelite. Proc. 12th Int. Congr. Chem. Cem. Montr. Canada, 2007.

[5] Baquerizo LG et al. Impact of water activity on the stability of ettringite. Cem Concr Res 2016;79:31–44.

[6] Preturlan JGD et al. Comprehensive thermodynamic study of the calcium sulfate-water vapor system. Part 1: Experimental measurements and phase equilibria. Ind Eng Chem Res 2019;58:9596–606.

[7] Ings JB, & Brown PW. An evaluation of hydrated calcium aluminate compounds as energy storage media. NASA STI/Recon Tech Rep N 1982;83.

[8] Struble LJ, & Brown PW. Heats of dehydration and specific heats of compounds found in concrete and their potential for thermal energy storage. Sol Energy Mater 1986;14:1–12.

Chapter IV. Comparative kinetics study on carbonation of ettringite and meta-ettringite based materials

Based on Publication III & IV

Comparative kinetics study on carbonation of ettringite and meta-ettringite based materials

B. Chen[1,2], M. Horgnies[2], B. Huet[2], V. Morin[2], K. Johannes[1], F. Kuznik[1]

[1] *Université de Lyon, CNRS, INSA-Lyon, Université Claude Bernard Lyon 1, CETHIL UMR 5008, F-69621, Villeurbanne, France*

[2] *LafargeHolcim Innovation Center, 95 rue du Montmurier BP15, 38291 Saint Quentin Fallavier, France*

This work was submitted in *Cement and Concrete research.*

Study of carbonation durability of several ettringite-enriched pastes

B. Chen[1,2], M. Horgnies[2], V. Morin[2], B. Huet[2], K. Johannes[1], F. Kuznik[1] et al.

[1] *Université de Lyon, CNRS, INSA-Lyon, Université Claude Bernard Lyon 1, CETHIL UMR 5008, F-69621, Villeurbanne, France*

[2] *LafargeHolcim Innovation Center, 95 rue du Montmurier BP15, 38291 Saint Quentin Fallavier, France*

This work was published in *WIT Transactions on Engineering Sciences, 2019, 124: 25-33.*

As mentioned in the conclusion of bibliographic research, the production of pure ettringite is difficult in actual cement plant production lines for large quantities. Therefore, the manufacture of ettringite enriched materials based on commercial cements seems to be a good compromise between production costs and high ettringite contents in the materials. However, carbonation, which modifies the structure and reduces the capacity of energy storage of ettringite, is an essential hindrance to real applications.

The aim of this chapter is then to investigate the carbonation kinetics of three materials in different ettringite contents from commercial high calcium aluminate cements. To approach the use of materials for thermal energy storage, the hydrated cement materials for storing energy and corresponding meta-ettringite-based materials (dehydrated samples for releasing energy) are exposed to different relative humidity (RH) and CO_2 concentrations. The relative humidity is set as three particular scenarios relating to the obtained thermodynamic of hydration in Chapter 3: 1) at 50 % RH for daily ambient humidity; 2) the lower limit 70 % RH for releasing energy and 3) ideal hydration at 90 % RH.

This chapter is arranged in the form of a scientific article. At first, the three used commercial cements are analysed for chemical components. The experiment methodology is then detailed together with different characterisation methods. Due to the variation of sample mass during carbonation (mass transfer of CO_2 and H_2O with the environment), the fraction mineral phases and carbonation degree are specifically recalculated basing on anhydrous binders in order to be comparable for different periods of carbonation. Then, the experimental results and discussion are presented. Particular effort is made on the determination of carbonation effect on the energy storage capacity of materials.

Individual contribution of involved authors

I performed all the experiments with laboratory technician Isabelle Baco. Together with Dr. Matthieu Horgnies (HDR), Dr.Bruno Huet, and Dr. Vincent Morin, I analysed the experimental data and wrote the manuscript. Prof. Frédéric Kuznik and Dr. Kévyn Johannes (HDR) participated in scientific discussions and revised the manuscript.

4.1 Materials and methods

4.1.1 Materials

Three blended cements were used to investigate the carbonation kinetics of ettringite and meta-ettringite that are supposed to be the major phases in hydrated and dehydrated cement pastes, respectively—i) Two made from the mixture of OPC (CEM I 52.5 N) and pre-blended Calcium Aluminate Cement containing calcium sulphate (p-CAC), and ii) A pre-blended Belite-Calcium Sulfoaluminate-Ferrite Cement containing anhydrite (BCSAF). The BCSAF was light brown cement with high ye'elimite content. Chemical compositions and mineralogical phases of the three cements were analysed by X-ray fluorescence (XRF) and X-ray diffraction (XRD), and are shown in Table IV-1. Minor oxides and mineralogical phases were not listed, resulting in total values less than 100 %.

Table IV-1: Percentages (wt.%) of chemical and mineralogical compositions of cements used.

	OPC	p-CAC	BCSAF		OPC	p-CAC	BCSAF
SiO_2	20.25	1.87	12.42	C_3S	70.7	-	-
Al_2O_3	5.44	23.43	16.87	C_2S	7.3	-	30.9
Fe_2O_3	2.48	0.47	6.25	C_4AF	7.4	-	16.4
CaO	64.25	43.17	47.33	C_3A	8.5	-	-
MgO	1.17	0.26	1.44	$C\bar{S}H_{0.5}$	3.2	-	3.7
K_2O	0.22	0.14	0.67	$C\bar{S}H_2$	2.6	-	1.2
Na_2O	0.18	0.05	0.09	$C\bar{S}$	-	52.5	10.7
SO_3	3.33	28.78	9.94	$C_{12}A_7$	-	3.5	-
TiO_2	0.15	1.12	0.88	$C_4A_3\bar{S}$	-	-	31.1
Mn_2O_3	0.10	<0.05	0.06	MgO	-	-	0.5
P_2O_5	0.26	0.05	0.06	Ferro-perovskite	-	-	3.6
Cr_2O_3	<0.05	<0.05	<0.05	Ettringite	-	-	1.5
ZrO_2	<0.05	<0.05	<0.05	Monosulfate	-	-	0.3
SrO	0.06	<0.05	0.13	Amorphous phase	-	44.0	-
Total	97.99	99.54	96.24		99.7	100.0	99.9

4.1.2 Preparation of samples

The p-CAC was manually mixed with 20 wt.% and 40 wt.% of OPC in order to prepare samples with different levels of ettringite, improving mechanical properties and decreasing the risk of self-breakage due to significant shrinkage. The BCSAF was prepared without any other cement. To obtain high porosities [1], demineralised water was used with water to solid ratio (w/s) of 1.1 to hydrate three binders by a VMI/Rayneri mixer at 700 r/min for 3 minutes, then at 1000 r/min for 10 minutes. Before the addition of the blend into demineralised water, a small quantity (0.05 wt.% of blend) of Chryso® Premia 162 was pre-introduced to the water to assure good workability retention. After the addition of cement mixtures, a certain amount of Kelco-Crete® DG-F (0.1 wt.% of water) was added slowly to prevent agglomeration. The used formulas for the different mixtures are summarized in Table IV-2. The cementitious pastes were then poured into polystyrene moulds ($4 \times 4 \times 16$ cm^3) and covered by a glass plate sealed with rubber for 24 h. After that, the samples were demoulded and stored in sealed bags for hydration of 28 days (1 day in moulds and 27 days in sealed plastic bags) at ~ 22°C. In parallel with the preparation of prisms for grains, the same mixtures (3 prisms for each) were also cast for compression strength test.

After 28 days of curing, the prisms were ground in a porcelain mortar with a pestle and passed through sieves of different sizes to collect 1–2 and 2–4 mm grains. Grains were then sealed in plastic bags for later experiments. The hydration of samples was not stopped by organic solutions, to approximate a real-world scenario for energy storage.

Table IV-2. Mixture designs for different pastes preparation of 800 cm^3.

Samples	Main cement (g)	OPC (g)	Chryso® Premia 162 (g)	Kelco-Crete® DG-F (g)	Demineralised water (g)
BCSAF	563.3 (BCSAF)	/	1.14	0.620	618.8
C80P20	451.0 (p-CAC)	112.8	1.14	0.620	619.3
C60P40	342.2 (p-CAC)	223.2	1.14	0.622	621.3

4.1.3 Accelerated and natural carbonation methods

Approximately 150 g of paste of each grain size was oven-dehydrated at 90 °C for 2 days to obtain meta-ettringite-based materials. Approximately 4 g of sample per study case was tiled as a monolayer in an 8 cm aluminum dish. The dehydrated samples as well as corresponding

original hydrated cement samples (1–2 and 2–4 mm) made of the three mixtures listed in Table 3 were then carbonated in a CO_2 chamber (Pharma 600 of Weisstechnik®) at 20 °C, 1 vol.% CO_2, and respective relative humidity (RH, 50 %, 70 %, and 90 %) for different periods from several hours to 28 days. The particle sizes and RHs were set with respect to the internal conditions of an energy storage system. The effects of RHs were studied for each case using non-hydration-stopped samples. As a reference, the same prepared samples sustained natural carbonation in an environmentally controlled chamber (50 % RH, 20 °C, and ~ 0.04 vol.% CO_2) for 0, 11 days, 1, 2, 3, and 6 months.

4.1.4 Characterisation methods

Before experiments on carbonation, compression strength tests (RP 12/50/300 FCC of 3R®) were executed on 3 prims (4 × 4 × 16 cm^3) for each hydrated binder after 7 and 28 days of curing. Mercury Intrusion Porosimetry (MIP), granulometry, and isotherm absorption were also performed on small pieces and grains of materials at 28 days. After each interval of carbonation, the specimens were ground to a powder (< 100 μm) and characterised by TGA and XRD.

4.1.4.1 Thermal characterisation

TGA (Mettler TGA-DSC 3^+) was principally used to quantify the carbonates. An approximately 40 mg sample was added to the device and heated from 30 to 1000 °C at 10 °C/min under a nitrogen flow of 20 mL/min. For cement pastes hydrated by a high w/c ratio, there existed an overlap between weight loss of combined water and CO_2 at 450–550 °C [2]. The range of decarbonisation temperature was thus defined between 550 and 1000 °C. The error in the TGA measurement was approximately 1 %. Due to the bound water release into gas phase as water vapour and weight loss of samples through carbonation experiments, the indicator of carbonation was calculated by normalizing the CO_2 mass gain by the anhydrous content as Equation IV-1.

$$I = \frac{m_{CO2}}{m_{anhydrous\ blend}} = \frac{m_{initiale\ TGA} * (a_{550\,°C} - a_{1000\,°C})}{m_{initiale\ TGA} * a_{1000\,°C}}$$

Equation IV-1

Where I is the CO_2 binding quantity (g CO_2 per g anhydrous mixture), m (mg) is the weight from TGA, and *a* (%) is the weight percentage from TGA.

When preparing the samples, carbonation was hard to avoid. The absolute CO_2 binding quantity (I_r) during experiments was then defined as the difference between the CO_2 binding quantities at each carbonation date (I_t) and at time zero (I_0) in Equation IV-2:

$$I_r = I_t - I_0$$

Equation IV-2

To determine thermal energy storage capacity (TESC), the carbonated grain samples were powdered and characterised by TGA-DSC (Sensys Evo TG-DSC), which provided thermal analysis simultaneous with the loss of weight. Approximately 10 mg of specimen was heated at 80 °C for 5 h with a speed of 10 °C / min from 25 to 80 °C, while the sample was protected by a nitrogen flow of 50 mL / min. Thermal analysis data were acquired by Calisto Acquisition and processed by Calisto Processing (both software) to give loss of weight and enthalpies. The systematic uncertainty in enthalpy measurement was approximately 1 %.

4.1.4.2 XRD analysis

The XRD method used was a semi-quantitative analysis, for not only the mineralogical variation but also mass fraction changes during carbonation. The XRD device used a Philips/PANalytical X'Pert Pro-MPD Powder Diffractometer with an X'Celerator detector of incident CuKα radiation beam by 40 kV and 40 mA to a rotation sample. The specimens were scanned for 40 minutes from 2θ = [5–65 °] by a step of 0.25 ° without protection from CO_2. For dehydrated specimens, the quantity of meta-ettringite was calculated with a nora 35 rutile standard using the external standard method for BCSAF cases and nora 35 for the other two mixtures. Although the semi-quantitative analysis of amorphous meta-ettringite and CSH phases was not accurate for the amounts but the trends of quantity evolution could still be traced.

For the variation of mass caused by water loss during carbonation, the semi-quantitative results were deemed not comparative for different carbonated samples. Hence, the analytical results were recalculated with TGA results (Equation IV-3).

$$X = \frac{X_{XRD} * m_{initial\,TGA}}{m_{anhydrous\,blend}} \times 100\,\% = \frac{X_{XRD} * m_{initial\,TGA}}{m_{initial\,TGA} * a_{1000°C}} \times 100\,\% = \frac{X_{XRD}}{a_{1000°C}} \times 100\,\%$$

Equation IV-3

Where *X* (wc.%) is the recalculated percentage of components relating to the mass of anhydrous blend, X_{XRD} (%) the original component weight percentage from XRD analysis, *m* (mg) and *a* (%) are the weight and weight percentage from TGA, respectively. *X* can exceed 100 % for several components of high content.

4.1.4.3 Theoretical CO_2 binding capacity by XRF

According to [3], the theoretical CO_2 binding capacity (I_{max}, g bound CO_2 / g anhydrous cement) of an anhydrous cement could be approximately inferred from the quantity of its main carbonatable oxides from XRF results (see Equation IV-4) with two assumptions. 1) The sulphate ion only exists in calcium sulphate after a total carbonation of cement pastes, and 2) CaO and MgO are the main carbonated phases.

$$I_{max} = \frac{m_{CO2}}{m_{anhydrous\ mixture}} = \frac{\left(\frac{a_{CaO}}{M(CaO)} + \frac{a_{MgO}}{M(MgO)} - \frac{a_{SO3}}{M(SO3)}\right) * m_{cement} * M(CO_2)}{m_{anhydrous\ mixture}}$$

Equation IV-4

Where m (mg) is the weight from TGA, *a* (%) is the weight percentage in XRF, and M is the molar mass.

4.1.4.4 Granulometry

Granulometry was executed on collected grains by stereoscopic magnifier STEMI SV 11 with a Zeiss electronic fibre optic lighting KL 1500. The 1–2 and 2–4 mm particles were randomly picked for optical observation. After observation of each sample, the Olympus Image Analysis Software carried out measurement for each grain. The approximate maximum and minimum values of 10–30 grains were used to calculate the mean diameter.

4.1.4.5 MIP analysis

MIP tests were carried out on small pieces from prims of hardened pastes of 28 days (4 × 4 × 16 cm^3) using an Autopore IV (Micromeritics, USA). Before testing, samples were dried in an oven at 45 °C overnight. The suggested contact angle for ordinary cement pastes [1] was presumed to be 130 °. On this basis, the pressures used enabled pore diameter coverage of approximately 3 nm–360 µm.

4.1.4.6 Water isotherm absorption

Six samples of 10 g each from the three binders' grains of both sizes were oven dried at 40 °C to extract pore water with soda lime protection for 10 days. Then, each dried sample was separated to 3 samples of approximately 2 g (18 samples in total) and exposed in hermetic chambers at 20 °C under soda lime protection. The RH in chambers were controlled by saturated salts solutions and an internal air circulation, typically $Mg(NO_3)_2$ for 55 % RH, NaCl for 75 % RH, and KNO_3 for 95 % RH [4]. The variation of weight was recorded every week until stable (< 0.1 wt.%). Therefore, liquid saturation degree (S_l) in per gram dry sample is expressed as Equation IV-5:

$$S_l = \frac{m \cdot \rho_{dry\ sample}}{p \cdot \rho_{water}} \times 100\ \%$$

Equation IV-5

Where, m is absorbed water mass (g per g dry hydrated sample), $\rho_{dry\ sample}$ is the dry material density (g·cm^{-3}), p is the porosity (vol. %), and ρ_{water} is the liquid water density.

4.2 Results

4.2.1 Characterisation of reference materials before carbonation

The physical characteristics of the hardened mixtures are summarised in Table IV-3 using methods like theoretical CO_2 binding capacity, water vapour isothermal absorption, MIP, and compressive strength. The grains of different mixtures were generally in the 1–2 mm and 2–4 mm ranges. For C80P20, the mean size was 1.04 mm for 1–2 mm, while it was 2.07 mm for 2–4 mm. Similarly, it was 0.98 mm and 2.50 mm for 1–2 mm and 2–4 mm of C60P40, respectively, 1.13 mm and 2.11 mm for BCSAF. The compressive strengths generally increase with curing time and are the order C80P20 > C60P40 > BCSAF. According to Equation IV-4, theoretical CO_2 binding capacities are approximately 0.25, 0.32, and 0.29 for anhydrous mixtures C80P20, C60P40, and BCSAF, respectively. For each hydrated binder, the quantity of absorbed water vapour at 20 °C increases with the rise of RH. Grains of size 2–4 mm get a higher content of absorbed water vapour than those of 1–2 mm. However, the total absorbed water content for all grains is not significant. Because of their high w/c ratios, the hydrated binders possess porosities 34 %, 38 %, and 54 % for C80P20, C60P40 and BCSAF, respectively. For hydrated mixtures, most pores are in the 0.03–1 µm range and they get less porosi-

ty from micro-pores with diameters smaller than 0.01 µm, or pores with diameters larger than 1 µm (Figure IV-1). No significant pore volume having a mean diameter greater than 0.3 µm is observed. However, BCSAF has the most significant pore volume with a diameter less than 0.1 µm, followed by C60P40, and very few for C80P20. After being dried at 90 °C for two days, the total porosities of C80P20 and C60P40 go up, but the volume of pores of each range also gets bigger. The pore volume for dehydrated C80P20 increases to 0.41 mL/g and is mainly impacted by pores < 0.03 µm and 0.1 < d < 0.3 µm. Dehydrated C60P40 and BCSAF have pore volume rise in all size ranges of pores and they hold similar general pore volume of approximately 0.55 mL/g. Table IV-4 gives the original mineralogical compositions in the samples before carbonation experiments (measurements done by XRD).

Table IV-3. Physical characteristics for three hardened mixtures.*

	Experimental conditions		C80P20	C60P40	BCSAF
Theoretical CO_2 binding capacity (g CO_2 / g anhydrous mixture)	Calculation		0.25	0.32	0.29
Water vapour absorption (wt.% by dry hydrated sample)	55 (5) % RH	1–2 mm	0.27	0.34	0.54
		2–4 mm	0.59	1.02	0.76
	75 (5) % RH	1–2 mm	0.48	0.67	0.88
		2–4 mm	0.83	1.23	1.05
	95 (5) % RH	1–2 mm	2.50	3.88	2.40
		2–4 mm	2.54	3.71	2.68
Total porosity at 28 days (vol.%)	Hydrated (ettringite-based)		34	38	54
	Dehydrated (meta-ettringite-based)		44	54	54
Compressive strength (MPa)	Hydrated pastes at 7 days		14.9 (0.8)	10.2 (0.6)	7.1 (0.3)
	Hydrated pastes at 28 days		15.8 (1.0)	12.0 (0.6)	9.0 (0.6)
Density (g/cm^3)	Hydrated (ettringite-based)		1.25	1.08	1.17
	Dehydrated (meta-ettringite-based)		1.07	0.98	0.94

* The values in parentheses present uncertainty of measurements.

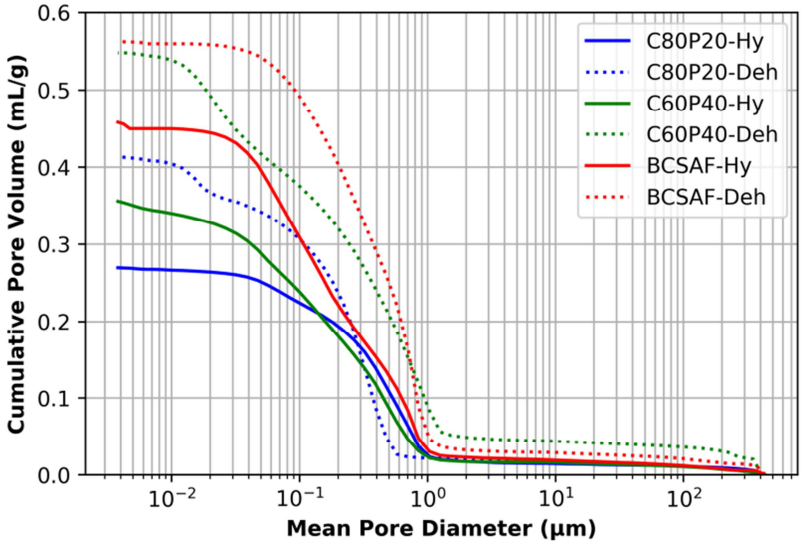

Figure IV-1: Cumulative pore volume of each hydrated and dehydrated pastes, measured by MIP.

Table IV-4: Original mineralogical compositions in XRD of hydrated and dehydrated samples basing on three binders used before carbonation test.*

	C80P20		C60P40		BCSAF	
	Hydrated	Dehydrated	Hydrated	Dehydrated	Hydrated	Dehydrated
C_2S	0.9	1.5	0.8	0.5	5.1	2.3
Monosulfate (12 H_2O)	0.3	1.2	5.8	2.2	3.1	1
Ettringite	75.3	/	67.6	/	45.6	/
Strätlingite	19.3	24	/	/	12.3	7.5
Katoite	/	/	/	/	11.3	14.3
Iron rich siliceous hydrogarnet	/	/	9.8	6.1	18.6	21.3
Monocarbonate	/	/	/	/	0.5	15.4
Hc	0.4	7.6	8.9	18.1	0.8	7.5
Calcite	/	/	1.6	0.2	2.8	0.9
Gypsum	/	/	2.7	3.1	/	/
AH_3	3.7	9.4	/	13.7	0.2	2.4
Amorphous phase	/	56.2	/	56.3	/	29.8

* The components less than 1 % could be neglected in this study; Hc is calcium hemicarboaluminate ($C_4A\bar{C}_{0.5}H_{12}$).

4.2.2 Carbonation results of three binders by TGA

Figure IV-2 shows accelerated carbonation results at 70 % RH and 1 vol.% CO_2 by TGA for the three mixtures of 2–4 mm in different hydration states. Note that t = 0 is noted as t = 0.01

h in the graphs with a logarithmic scale. For hydrated samples (Figure IV-2 a), the slope break points of curves are at 6 h for BCSAF and 24 h for C60P40, while for dehydrated samples (Figure IV-2 b) they are at 6 h for BCSAF and 2 h for C60P40 with respect to 24 h for C80P20 in both cases. Here, the slope break point of carbonation is defined as the point at which the slope of the curve changes significantly in a logarithmic scale plot. The hydrated samples demonstrate a generally larger CO_2 binding quantity and carbonation rate before 24 h than those of dehydrated grains. Specifically, the carbonation rates of dehydrated samples are so small that there is no difference for three binders during the first 2 h, and then the increase of rate is in the order of C60P40 > BCSAF > C80P20. Among them, the carbonation rate of dehydrated C60P40 exceeds even that of the hydrated samples. In fact, almost no water remains in the pores after dehydration. Therefore, it takes some time to absorb enough water and CO_2 to start carbonation. Generally, no obvious difference of CO_2 binding quantity between hydrated and dehydrated samples is observed. For all three samples, carbonation rate during 11 ~ 28 days reduced significantly even if the slope of the curve in logarithmic scale does not change with time. Especially for C60P40, the variation of carbonation degree is very small (~ 0.01). Differing from the other two binders, dehydrated C80P20 presents a high rate of carbonation after 11 days. At 11 days, carbonation degrees of hydrated samples reach values of 38 %, 60 %, and 52 % for C80P20, C60P40, and BCSAF, respectively, while for dehydrated samples, the corresponding values are 25 %, 60 %, and 56 %, respectively. Therefore, C80P20 possesses a higher resistance against CO_2 than the other two binders. Given this fact, only the results of C80P20 will be measured and discussed.

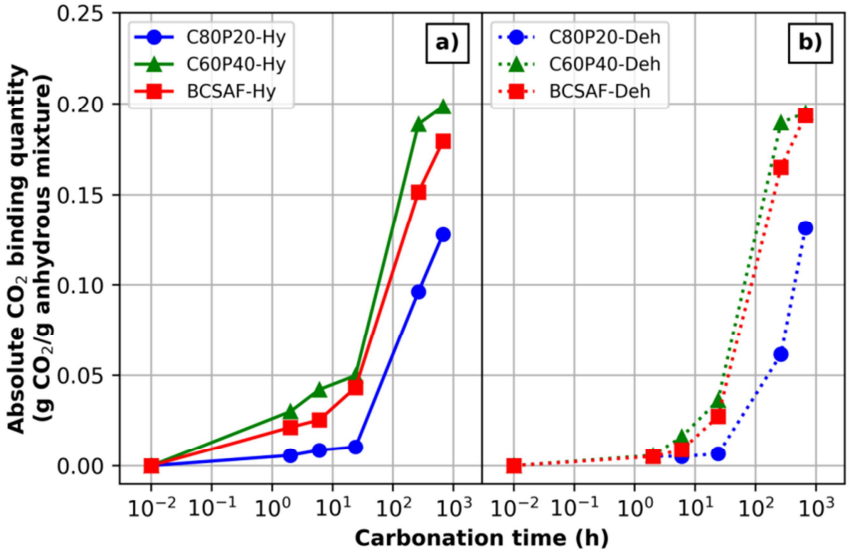

Figure IV-2: Absolute CO_2 binding quantity of hydrated a) and dehydrated b) cement pastes of C80P20, C60P40, and BCSAF of 2–4 mm, as a function of carbonation time at 70 % RH and 1 vol.% CO_2.

4.2.3 Detailed carbonation results of C80P20 by TGA

Figure IV-3 shows the CO_2 binding quantity of hydrated and dehydrated C80P20 for both sizes of particles at different RHs and CO_2 concentrations by TGA. Under 50 % and 90 % RH, the particle size effect is not visible for both states for each duration of carbonation. Under 70 % RH, the difference is more significant after 11 days of accelerated carbonation for both ettringite (~ 0.03) and meta-ettringite (~ 0.05) based cases.

For hydrated samples (Figure IV-3 a), low RH appears to delay the carbonation. The accelerated carbonation of hydrated C80P20 at 50 % RH is very slow. After 11 days, the quantity of bounded CO_2 is approximately 0.02 g per g of anhydrous mixture. Moreover, under 50 % RH, the effect of CO_2 concentration on carbonation of the hydrated samples is not significant. The values of CO_2 binding quantity are 0.03 and 0.01 for accelerated and natural carbonation at 28 days, respectively. When RH increases to 70 %, the slope break point of the degree of carbonation occurs at 24 h, when the quantity accumulation of absorbed CO_2 is very steep. At 28 days, the CO_2 binding quantities are almost the same (0.14 and 0.13) for both hydrated and dehydrated samples. Under 90 % RH, the slope break point advances to 6 h and the CO_2 binding quantity reaches 0.17 after 28 days of carbonation.

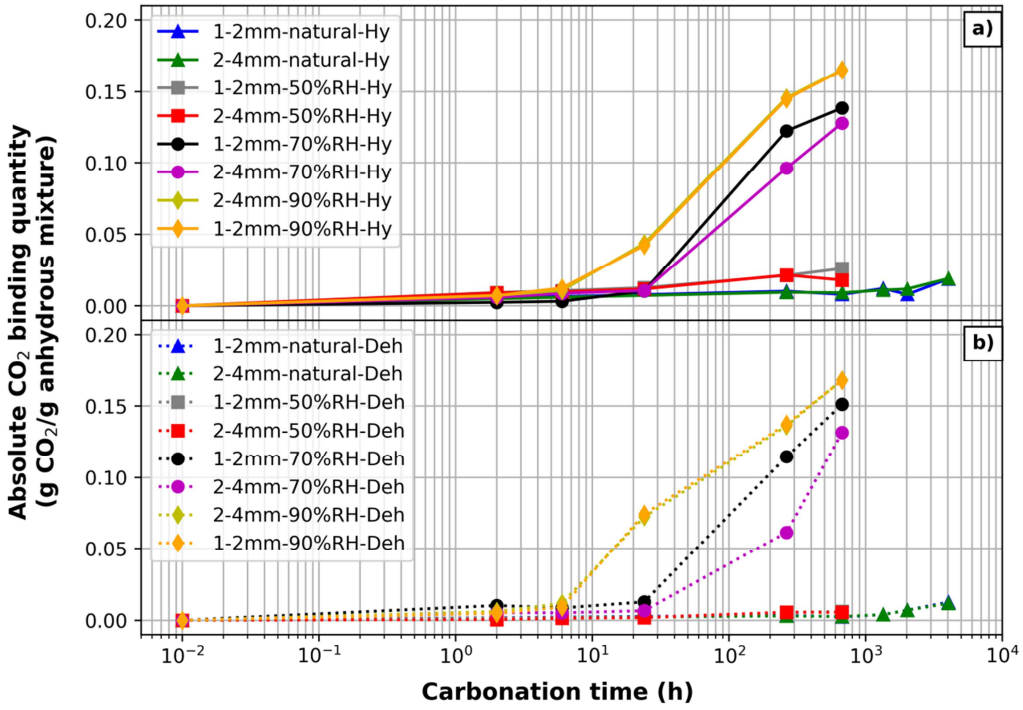

Figure IV-3: Absolute CO_2 binding quantity of a) hydrated and b) dehydrated C80P20 grains of 1–2 and 2–4 mm over carbonation time under natural conditions and accelerated conditions (at various RHs and 1 vol.% CO_2).

For dehydrated pastes (Figure IV-3 b), the values of CO_2 binding capacity at 50 % RH are only 0.005 for accelerated carbonation and 0.003 for natural carbonation at 28 days, which are much smaller than those of hydrated specimens. Compared to hydrated samples, the dehydrated samples demonstrate the following approximate capacities for capturing CO_2 at 28 days: 0.13–0.15 at 70 % RH and 0.17 at 90 % RH for both sizes of grains. Note that for the accelerated carbonation at 1 day under 90 % RH, the dehydrated samples of both sizes indicate a higher CO_2 binding quantity (0.072) than hydrated ones (0.044).

To summarise, a high CO_2 concentration has very little carbonation effect on dehydrated C80P20 samples under 50 % RH but has a more significant effect on hydrated ones. The carbonation rate increases steeply with RH going up. At 90 % RH, the curve profiles of the hydrated and dehydrated samples are alike, and show no effect of gain size.

4.2.4 Carbonation results of C80P20 by XRD

4.2.4.1 Accelerated carbonation at 50 % RH

Figure IV-4 presents the evolution of phase assemblage by XRD as a function of carbonation time for the 2–4 mm C80P20 samples of different hydration states. In the following XRD results, the $CaCO_3$ and $CaSO_4{\cdot}XH_2O$ present the total fraction of polymorphs of $CaCO_3$ and $CaSO_4{\cdot}XH_2O$, respectively. The evolution of carbonate components is very slight for the grains in four cases. For hydrated C80P20 (Figure IV-4 a), the quantity of ettringite decreases slightly, while some monosulfate forms at the very beginning with minor change as time progresses. Besides, a small amount of calcium hemicarboaluminate (Hc, $C_4A\bar{C}_{0.5}H_{12}$) is evidenced at an early stage of carbonation. During carbonation at 50 % RH, calcium carbonates are not visible.

For dehydrated samples (Figure IV-4 b), Hc is formed after oven drying in the presence of fresh air flow and keeps a relatively high level, approximately 8 wc.%, over the experiments and tends to increase at 28 days. Calcium carbonates and calcium sulphate hydrates are not measurable in XRD even after 28 days of accelerated carbonation at 50 % RH. The reformation of ettringite progresses gradually to 14 wc.% at 28 days, while monosulfate crystallises quickly during the initial hours and eventually stabilises at approximately ~ 8 wc.%.

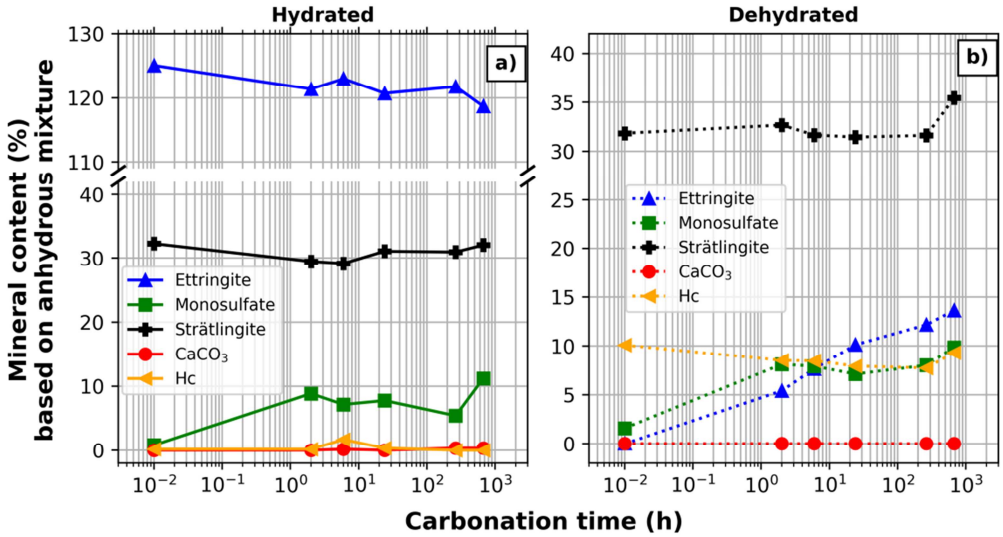

Figure IV-4: Calculated mineralogical contents in a) hydrated and b) dehydrated C80P20 of 2–4 mm after different periods of accelerated carbonation under 50 % RH and 1 vol.% CO_2.

4.2.4.2 Accelerated carbonation at 70 % RH

According to TGA results (Figure IV-3), accelerated carbonation under 70 % RH is significantly greater than it is under 50 % RH. For hydrated samples (Figure IV-5 a), the content of ettringite does not change during the first 24 h, but monosulfate rises to 11 wc.%. Ettringite is then substantially carbonated (55 % of total ettringite) during the following 10 days, accompanied by the depletion of all formed monosulfate. The carbonation process during this period produces 40 wc.% of $CaCO_3$ polymorph, which agrees well with the steep growth of CO_2 binding quantity in TGA at 11 days. All ettringite in the sample is consumed at 28 days, yielding approximately 54 wc.% of calcium sulphate hydrates. Strätlingite is not carbonated over carbonation time and tends to increase.

For dehydrated samples (Figure IV-5 b), the presence of Hc after being dried in the oven is the same as in the 50 % RH case, before entirely carbonating after 24 h. The reformation of ettringite is more rapid than 50 % RH owing to more water vapour available under 70 % RH. However, the quantity of reformed ettringite only reaches 17 wc.% at 24 h. Afterwards, abundant $CaCO_3$ vaterite and aragonite are detected, while monosulfate and ettringite get partly carbonated. Calcium sulphate, being proved as hemihydrate, grows sharply from 24 h. Given the small variation in quantity during the investigation, strätlingite is hardly carbonated. Besides, an increasing trend of strätlingite is found at 28 days of carbonation.

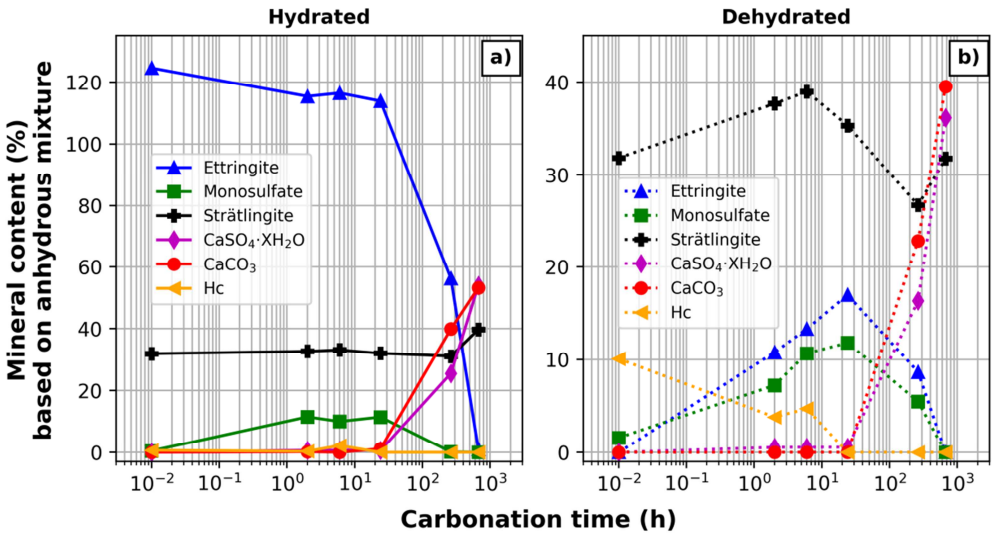

Figure IV-5: Calculated mineralogical contents in a) hydrated and b) dehydrated C80P20 of 2–4 mm after different periods of accelerated carbonation under 70 % RH and 1 vol.% CO_2.

4.2.4.3 Accelerated carbonation under 90 % RH

Similar to the 70 % RH results for hydrated samples, there is a small amount (7 wc.%) of monosulfate formed during the first 6 h, which is then totally reacted at 24 h for hydrated specimens (Figure IV-6 a). However, ettringite is carbonated at the very beginning since a little vaterite and a reduction in ettringite are visible at 2 h. After 11 days of exposure, all the ettringite is depleted. The $CaCO_3$ polymorph and gypsum are essentially produced between 1 and 11 days. Strätlingite starts to react between 11 and 28 days, with no apparent change during the first 11 days of carbonation. An increase of Hc and monosulfate is identified at 11 and 28 days.

In the dehydrated samples (Figure IV-6 b), ettringite reforms maximally around 15 wc.% and 8 wc.% for monosulfate. These two minerals are then totally depleted at 11 days. The preformed Hc is progressively consumed to 0 at 24 h. However, some Hc reforms after 11 and 28 days. Unlike in the hydrated samples, a steep decrease of strätlingite occurs at 11 days and a smaller depletion rate at 28 days. The total amounts of $CaCO_3$ and $CaSO_4$ in dehydrated samples are bigger than those in hydrated ones at 24 h, but being smaller at 11 days while no difference is evident at 28 days. $CaCO_3$ appeared mainly at 24 h, while ettringite was detectable at the very beginning of experiments (2 h). This demonstrates that the rehydration of ettringite is faster than carbonation.

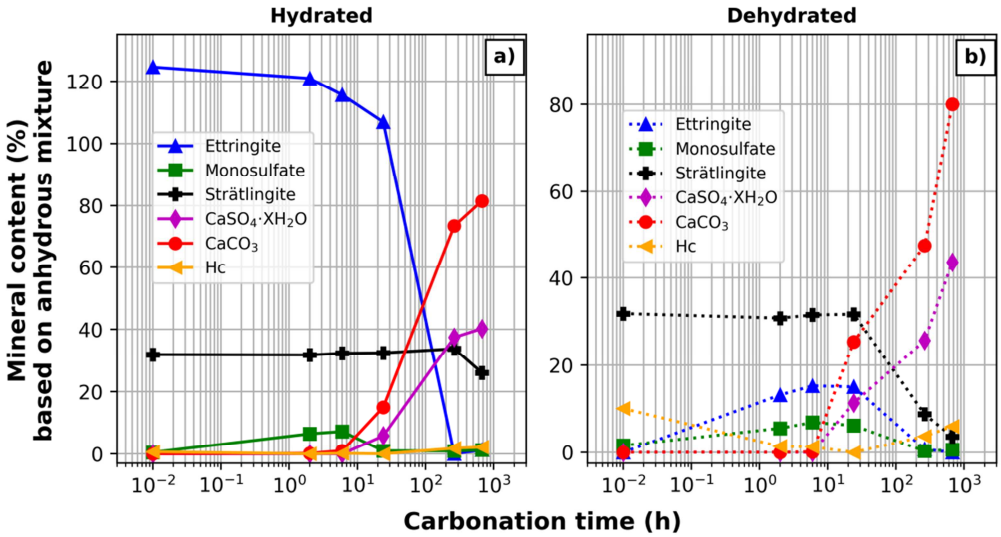

Figure IV-6: Calculated mineralogical contents in a) hydrated, and b) dehydrated C80P20 of 2–4 mm after different periods of accelerated carbonation under 90 % RH and 1 vol.% CO_2.

4.2.5 Carbonation effect on TESC

Since C80P20 was the most resistant to CO_2 among the three binders, its TESC was investigated by TGA through samples with various quantities of bound CO_2 during accelerated carbonation at 70 % RH (Figure IV-7). With reference to the fact that carbon can decompose ettringite irreversibly, it is expected that carbonation yields a decrease of TESC by depleting ettringite. Indeed, in this investigation, the TESC of the 1–2 mm samples reduces with carbonation underway. However, the initial growth of CO_2 binding quantity does not significantly reduce TESC when the CO_2 binding capacity is in the 0–0.075 range. The values stabilise at 880 ~ 890 J /g of anhydrous mixture, after which the TESC drops with an increase in the amount of bound CO_2. For carbonated 2–4 mm samples, the TESC was consistent with the 1–2 mm sample results.

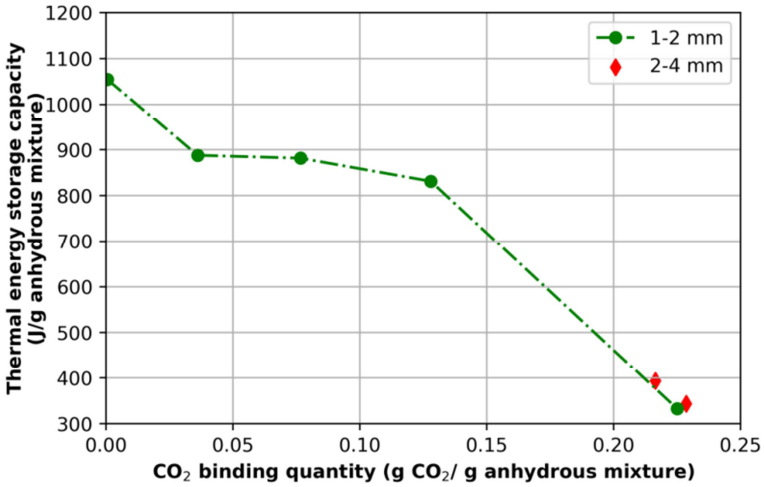

Figure IV-7: Thermal energy storage capacity of C80P20 as a function of CO_2 binding quantity at 70 % RH, 1 vol.% CO_2.

4.3 Discussion

This work studies the carbonation of cement-based materials rich in ettringite/meta-ettringite for potential thermal energy storage use. The evolution of ettringite and carbonate content is discussed, with a comparison of two other materials with high ettringite content. Although ettringite is a dominant phase in these materials, other hydrates like monosulfate, strätlingite, and calcium aluminate hydrates contribute against carbonation to protect ettringite. The influence of CO_2 on the capacity of energy storage is also examined.

4.3.1 Pore size distribution vs. carbonation

Pores with diameters less than 0.1 µm behave like water containers during carbonation. The behaviour of pores as water containers strongly relies on environmental RH, which will be discussed in Section 4.4. Furthermore, more than 60 % of the pores in the samples are larger than 0.1 µm in diameter (Figure IV-1), which ensures an efficient mass transfer of gaseous species via diffusion. For high-ettringite cement pastes of big w/c, the total porosities increase after carbonation and pores, especially with diameters < 0.1 µm, become more coarse [3]. According to [5], ettringite crystals tend to grow (directed or non-directed) in a direction less limited by solid pores, like into or around the pores rather than within the intrinsic solid matrix. This growth of crystals in solid pores can significantly decrease the diameter of micro pores but have less size influence for pores > 0.05 µm. This may explain how the increase of ettringite content in cement pastes could reduce not only the size but also the volume of pores. Besides, ettringite crystals experienced a considerable change of **a** and **c** lattice parameters, which led to a decrease in crystal volume after dehydration [6]. Thus, the size and volume of ettringite-containing pores could be enlarged. Once the ettringite in the pores (d < 0.05 µm) is carbonated, the pores are going to be enlarged. However, the microstructure could be influenced by pre-treatments in a complex way, like during hydration, drying, or pre-carbonation [7]. Finally, MIP cannot quantify all types of pores, which leads to the implication that total porosity is higher.

4.3.2 Comparison of carbonation resistance for three binders

Among the three hydrated cement pastes that sustained accelerated carbonation, C60P40 seemed to be the least resistant against CO_2. This may be somewhat explained by the high calcium silicates' (C_3S and C_2S) content in anhydrous cement yielding C-S-H, which is more

reactive to CO_2 than ettringite. Because of similar quantities of calcium silicates, the carbonation rate of BCSAF sample is comparable with that of C60P40 at an early stage of carbonation. The higher content of ettringite (hydrated) and meta-ettringite (dehydrated) in the C60P40 sample than the BCSAF makes C60P40 bind more CO_2 at 11 days. However, the BCSAF sample yields a higher theoretical CO_2 binding capacity than the C60P40 sample. The reduction of carbonation rate is therefore not as significant as in C60P40. Even the CO_2 binding quantity of BCSAF keeps approximately the same slope from 1 to 28 days, due to the logarithmic scale of time axis in Figure IV-2, while the carbonation rate decreases. The same explanation is applicable for the C80P20 case. Additionally, C80P20 seems to present a lower CO_2 binding quantity and carbonation rate than the other two binders in both hydration states. It was thus the most resistant against CO_2, while C60P40 was the most easily carbonated in this investigation.

4.3.3 Effect of grain size on carbonation

As demonstrated in Figure IV-3, at an appropriate RH (70 %), the small size leads to a higher carbonation degree after 24 h of carbonation. However, the visible differences in results between the samples of different sizes occur at 70 % RH. The influence of size is not observed for low RH (50 %) and high RH (90 %), which may be due to the lack of water supply at 50 % RH, bringing about a too-slow reaction. On the contrary, 90 % RH has a very high carbonation rate. This indicates that the effect of particle size may be controlled by RH and CO_2 concentrations, which could influence the dissolution rate of CO_2. At high RH and low RH, the process of equilibrium of water absorption has little influence on carbonation. However, at 70 % RH, the process of water exchange between pore solution and humid air is significant. Note that the effect of size is more pronounced for dehydrated samples, the largest grain being slower to carbonate at an intermediate age, because achieving water sorption equilibrium needs more time for larger sized grains. Therefore, the carbonation is more significant at this RH.

4.3.4 Influence of RH

Carbonation of cementitious materials essentially depends on environmental RH [8,9]. Galan et al. [10] indicated that carbonation was affected by condensation of water in pores for OPC: 1) Firstly, the lack of water in pores at low humidity to dissolve reactants makes carbonation very slow, and 2) At intermediate RH, i.e., 50–70 % RH, there is enough water and diffusion

space for CO_2 to accelerate carbonation, while a higher RH reduces carbonation speed because water saturation in pores slows it down. This saturation phenomenon may only be suitable for pores of small scale, where saturation of water can block the diffusion of CO_2. In this work, the carbonation of hydrated C80P20 grains (very porous) demonstrates that the higher the RH percentage, the higher the indicator of carbonation. This could be explained by the large porosity contributed by pores with diameters greater than 0.1 µm in samples. With a porosity of 34 % and the presence of pores > 0.1 µm, the transmission of water vapour and CO_2 is assumed to be too fast for the typical diffusion-controlled phenomenon.

Water content is the key for determining the rate with a constant CO_2 concentration. At 50 % RH, the lack of pore solution limits the dissolution of CO_2, while at 90 % RH, a sufficient water content makes the CO_2 concentration the decisive factor of carbonation. When RH keeps at adequate values of 70 %, the equilibrium of water sorption makes the size effect on carbonation visible. This process needs time (the induction period was typically several hours in this study) to achieve the formation of ettringite-saturated pore solution and dissolution equilibrium of CO_2. Typically, the CO_2 binding quantities of hydrated C80P20 at 70 % RH are almost 5 times larger than the ones in samples of the same period at 50 % RH. At 90 % RH, the CO_2 binding quantities are bigger than those at 70 % RH, although the filling rate of pore solution is higher at 90 % RH (Table IV-5). Moreover, the generally low pore-filling rate as well as the high fraction of large pores can ensure good transport of CO_2. The large pore volume contributed by pores > 0.1 µm in C80P20 samples of both hydration states could still lead to an intense carbonation reaction with abundant water supply. Additionally, the average carbonation rate of dehydrated C80P20 between 6 and 24 h is found to be higher than that of the hydrated one at 90 % RH. This is due to carbonation being reinforced along with the reformation of ettringite under high RH. It should be noted that in general, carbonation rate reduces with time. Between 11 and 28 days, the carbonation degree increases significantly more slowly than before, and tends to flatten for both 70 % and 90 % RH.

Table IV-5: Liquid saturation degree of pores by absorbed water for dry hydrated C80P20 using Equation IV-5.

RH (%)		55 ± 5	75 ± 5	95 ± 5
Liquid saturation degree (%)	1–2 mm	1.0	1.8	9.2
	2–4 mm	2.2	3.1	9.3

4.3.5 Influence of CO_2 concentration

The accelerated carbonation under 50 % RH with 1 vol.% CO_2 for hydrated 1–2 mm C80P20 (Figure IV-3 a) is indeed more rapid than natural carbonation for each period because of the CO_2 concentration being 25 times greater. The hydrated samples are carbonated 5 times faster than dehydrated ones with 1 vol.%, while the difference is not significant for natural carbonation. Besides, the carbonation time of hydrated samples to bind with the same amount of CO_2 is approximately 45 times shorter under accelerated carbonation than natural carbonation. However, the difference of carbonation time is only approximately three times shorter for dehydrated samples. Considering the results in Figure IV-3, the storage of C80P20 materials under ambient conditions (20 °C and 50 % RH) makes C80P20 materials of both hydration states reach less than 1 % carbonation degree for 6 months, which will not cause a significant carbonation problem.

4.3.6 Phase assemblage and reaction path

4.3.6.1 50 % RH results

The general outline of TGA results are consistent with the evolution of components clarified by XRD. At 50 % RH, the very slight changes in quantity of carbonates in XRD proved the small increase of TGA curves. Due to the lack of water in dehydrated C80P20 samples, Hc exists during the entire investigation. Besides, the continuous slight increase of CO_2 bonding quantity in TGA cannot be directly confirmed by the increase of carbonation products in XRD. The explanation may be that, on the one hand the detection limit of XRD is not able to indicate the other carbonates, while on the other hand, some CO_3^{2-} substituted minerals exist in relatively low carbonated samples, which are not indistinguishable by XRD, like partially CO_3^{2-} substituted ettringite [6,11,12]. Moreover, the miscibility of CO_3^{2-} in SO_4-ettrignite could be up to 60 % in the ettringite solid solution [13,14]. According to the independent thermodynamic models in [15,16], ettringite may decompose to monosulfate (12-hydrate) at low humidity because of a shift of equilibrium with water activity. This may explain the reformation of monosulfate containing 12 H_2O in hydrated and dehydrated C80P20 samples.

It is worth noting that the reformed “ettringite” in dehydrated samples is a low-hydrate ettringite with less than 30 H_2O, which is given by its wide peak of low intensity in XRD patterns for 50 % RH cases in Figure IV-8. According to [15], the reformed ettringite at approximately 60 % RH presented wide and low counts peaks, which meant the minerals had short-range order, and were not real crystals with long-range order. Thus, it could be a higher hy-

dration degree hydrate (12-hydrate meta-ettringite [15]) with respect to the initial meta-ettringite. It is consistent with the result as actually a 12-hydrate meta-ettringite according to Chapter 3 under such conditions.

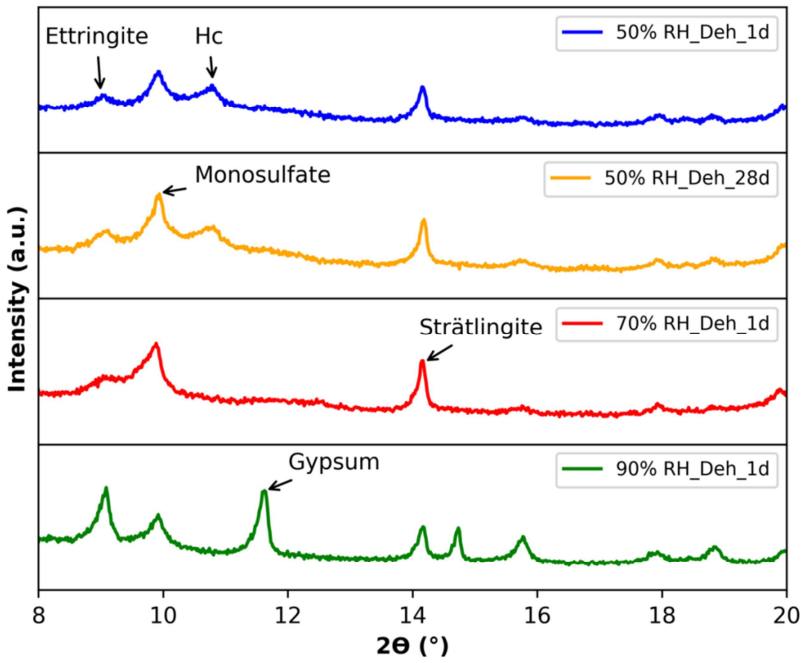

Figure IV-8: XRD patterns of formed ettringite in dehydrated C80P20 grains of 2–4 mm at different dates of carbonation in 1 % CO_2.

4.3.6.2 70 % RH results

When RH increases to 70 %, carbonation is significantly accelerated. Comparing TGA (Figure IV-3) with XRD (Figure IV-5) results, all the slope break points correspond to the beginning of carbonation of ettringite in hydrated samples and reformed ettringite in dehydrated samples, yielding carbonates and calcium sulphate hydrates. Oven-drying the preparation with air circulation carbonates the samples and capture some CO_2, resulting in Hc in the dehydrated samples.

A certain amount of gypsum ($CaSO_4 \cdot 2H_2O$) is produced at 11 days for hydrated samples, while major hemihydrate ($CaSO_4 \cdot 0.5H_2O$) and trace gypsum is present after 28 days of carbonation. Ndiaye et al. [17] found hemihydrate instead of gypsum in an accelerated carbonation of 28 days at 65 % RH for an ettringite-based material. However, the survey [18] on accelerated carbonation (pure CO_2 gas) of a pure ettringite pellet at 68 % RH demonstrated the co-existence of these two calcium sulphate hydrates. Given that the direct transformation from $CaSO_4 \cdot 2H_2O$ to $CaSO_4 \cdot 0.5H_2O$ strictly needs high temperature and low RH [19], the

authors assume that the carbonation leads a nucleation and crystallisation of hemihydrate from a saturated solution due to a local pH and water environment change. Carbonation has actually been reported to increase not only the porosity but also the size of pores [20], especially for gel pores (0.5–10 nm) and capillary pores (10 nm–10 µm). At an early age, water in micro pores (non-evaporable) plays a role in providing a very humid local environment to ensure producing a calcium sulphate di-hydrate. As carbonation proceeds, the collapse of ettringite crystal increases the amount and size of pores and porosity, making the water in pores evaporable. The exchange of water between materials and the environment is important, and the formed oversaturated pore solution forces crystallisation of lower hydrate degree minerals as hemihydrate with respect to gypsum. In the case of dehydrated samples, the lack of water caused by the hydration of dehydrated minerals makes that hemihydrate the only hydrate of calcium sulphate.

From TGA, it is seen that the binding of CO_2 at 70 % RH was more important than it was under 50 % RH. However, the effective diffusivity of CO_2 (0.8 ~ 1.8 vol.%) has no apparent change for high w/c hydrated cement paste at 47–78 % RH [7]. It is then rational to presume that on the one hand, a higher RH makes more water condensed in pores to dissolve CO_2, while on the other hand, the bigger consumption of carbonate ions in the solution at 70 % RH promotes local CO_2 dissolution in water.

4.3.6.3 90 % RH results

At 90 % RH, carbonation is still accelerated compared to the results at 70 % RH. High water supplies and large porosity contributed by pores with diameters greater than 1 µm favour the binding of CO_2 in the samples. Thus, the slope break point is advanced to 6 h (Figure IV-3), and the ettringite and reformed ettringite in samples are totally consumed at 11 d. The reformed ettringite in dehydrated samples exhibiting a narrow and high counts peak in Figure IV-7 suggests a good crystal structure and a higher rate of hydration than carbonation. According to [15], meta-ettringite could be hydrated to a 30-hydrate ettringite at 90 % RH. Therefore, the carbonation of meta-ettringite is actually acting on the reformed ettringite rather than on meta-ettringite with sufficient water supplies. Moreover, the carbonation rate of dehydrated samples younger than one day is indeed higher than the one of hydrated samples, which can be ascribed to the promotion effect by water. It can result in a higher rate of carbonation for dehydrated samples. At 11 days, the quantity of calcium sulphate hydrates in

dehydrated samples is smaller than it is in hydrated samples. This indicates that a part of meta-ettringite is still somehow not carbonated. This meta-ettringite may lead to a local high pH solution once it is hydrated. Moreover, Hc was formed during the conversion of ettringite with reactive carbonates. Note that the final calcium sulphate in samples of both hydration states is proved to be gypsum, which is also indicated in [21,22] at RH superior than 90 %. Meantime aragonite and vaterite are the observed calcium carbonate polymorphs rather than calcite as reported in most investigations [21–23] on carbonation of pure ettringite. Strätlingite is supposed to get carbonated after the disappearance of ettringite and yield vaterite and aragonite as calcium carbonate polymorphs.

4.3.7 TESC vs. CO_2 binding quantity

The first decrease of TESC samples is due to ettringite not being dominant in getting carbonated. This protection may come from not only other hydrates in the samples like monosulfate and CSH, which are carbonated at higher rate than the one of ettringite, but also the possible formation of partial carbonate substituted ettringite. The miscibility of carbonate and sulphate ions could be up to 60 % without influence the number of water molecule [13,14,24]. Once ettringite begins to get carbonated, the reduction of TESC is assumed to be proportional to the increase of the quantity of bound CO_2. Specially, when the CO_2 binding quantity is greater than 0.13, the TESC decreased approximately 5000 J/g bound CO_2 (slope of curve) per gram of anhydrous C80P20 mixture. Moreover, no effect of grain size is observed during carbonation. For samples of different sizes with a CO_2 binding quantity of approximately 0.22, the TESCs are approximately 320 J/g of anhydrous mixture. Although the CO_2 binding quantity approaches the maximal value of 0.25, the rest of non-carbonated minerals and absorbed water are expected to contribute a certain capacity of storing energy. In order to adapt to a real-world scale of application for storing thermal energy, the carbonation kinetics of meta-ettringite enriched materials during usage cycles of hydration by cold humid air and dehydration by hot dry air need to be further examined in a fixed bed reactor for C80P20 samples [25]. Besides, with respect to the value of 1581 J/g $_{3CaO\cdot Al2O3\cdot 3CaSO4}$ adapted from [15] for pure ettringite, the TESC of C80P20 (1054 J/g of anhydrous mixture) is indeed lower due to relatively low ettringite content in composite material and carbonation influence.

4.4 Conclusion

This study significantly advances the understanding of natural and accelerated carbonation of ettringite and meta-ettringite-based material. The current results of carbonation experimentations typically conducted by TGA and XRD lead to the following conclusions.

- ✓ Relative humidity is the key controlling factor of carbonation, whatever the grain size (1 to 4 mm) of ettringite and meta-ettringite-based materials. Both the instantaneous rate of carbonation and the maximum degree of carbonation (up to 80 %) are monotonic functions of relative humidity (up to 90 %).

- ✓ Among the three mixtures investigated, C80P20 possesses a better carbonation resistance than C60P40 and BCSAF thanks to a relatively lower porosity and high ettringite content.

- ✓ The ettringite-based material (hydrated C80P20) undergoes carbonation relatively slowly at 50 % RH, while higher RH can accelerate carbonation. As for meta-ettringite-based materials (dehydrated C80P20), carbonation occurs after hydration, even if it is a low-hydrate ettringite of less than 30 H_2O at low RH. Conversely, 90 % RH hydrates meta-ettringite into crystal ettringite and carbonates as fast as ettringite, given that the hydration process of meta-ettringite is very fast under such RH.

- ✓ For all samples of C80P20 in a natural environment (50 % RH), carbonation is a very slow process. After exposure of 6 months, the hydrated and dehydrated C80P20 materials are carbonated to approximately 6 %. In contrast, the significant CO_2 binding quantity at 90 % RH and 1 vol.% CO_2 of C80P20 samples at 28 days indicates that after release of heat via hydration by humid air, there is strong indication for the material to be stored at low RH (< 50 % RH) or CO_2 free environment aiming at avoiding the carbonation of ettringite and extending service life.

- ✓ The $CaCO_3$ polymorphs formed after carbonation of ettringite and meta-ettringite are confirmed as vaterite and aragonite, while the final polymorph of $CaSO_4$ is hemihydrate at 70 % RH and gypsum at 90 % RH.

- ✓ The reduction of ettringite content caused by carbonation indeed decreases the thermal energy storage capacity of C80P20. When the CO_2 binding quantity is 0.03–0.08, it

could store approximately 890 J/g of anhydrous material. Further loss of energy storage capacity is observed with deepening of the carbonation of C80P20.

4.1 References

[1] Taylor HFW. Cement chemistry. 2nd. London: Thomas Telford; 1997.

[2] Thiery M et al. Carbonation kinetics of a bed of recycled concrete aggregates: A laboratory study on model materials. Cem Concr Res 2013;46:50–65.

[3] Hargis CW et al. Carbonation of calcium sulfoaluminate mortars. Cem Concr Compos 2017;80:123–34.

[4] Greenspan L. Humidity fixed points of binary saturated aqueous solutions. J Res Natl Bur Stand (1934) 1977;81:89–96.

[5] Chinchón-Payá S et al. A comparative investigation of the degradation of pyrite and pyrrhotite under simulated laboratory conditions. Eng Geol 2012;127:75–80.

[6] Chen B et al. Physicochemical properties of ettringite/meta-ettringite for thermal energy storage: Review. Sol Energy Mater Sol Cells 2019;193:320–34.

[7] Houst YF, & Wittmann FH. Influence of porosity and water content on the diffusivity of CO_2 and O_2 through hydrated cement paste. Cem Concr Res 1994;24:1165–76.

[8] Houst YF. The role of moisture in the carbonation of cementitious materials. Int Zeitschrift Für Bauinstandsetz Und Baudenkmalpfl 1996;2:49–66.

[9] Boumaaza M et al. A new test method to determine the gaseous oxygen diffusion coefficient of cement pastes as a function of hydration duration, microstructure, and relative humidity. Mater Struct 2018;51:51.

[10] Galan I et al. Natural and accelerated CO_2 binding kinetics in cement paste at different relative humidities. Cem Concr Res 2013;49:21–8.

[11] Glasser FP. The stability of ettringite. Int. RILEM Work. Intern. Sulfate Attack Delayed Ettringite Form., RILEM Publications SARL; 2002, p. 43–64.

[12] Winnefeld F et al. Carbonation resistance of calcium sulfoaluminate cement mortars. Conf. to Celebr. Centen. LMC Karen Scrivener's 60th Birthd., Lausanne, Switzerland: 2018, p. 243–6.

[13] Pöellmann, H., Kuzel H-J. Solid solution of ettringites Part1: Incorporation of OH^- and

CO_3^{2-} in $3CaO{\cdot}Al_2O_3{\cdot}3CaSO_4{\cdot}32H_2O$. Cem Concr Res 1990;20:941–7.

[14] Barnett SJ et al. An XRPD profile fitting investigation of the solid solution between ettringite, $Ca_6Al_2(SO_4)_3(OH)_{12}{\cdot}26H_2O$, and carbonate ettringite, $Ca_6Al_2(CO_3)_3(OH)_{12}{\cdot}26H_2O$. Cem Concr Res 2001;31:13–7.

[15] Baquerizo LG et al. Impact of water activity on the stability of ettringite. Cem Concr Res 2016;79:31–44.

[16] Albert B et al. Water chemical potential: A key parameter to determine the thermodynamic stability of some hydrated cement phases in concrete? Cem Concr Res 2006;36:783–90.

[17] Ndiaye K et al. Durability and stability of an ettringite-based material for thermal energy storage at low temperature. Cem Concr Res 2017;99:106–15.

[18] Zhou Q, & Glasser FP. Kinetics and mechanism of the carbonation of ettringite. Adv Cem Res 2000;12:131–6.

[19] Clifton JR. Thermal analysis of calcium sulfate dihydrate and sopposed alpha and beta forms of calcium sulfate hemihydrate from 25 to 500 °C. J Res Natl Bur Stand - A Phys Chemmistry 1972;76 A:41–9.

[20] Shah V et al. Changes in microstructure characteristics of cement paste on carbonation. Cem Concr Res 2018;109:184–97.

[21] Grounds T et al. Carbonation of ettringite by atmospheric carbon dioxide. Thermochim Acta 1988;135:347–52.

[22] Nishikawa T et al. Decomposition of synthesized ettringite by carbonation. Cem Concr Res 1992;22:6–14.

[23] Chen X et al. Kinetic study of ettringite carbonation reaction. Cem Concr Res 1994;24:1383–9.

[24] Matschei T et al. Thermodynamic properties of Portland cement hydrates in the system $CaO–Al_2O_3–SiO_2–CaSO_4–CaCO_3–H_2O$. Cem Concr Res 2007;37:1379–410.

[25] Chen B et al. A modular reactor for thermochemical energy storage examination of ettringite-based materials. Proceedings 2019;34:18.

Chapter V. Characterization of an ettringite-based material in an open-mode reactor

Based on Publication V

Characterization of an ettringite-based thermochemical energy storage material in an open-mode reactor

B. Chen[1, 2], K. Johannes[1], M. Horgnies[2], V. Morin[2], F. Kuznik[1]

[1] *Université de Lyon, CNRS, INSA-Lyon, Université Claude Bernard Lyon 1, CETHIL UMR 5008, F-69621, Villeurbanne, France*

[2] *LafargeHolcim Innovation Center, 95 rue du Montmurier BP15, 38291 Saint Quentin Fallavier, France*

The work presented in this chapter was submitted in *Applied Energy*.

After the study on carbonation kinetics in Chapter IV, the cement mixture C80P20 has been proved most CO_2 resistant. Together with high amounts of ettringite after cement hydration, it is then supposed to be the best candidate for thermochemical heat storage in this thesis project. Despite the previous studies on the de/hydration of ettringite in Chapter III, the thermal behaviors of this kind ettringite-based need to be examined.

Consequently, this chapter is dedicated to the thermal investigations of the chosen mixture C80P20. The kinetics of de/hydration for powder samples are firstly studied in TGA-DSC under different conditions (temperatures and partial water vapor pressures). As for the macro-scale study, a fixed bed reactor is designed in the open configuration. Inspired by the LEGO™ construction toys, the main reactor is modularly assembled with designed "standard pieces", in order to be convenient for numerous tests and future possible modification. The granule sample (1–2 mm) is preferred rather than blocks so as to maximize the mass and heat transfer during de/hydration. In order to address daily use and reveal the real potential of the material, the macro energetic performance of the material is investigated under operating conditions relating to several real-world scenarios.

This chapter is written in the form of a scientific article. First, the used materials and experimental methods, as well as the reactor design and data analysis method are introduced. Then, the results of the chemical characterisation of the material, micro-scale thermal characterisations in TGA-DSC, and reactor tests are presented and discussed. In particular, a horizontal comparison for different thermal energy storage projects is completed to prove the potentiality of this cement-based material used for thermal energy storage.

Individual contribution of involved authors

I performed all the experiments. Together with Prof. Frédéric Kuznik and Dr. Kévyn Johannes (HDR), I analysed the experimental data and wrote the manuscript. Dr. Matthieu Horgnies (HDR) and Dr. Vincent Morin, as the co-advisors of the project, participated in the scientific discussions and revised the manuscript.

5.1 Experimental method

5.1.1 Material preparation

A mixture (named C80P20) of Ordinary Portland Cement (20 wt. %) and pre-blended Calcium Aluminate Cement containing anhydrite (80 wt. %) was used to produce high ettringite content materials. The cement mixture was hydrated by demineralized water with high water to cement mixture ratio of 1.1. After 28 days of hydration, the content of ettringite was quantified by X-ray diffraction (XRD). The hardened paste of mixture was further milled down to granules of 1–2 mm in diameter. A few samples were stored in a plastic bottle under the protection of soda-lime and silica gel for TGA-DSC analysis. The rest was stored in sealed plastic bags for later use.

5.1.2 Thermal characterization

The bottle-stored granules were ground down to powder inferior to 0.125 mm in diameter. The thermal characterizations for C80P20 powders were executed in the TGA-DSC instrument under the control of water vapor content (Sensys Evo TG-DSC & Wetsys, Setaram Instrument). To dehydrate the samples, the temperature was rapidly increased to the setpoint with a heating rate of 10 K/min. The environment in the furnace was stabilized at the targeted humidity with an N_2 flow at 50 ml/min. After the removal of water, the dehydrated powder was cooled down to hydration temperature in pure N_2 flux. The hydration then carried out by regulating the Wetsys instrument (Setaram) for delivering a required humid N_2 flow. The degree of advancement (DA) for different processes is defined as Equation V-1:

$$DA = \frac{\Delta m_t}{m_{H2O,loss}}$$

Equation V-1

Where Δm_t is the cumulative weight change at time t and m_{H2O}, loss is the weight loss of water in dehydration.

5.1.3 Reactor conception

Having considered the drawbacks of a closed system, the reactor is designed as an open-mode system with the circuit of ambient air (Figure V-1 a). For storing energy (dehydration pro-

cess), room air is pumped to the heat exchanger and heated up to a temperature similar to a heat source from common solar collectors. The hot dry air flux is monitored by an anemometer and a thermo-hydrometer. The flux is then introduced into the reactor by the three-way valve once the set conditions are achieved. The temperatures of three different positions in the cylindrical reactor (the crosses in Figure V-1 b) are registered synchronously during all experiments. Besides, two thermocouples are respectively installed at the entry and exit of the reactor to measure the fluid temperatures before and after passing through the fixed bed. The end of desorption process is defined as that the relative humidity (RH) is identical in the upstream and downstream pipes. Contrarily, for discharging heat (hydration process), ambient air is firstly stabilized at the desired temperature with the mixture of water vapor supplied by the vapor generator. After reaching the steady state, the humid air is imported into the reactor and hydrates anhydrous materials. The temperature evolution of the fixed bed is collected. Similarly to the dehydration process, the difference of partial water vapor pressure (PWVP) is used to determine the reaction rate of progress. A picture of the reactor is given in Figure V-1 c. For all tests, the reactor is insulated by 5 cm thick glass wool. The measurement ranges, as well as the uncertainty of the sensors, are detailed in Table V-1. The time step of measurement is set to 2 s. The upside door of the isothermal room (Figure V-1 d) is closed to keep a constant temperature around the reactor during all experiments.

Table V-1: Measurement range and uncertainty of the probes.

Probe	Measurement range	Uncertainty
Thermohygrometers (Rotronic, HygroClip type HC2-IC102)	-100–200 °C	± 0.1 °C
	0–95 % RH	± 0.8 % RH
Thermocouples (Type K)	0–100 °C	± 0.1 °C
Propeller anemometer (Schiltknecht, MiniAir20, steel)	40 m/s	1.5 % of measurement

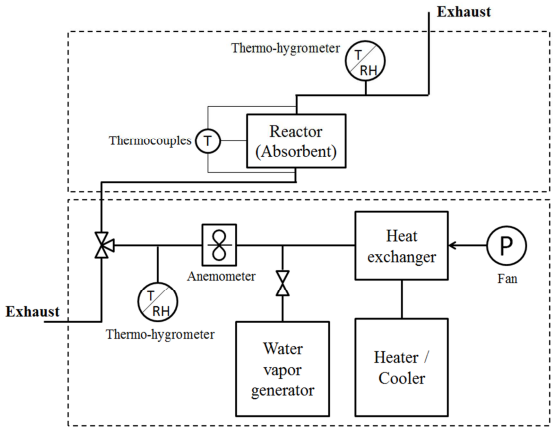

(a) Schematic diagram of reactor system

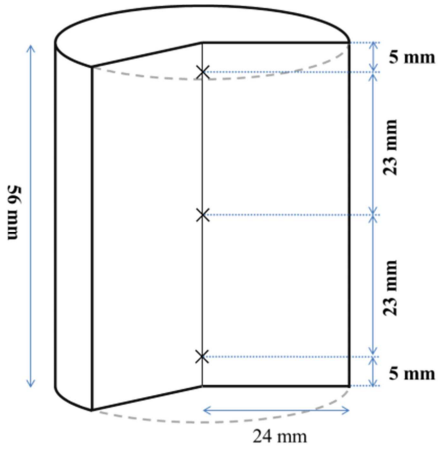

(b) Positions of thermocouples in the cylinder reactor

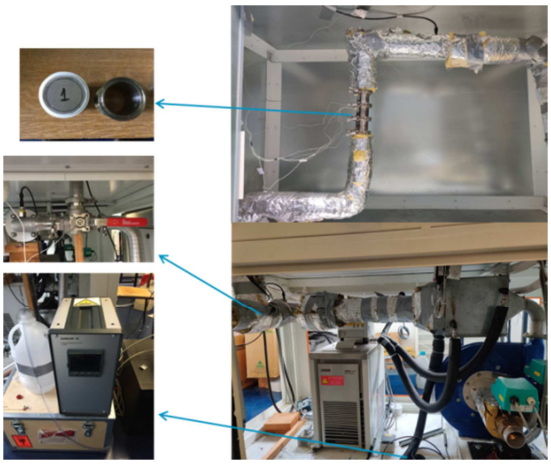

(c) Photos of the prototype

(d) Isothermal room for reactor

Figure V-1: Detailed design for the fixed-bed reactor set-up.

5.1.4 Reactor test conditions

The kinetics of dehydration and hydration of the composite material is controlled by multi-parameters of the working fluid at the inlet of the reactor, such as temperature, humidity, and airflow. During each experiment, about 75 g of C80P20 grains filled the cylinder reactor. For dehydration tests, the initial RH was not considered because the ambient water vapor content in the laboratory does not result in a significant difference in RH at high temperatures. An experimental design has been carried out on the de/hydration temperature, flowrate and RH. Dehydration temperatures have been set according to the outlet temperatures achievable by a classical solar air collector. After dehydration, the air flowrate is turned off and the samples are cooled down by natural convection with the ambient environment. The door of the isothermal chamber is opened without unloading insulation. This step is important to mimic seasonal heat storage where charging sensible heat is lost. For hydration investigations, the temperature of the inlet humid air was pre-stabilized at 20 °C which is the set point temperature

in a building during winter [1]. Besides, a comparison test of hydration at 15 °C is executed. The RH of fluid was controlled at around 90 % in various flowrates. The operating conditions of these de/re-hydration tests are summarized in Table V-2. It is worth noting that the dehydration and hydration tests were carried independently.

Table V-2: The operating conditions set for reactor tests.

Test number	Dehydration		Test number	Hydration		
	T [°C]	Flowrate [$m^3 \cdot h^{-1}$]		T [°C]	RH [%]	Flowrate [$m^3 \cdot h^{-1}$]
1	75	5	6	20	90	5
2	85	5	7	20	90	3
3	95	5	8	20	80	5
4	95	6	9	15	90	5
5	95	7.5	/	/	/	/

5.1.5 Data processing method

As shown in Figure V-1, the measuring devices during the reactor tests gave the following values:

- ✓ the RH of the fluid at the inlet ϕ_{inlet} and outlet ϕ_{outlet} of the system [%];
- ✓ the air temperature at the inlet T_{inlet} and the outlet T_{outlet} of the system [°C];
- ✓ the airflow rate Q_V in the system [$m^3 \cdot h^{-1}$];
- ✓ the temperature of the air entering the reactor T_{in} and exiting the reactor T_{out} of the system [°C];
- ✓ the temperatures at different positions in the reactor [°C]

The partial water vapor pressure, P [Pa], at the inlet and outlet of the system are calculated as Equation V-2 and Equation V-3:

$$P_{inlet,H2O} = P_{sat,T_{inlet}} \cdot \phi_{inlet}$$

Equation V-2

$$P_{outlet,H2O} = P_{sat,T_{outlet}} \cdot \phi_{outlet}$$

Equation V-3

The saturated water vapor pressure $P_{sat,T}$ [hPa] at absolute air temperature T [K] can be drawn from Goff-Gratch equation (Equation V-4) [2]:

$$logP_{sat,T} = -7.90298\left(\frac{T_{st}}{T}-1\right) + 5.02808\log\left(\frac{T_{st}}{T}\right) - 1.3816\times10^{-7}\left(10^{11.344\left(1-\frac{T}{T_{st}}\right)}-1\right) + 8.1328 \times 10^{-3}\left(10^{-3.49149\left(\frac{T}{T_{st}}-1\right)}-1\right) + logP_{st}$$

Equation V-4

where T_{st} is the steam-point of 373.15 K at 1 atm, P_{st} is the $P_{sat,T}$ at the steam-point pressure.

The water absorption rate $\dot{m}_w$ is defined as the variation rate of water vapor content between the inlet $\dot{m}_{inlet}$ and outlet $\dot{m}_{outlet}$ in Equation V-5. R is the ideal gas constant equal to 8.3145 J/(mol·K). Thus, the quantity of absorbed water could be inferred by the integration of $\dot{m}_w$.

$$\dot{m}_w = \dot{m}_{inlet} - \dot{m}_{outlet} = \frac{P_{inlet,H2O}\cdot Q_V \cdot M_{H2O}}{R\cdot T_{inlet}} - \frac{P_{outlet,H2O}\cdot Q_V \cdot M_{H2O}}{R\cdot T_{outlet}}$$

Equation V-5

The usable system output power P_s [W] is estimated by Equation V-6 based on the sensible heat of air flow composed of dry air and water vapor:

$$P_s = Q_V \cdot \rho_{dry\ air}\cdot C_{p,dry\ air}\cdot(T_{out}-T_{in}) + \dot{m}_{outlet}\cdot C_{p,water\ vapor}.T_{out} - \dot{m}_{inlet}\cdot C_{p,water\ vapor}.T_{in}$$

Equation V-6

Where the specific heat capacity of air $C_{p,\ dry\ air}$ and of water vapor $C_{p,\ water\ vapor}$, dry air density $\rho_{dry\ air}$, molar mass of water vapor M_{H2O} and the variation of temperature (T_{out}–T_{in}) between the inlet and outlet of the reactor. The quantity of discharging energy Q [J] is calculated as the following integral on the observation duration (Equation V–7):

$$Q = \int P_s \cdot dt$$

Equation V-7

5.2 Results and discussion

5.2.1 Ettringite content by XRD

After 28 days of hydration curing, some materials were collected and ground to powder (< 100 µm) for the semi-quantitative XRD analysis. The percentage was determined based on the most strong peak area and standard relative diffraction intensity for each mineral. Therefore, the ettringite content in the materials was then confirmed as 71 wt.%.

5.2.2 TGA-DSC analysis

5.2.2.1 Dehydration analysis

Dehydration tests have been carried out to study the influence of temperatures and PWVPs on the removal of water pore solution and structure water molecules. Figure V-2 represents the kinetic results of different dehydration experiments. The degree of advancement (DA) is normalized by the respective total weight losses. The decreasing pressures of water vapor from 1200 to 400 Pa delivered into instruments in this study have a minor effect on the dehydration rates and the degree of water removal at 80 °C. The final water removed level stabilizes at 21.3 % for 800 and 1200 Pa while the value reaches 21.4 % for 400 Pa after 1.5 hours (see Table V-3). The average endothermic energy is about 715 J/g of initial hydrated materials. In the case of dry N_2 only, the water loss reaches 25 % after 4 hours with an enthalpy of 811 J/g of hydrated materials, which is equivalent to a material energy storage density of 286 kWh/m^3.

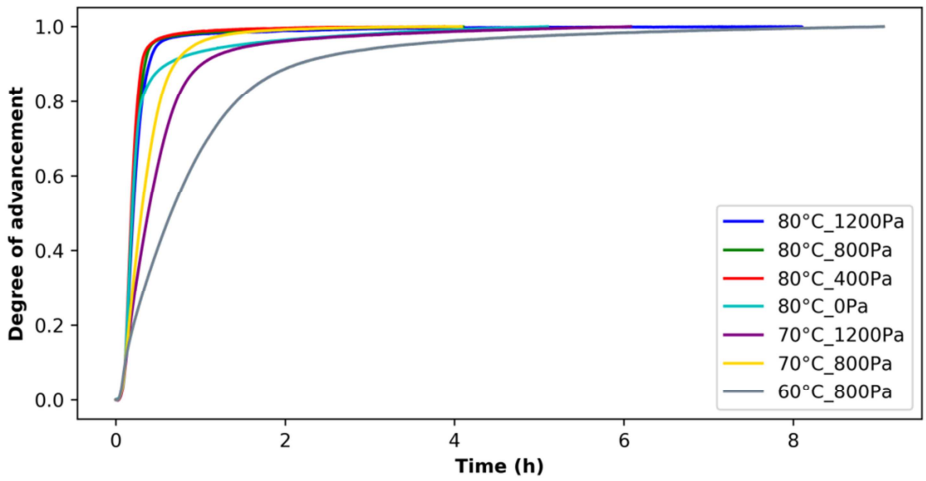

Figure V-2: Dehydration of powder sample at various temperatures and PWVPs in the TGA-DSC.

Table V-3: Dehydration results for C80P20 powders.

Dehydration temperature (°C)	PWVP (Pa)	Final weight loss (%)	Enthalpy ($J/g_{\text{initial hydrated material}}$)
80	1200	21.3	714
	800	21.3	703
	400	21.4	729
	0	25.0	811
70	1200	18.9	605
	800	20.3	667
60	800	16.5	570

Figure V-3 shows the tested equilibrium states of ettringite on the phase diagram. The dehydration points from 400 to 1200 Pa cluster near the thermo-equilibrium of the 9-hydrates meta-ettringite. For dry N_2 (treated as 0.01 Pa PWVP), the distance from the thermo-equilibrium increases the weight loss by 3.6 %. At 70°C, the material dehydration is more affected by the water vapor pressure. A higher PWVP decreases not only the dehydration rate but also the water loss level. Same under 800 Pa of PWVP, it cost 7 hours to dehydrate the samples at 60 °C for the only removal of 16.5 % while 20.3 % for 70 °C for 2 hours. This lower weight loss trend as a function of temperature is caused by the approach of operating condition to the limit of ettringite dehydration. For the dehydration points, it can be assumed that there is a zone where the reaction is di-variant [3]. The endothermic energy during the process is linear with mass loss (Figure V-4). The relative equation is assumed as $\Delta H = 30.321 \times W_{loss} + 58.788$ with the determination coefficient (R^2) of 0.962. It is worth mentioning that the slope of the linear curve corresponds to a reaction enthalpy of 54.6 kJ/mol H_2O, value that is in good agreement with other hydrated salts from the literature [4].

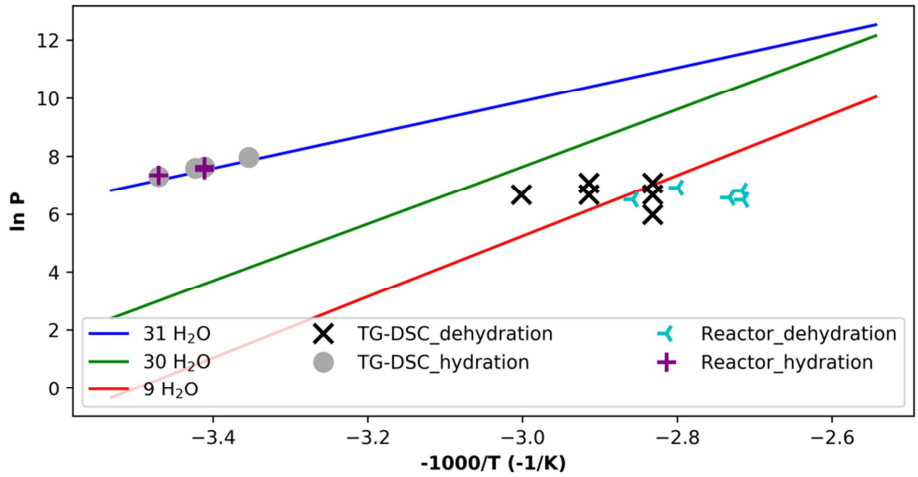

Figure V-3: Location of operating points in the de/hydration equilibrium curves of ettringite relating to Chapter III.

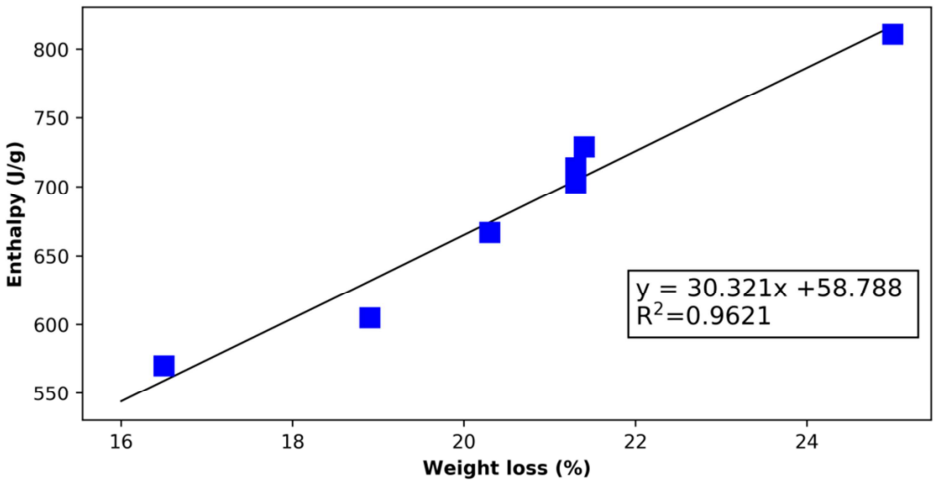

Figure V-4: Dehydration enthalpy as a function of the weight loss in TGA-DSC.

5.2.2.2 Hydration analysis

The dehydrated specimen was prepared at 80 °C under dry N_2 flow in TGA-DSC. The hydration experiments were then carried out at about 90 % RH and for different temperatures. Figure V-5 shows the DA and heat-releasing power for hydration at 20 °C at 2100 Pa (~ 90 % RH). The peaks observed on the heat flow curve allow separating the whole process into three stages. The first strong heat releasing process before 0.4 hours is with a DA of about 0.15. This step is probably due to a surface reaction that leads to a high reaction rate corresponding to a large slope given by the blue curve. Afterward, from 0.4 to 2.1 hours, the rate of water vapor sorption slows down and stabilizes. It leads to a nearly linear growth which is probably due to a steady diffusion of water vapor in the material grains. During this period, the discharging power gets firstly a slight rise to 0.18 mW and then decreases to 0.03 mW. The slow tendency of DA evolution in the last stage shows a quite slow water vapor sorption process.

The heat-releasing power of this development is too small to be detected and the accuracy of signal is somehow influenced (waveform) between 3 to 17 hours. Therefore, the main accountable amount of heat is released during the first two stages. The amount of water uptake in the sample is about 78 % of water removal weight during the preparation of the dehydrated sample.

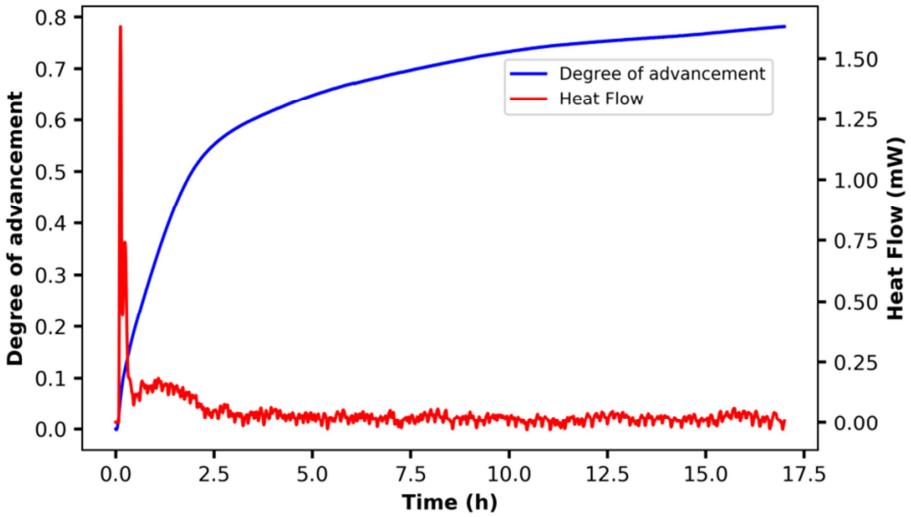

Figure V-5: Hydration kinetics of C80P20 powder sample at 20 °C & 2100 Pa.

Figure V-6 shows the hydration curves of DA under the operating conditions given in Table V-4. The three stages in the hydration at 20 °C are also observed in the other hydration experiments at 90 % RH. These stages could be distinguished by the DA: the first rapid sorption locates at 0–0.15, while the steady zone at 0.15–0. 55 and the final slow process at DA > 0.55. In Table V-4, the hydration enthalpies at 15 and 20 °C are around 635 J/g of initial hydrated material with a DA of about 0.78. The enthalpy at 19 °C is slightly higher while the heat-releasing amount at 25 °C is significantly higher. It is owing to the higher sorption rate and amount of water vapor. Combining with Figure V-3, the end chemical state is the same at 31-hydrate ettringite and the final different DA comes from the state of hydration. The higher added PWVP the faster the hydration. These final hydration enthalpies are assumed to be equal to the heat amount for removing water if the DA can reach 1. It should be noticed that the releasing heat is composed of the condensation heat of capillary water and major chemical heat from ettringite hydration.

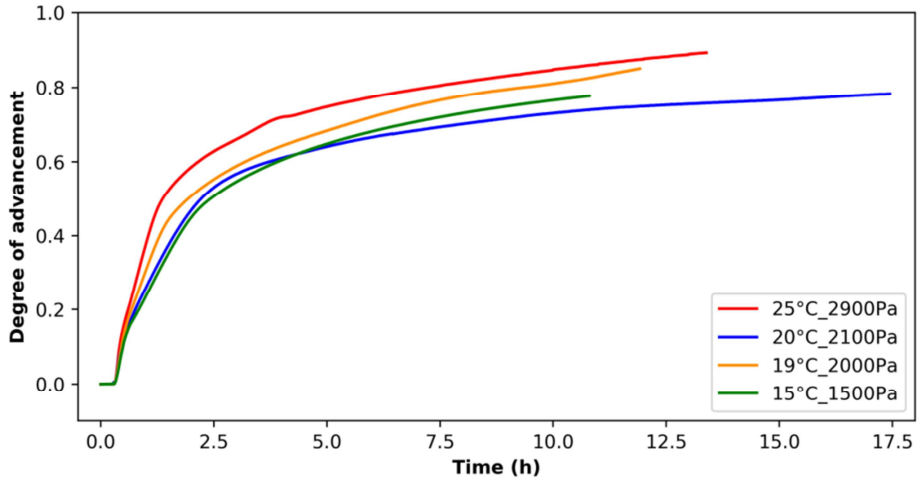

Figure V-6: Hydration under 90 % RH at various temperatures and PWVPs for powder samples dehydrated at 80 °C in dry N_2.

Table V-4: Hydration results for C80P20 powders dehydrated at 80 °C & in dry N_2.

Hydration temperature (°C)	PWVP (Pa)	RH (%)	Enthalpy (J/g $_{\text{initial hydrated material}}$) *
25	2900	91	755
20	2100	90	636
19	2000	91	652
15	1500	88	631

*The enthalpy is integrated by the baseline of 0 for the whole process even though the "Heat Flow" signal is said imprecise in the third stage of hydration.

5.2.3 Reactor performance

5.2.3.1 Dehydration tests

The water removal process was started after the stabilization of dehydration conditions for the airflow (details are given in section 2.4). Figure V-7 presents the dehydration experiment carried out for 95.2 °C and 6.1 m^3/h (0.94 m/s). During the charging phase, the temperatures in the fixed bed gradually increased over time and were identical after 1 hour of heating. As being a porous material, the removable water in the grains is composed by water pore solution (physical desorption) and structural water in ettringite (chemical desorption).

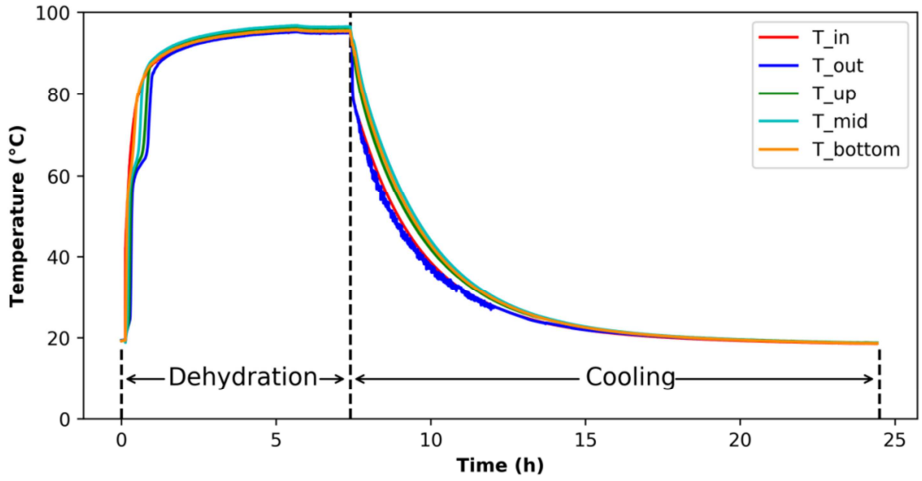

Figure V-7: The temperature evolution of thermocouples in the reactor during dehydration (95.2 °C & 6.1 m^3/h) and cooling (no air supply).

The process of dehydration during the first 3 hours is specified in Figure V-8. Once the hot airflow introduced into the reactor, the bottom temperature increases steeply to 53.8 °C with a very strong release of water vapor up to about 2100 Pa. This quick growth of PWVP mainly comes from the evaporation of the pore solution in the materials. Later, the PWVP increases significantly to 2750 Pa until the temperature of the upper-position raises to 54.9 °C. Meanwhile, the temperature of the bottom material starts to rise again. The PWVP then falls to around 1400 Pa when the temperature of the whole fixed-bed climbs higher than 61.3 °C. Then, the pressure slightly increases to 1500 Pa and keep at almost the same level when the materials at the upper-position are heated. In this stage, the produced water vapor is supposed to be essentially coming from the main dehydration of ettringite. Hereafter, the upper temperature reaches 88.3 °C as the bottom and middle temperature of the fixed-bed. The PWVP's decrease is delayed because some materials still need to be dehydrated at the top of the fixed-bed. These phenomena during heat storage are consistent with the three dehydration phases described by Pan and Zhao [5]. Besides, the studied operating conditions prove the possibility of using hot air from common solar air collectors to dehydrate ettringite materials in residential buildings.

It is worth noting that, at the second large increase of temperatures from 65.2 to 88.3 °C, the dehydration of ettringite is still occurring since a relatively high PWVP. However due to a more difficult process to remove the water molecules in the ettringite crystal structure than evaporation of pore solution, the slope of the curve is, at this stage, smaller than the one at the first increase of temperature from 27.2 to 54.9 °C. When the temperatures of the whole fixed-bed approaches 90 °C, the last stage of dehydration is almost finished and the PWVP decreas-

es significantly and forms a tail-off to finally stabilize at 600 Pa. These phenomena are similarly findable in the dehydration at different temperatures and airflow rates. The materials in the fixed-bed are completely charged by hot airflow when the PWVP at the outlet of the system is stable at the temperature of 95.2 °C.

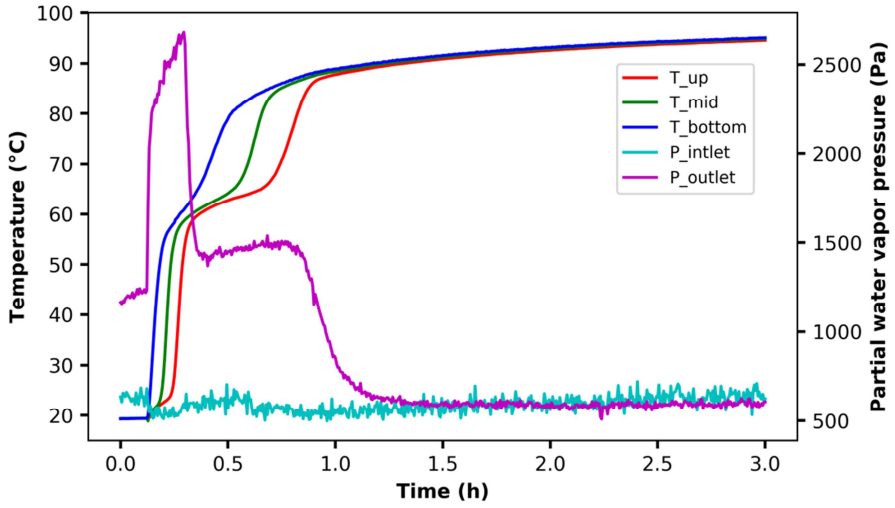

Figure V-8: The evolution of reactor temperatures and partial water vapor pressure at outlet of system during first hours of dehydration (95.2 °C & 6.1 m^3/h).

Figure V-9 represents the variation of the difference between the temperatures of the entry and exit of the fixed-bed during the charging stage. The T_{in} raises very rapidly first of all while only a slight increase for the T_{out}. It results in the maximal temperature difference of 39.3 °C for the first stage. Then difference decreases down to 14.7 °C due to the increase of T_{out}. During this period, the temperature of the fixed bed ranged between 54.9–65.2 °C. Afterward, the temperature difference increases to 20.9 °C for the second stage, with duration approximately equal to three times the first stage one. Once the main dehydration of material is done, the airflow temperature at the outlet of reactor increases significantly, which leads to the second drop of temperature difference. However, the reactor is not totally adiabatic despite the use of thick glass wool insulation (~ 5 cm). The final temperature gap is about 0.6 °C between the two thermocouples (14.5 cm), which results in the heat loss power of 1.36 W according to Equation V-6. The temperature difference ΔT between the two positions is equivalent to a specific power loss of 0.018 W/g of sample.

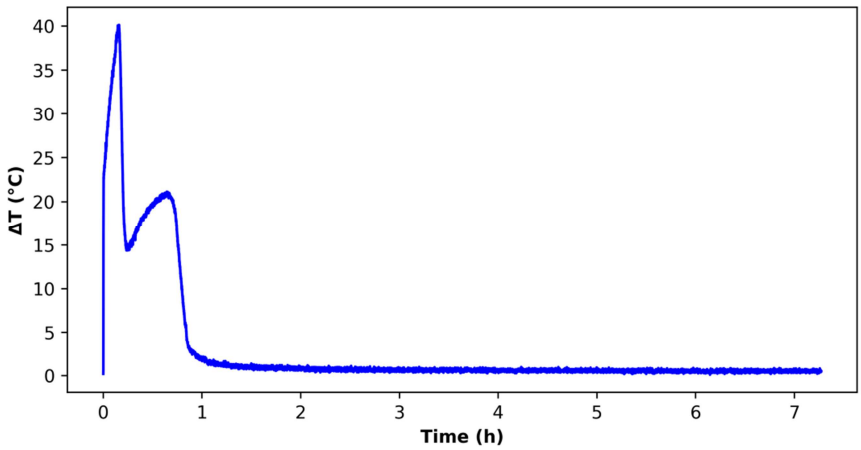

Figure V-9: The difference of temperatures at up and bottom position of fixed-bed sample during dehydration.

Table V-5 summarizes the results of dehydration experiments. Despite of the small variation of loss percent for dehydration at 95 °C, the average value is about 33.5 %. The small divergence may come from the different weight of samples loaded, which leads to some effect on bulk porosity and furtherly influences the dehydration procedure. Besides for similar sample mass, the lower the dehydration temperature the smaller the weight loss is. The weight losses in the reactor are indeed bigger than in the TGA-DSC analysis because of more pore solution in the non-silica gel dried reactor samples.

After the dehydration at 95 °C, the material is cooled down to ambient temperature with thermal insulation to simulate the temperature evolution in a real operating scenario, see in Figure V-7. It takes about 10 hours to discharge the sensible heat. Even though the temperatures of the materials decrease to ambient temperature (18.9 °C), the chemical energy is stored thanks to the dry condition in the reactor to avoid water re-adsorption.

Table V-5: Experimental results for dehydration.*

Final temperature (°C) at the reactor inlet	Flow (m^3/h)	Weight of samples (g)	Weight after dehydration (g)	Percent of loss (wt.%)
95.0 ± 0.1 (95)	7.5	74.80	49.75	33.5
95.2 ± 0.2 (95)	6.1	77.30	52.25	32.4
92.8 ± 0.2 (95)	5.1	70.25	45.90	34.7
84.1 ± 0.1 (85)	5.1	74.85	50.30	32.5
76.8 ± 0.2 (75)	5.1	79.45	54.30	31.7

*The number in the brackets is the targeted temperature of dehydration in the reactor. The incertitude of flowrate is ± 0.1 m^3/h while ± 0.05 g for weight.

5.2.3.2 Hydration tests

After the stabilization of the humid airflow psychrometric values, 20.0 °C & 90.0 % RH, the three-way valve was turned on to introduced the humid airflow into the reactor and then hydrate the material. Then, the water vapor diffused into the porosity of the material and get absorbed to release thermal energy and increase the temperature of the fixed-bed. Meanwhile, the airflow entering the reactor advected the heat produced. In this way, the stored chemical energy was transferred into the airflow in order to heat the household.

The inlet relative humidity at 20.1 °C is pre-stabilized at 90.1 % RH (see Table V-6). Along with to Equation V-2 to Equation V-4, the PWVP is set to 2280 ± 60 Pa during the hydration phase (showed in Figure V-10 a). During the hydration, the outlet PWVP decreases to 270 Pa due to very strong sorption of water vapor at the surface of materials. In the meantime, the material presents a very sharp increase in temperature above the constant inlet airflow temperature of 21.9 °C. In Figure V-10 b, the bottom temperature increase is about 12.8 °C while the middle temperature and top temperature reach, respectively, 26.8 °C and 34.1 °C. This gradual evolution in different locations is the result of heat advection from the material located at the lower position in the reactor. It also leads to a time shifting of the peak visible in Figure V-10 c, which shows a zoom of the first 30 minutes. Moreover, the maximal temperature of the airflow leaving the reactor is 57.5 °C with an increase of 37.5 °C. Similarly showed in Figure V-11 for the same period, the rate of water vapor sorption is as high as 71.4 g/h by the fixed-bed, which leads to a steep rise in the quantity of water vapor absorbed.

Afterward, the PWVP at the outlet of the system increases rapidly (Figure V-10 a), which corresponds to a sharp decrease in the rate of sorption. Consequently, the temperatures in the fixed-bed decrease in the following order: bottom, middle and finally up-side. The temperature of the airflow leaving the reactor decreased to 30.3 °C. Then all the temperatures decreases slowly when the water sorption rate reduces. This tail-off may be due to the low diffusion rate of water vapor in the material granules thereby the low quantity of available water resources for exothermic reaction under the operating conditions. Figure V-10 b shows that the thermal energy release lasted about 2.5 hours and the water sorption rate is close to 0. However, the slight increase of water vapor absorbed could be observed but not visible in temperature during the last hour of the experiment in Figure V-10 b. The profile of temperature curves and water adsorption rate could be modified, not only by improving the porosity

and thermal conductivity of material itself [6], but also by low airflow rate or adding more materials to extend the duration of the temperature peaks.

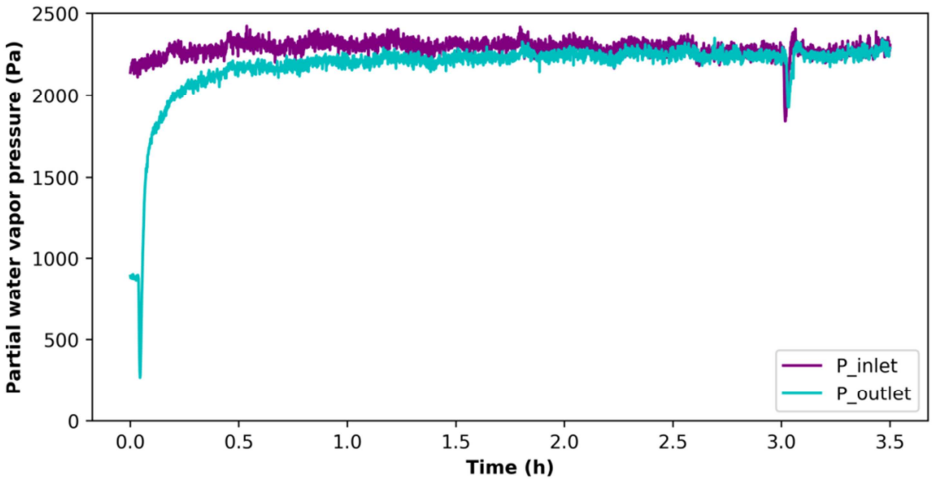

(a) PWVP evolution

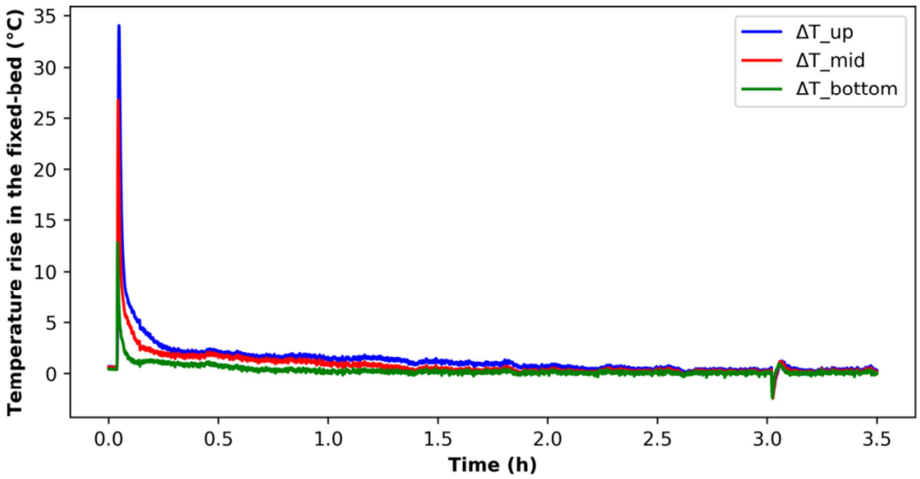

(b) The increase of temperatures in the fixed-bed

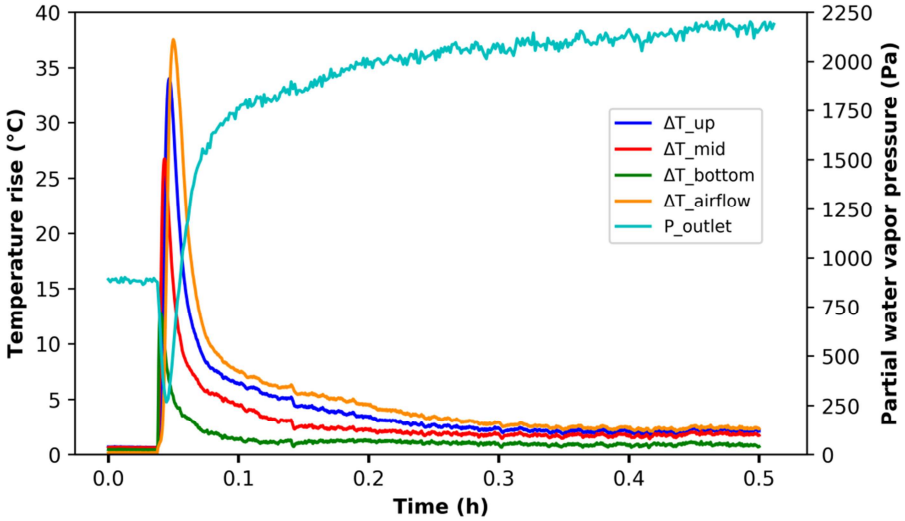

(c) Results for the first 30 minutes

Figure V-10: Hydration performance at 90.1 % RH and 20.1 °C in the reactor.

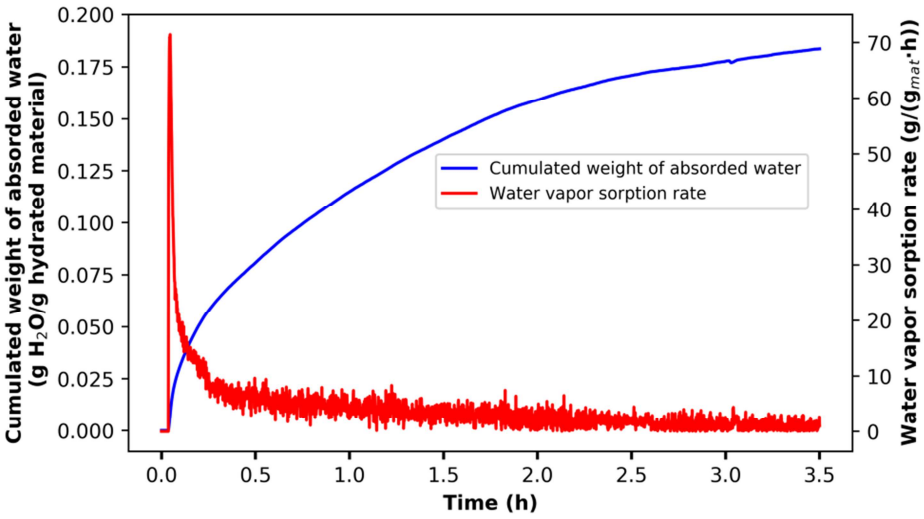

Figure V-11: Kinetics of water sorption during hydration at 20.1 °C and 90.1 % RH.

As a porous material, a certain amount of water vapor could condense in the pores. Therefore, the heat released could be owed to the chemical reaction and physical adsorption. However, it is difficult to discuss the two processes dividedly. The exothermic power and accumulated energy were calculated from the temperature rise of airflow at the exit of the reactor by Equation V-6 and Equation V-7. The mass-normalized power of discharging was determined as the ratio of heat-liberating power to the weight of initial hydrated cement materials loaded in the reactor. Figure V-12 shows the evolution of the specific power during the hydration. The whole profile of the curve is similar to the temperature ones. The response of the system to release heat is very rapid and rockets as high as 915 W/kg hydrated material, which may come from the large water molecular bonding capacity of meta-ettringite (see Chapter III). Then it reduces quickly and forms a long tail-off to 0 after 2.5 hours. The total energy in this experiment contributes to about 176 kWh/m^3 hydrated cement material, or a reactor energy density of 104 kWh/m^3. Note that the experiment is stopped after 3.5 hours due to the negligible evolution of the airflow temperature. Although the power is close to 0, the heat releasing is always in process due to the slow kinetic of water absorption. With time, the final mass should be equal, or at least, close to the initial weight.

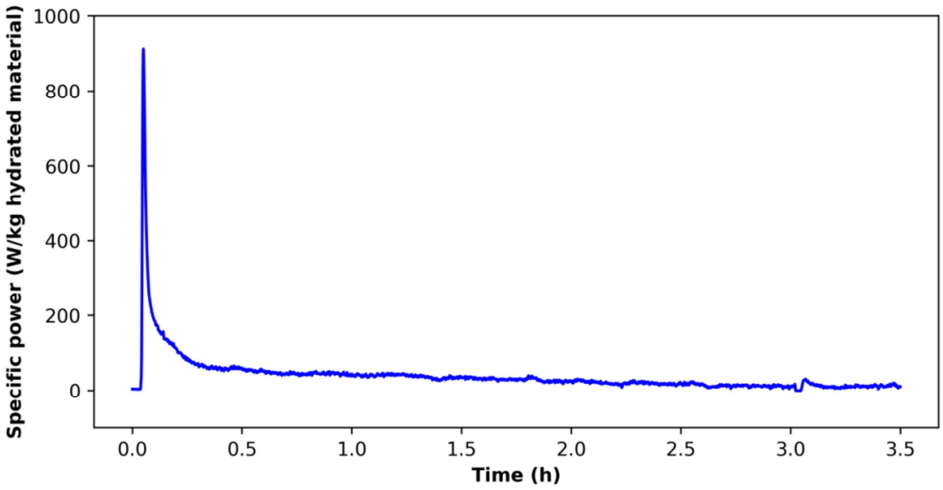

Figure V-12: The hydration power of material calculated by the temperature rise of airflow exiting the reactor.

Table V-6 summarizes the results of hydration experiments for different scenarios. The best result obtained is with the operating conditions of 20.1 °C, 5.1 m^3/h and 90.1 % RH. The reduced airflow rate could increase the temperature but decreases the maximal power due to less accessible water resources for the same period. The energy density is expected to be similar to the one with a higher airflow rate. However, the low airflow rate makes the kinetic of hydration very slow, which leads to the earlier ending of the experiment. If the relative humidity decreases by 10 %, the amount of water absorbed is as low as 5.8 %. Besides, a lower hydration temperature may also slow down the kinetics of water vapor sorption, thereby a relatively lower temperature and power. All water uptake percentages are smaller than the weight loss percentages during dehydration because of the slow sorption kinetics of granules.

Table V-6: Results of hydration experiments under different operating conditions.*

Hydration temperature (°C)	Flow (m^3/h)	RH (%)	Weight of dehydrated samples (g)	Percent of water gain on initial hydrated sample) (%)	T _out max. (°C)	Specific max. power (W/kg $_{\text{initial hydrated sample}}$)	Material energy density & reactor energy density (kWh/m^3)
20.1 ± 0.2 (20)	5.1	90.1 ± 1	49.75	14.0	57.5	915	176 & 104
19.8 ± 0.2 (20)	3.1	90.2 ±1.4	53.5	10.3	59.2	630	148 & 87
20.3 ± 0.3 (20)	5.1	80.4 ±1.4	57	5.8	47.1	670	94 & 56
14.7 ± 0.2 (15)	5.1	92.7±1.2	52.25	12.9	49.1	750	175 & 103

*The number in the brackets is the targeted temperature of hydration in the reactor. The incertitude of flowrate is ± 0.1 m^3/h while ± 0.05 g for weight.

5.2.4 Comparison with other systems from the literature

Compared with energy storage materials issued from different authors, in Figure V-13, the current ettringite-based material has comparable material energy storage density (excepting pure salt hydrates). However, the average releasing power of 33.3 W/kg is much higher than the other energy storage materials. It is clear, from Table V-7, that the maximum release power of 915 W/kg is much higher than the other materials from the literature! The specific material cost of the ettringite based material is only 3.5 €/kWh$_{exp}$ in the reactor tested, which is 19 times less than SrBr2 and 4 times less than zeolite 13X. It is still very possible to decrease this specific cost by increasing its energetic performance, with the consideration that the upper limit is 286 kWh/m^3 for the hydration at 20 °C & 2100 Pa in TGA-DSC analysis. This low material cost promises a future large-scale application for thermal energy storage in buildings.

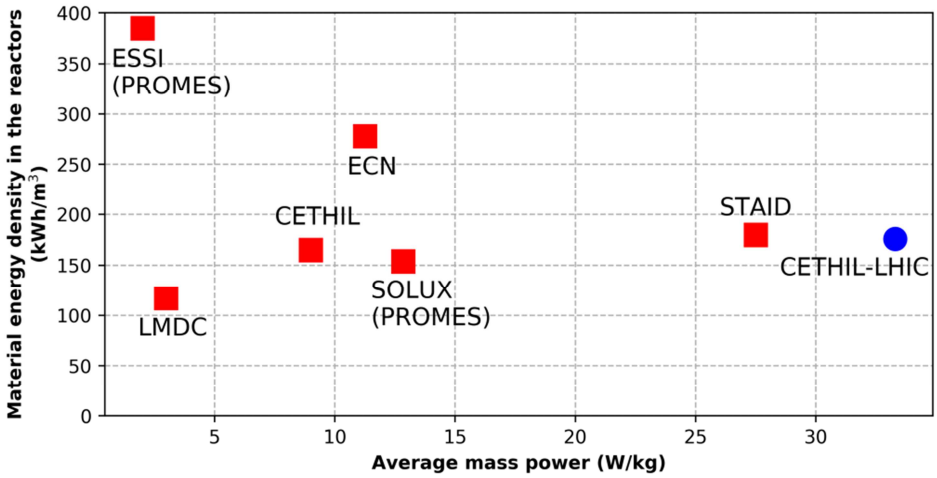

Figure V-13: Comparison of thermal performances for various materials: ESSI ($SrBr_2/H_2O$, [7]), LMDC (Ettringite_CSA/H_2O, [6]), CETHIL ($MgSO_4$+Zeolithe13X / H_2O, [8]), ECN ($MgCl_2/H_2O$, [9]), SOLUX ($SrBr_2/H_2O$, [10]), STAID (Zeolite 13X/H_2O, [1]), and CETHIL-LHIC (Ettringite_C80P20/H_2O, in this work).

Table V-7: Comparison of several most investigated absorbent energy storage materials in reactors.

Investigations	Specific material cost (€/kWh$_{exp}$)	Maximal mass power (W/kg)	References
$SrBr_2/H_2O$	67 [1]	2.3	ESSI [7]
Zeolite 13X/H_2O	15.2	32.5	STAID [1]
Zeolite-$MgSO_4$	33.4 [2]	29.5	CETHIL [8]
Ettringite_C80P20/H_2O	3.5	915	CETHIL-LHIC (current work)

[1] calculation based on [11].

[2] the material cost of $MgSO_4$ is supposed to be 30 €/kg.

5.3 Conclusions

The present work aims at investigating the thermal performance of an ettringite-based material, not only at micro-scale, but also at the reactor scale in an open-mode fixed-bed prototype. After the drying by silica gel, the dehydration enthalpy of material at 80 °C under dry N_2 was 811 J/g $_{\text{initial hydrated materials}}$ with 25 % weight loss for 4 hours, which equals to 286 kWh/m^3 $_{\text{initial hydrated material}}$. The hydration enthalpy obtained was 755 J/g $_{\text{initial hydrated materials}}$, which is indeed smaller than that of dehydration. This is probably due to the slow kinetics of last hydration stage with imprecise heat signal in TGA-DSC. However, the heat releasing should still take place in this stage even the slow sorption of water vapor, which may not be counted.

The open-mode reactor tests involved several operating conditions for the charging and discharging process. The three parameters respectively studied were three temperatures and two airflow rates for dehydration while two temperatures, two airflow rates, and two RHs for hydration. The main results for these prototypes experiments are:

- ✓ The energy charging could be completed within several hours in the improved prototype with hot airflow having working temperatures that can definitely be supplied by a solar air collector system.
- ✓ The dehydration temperature has a minor influence on the final mass loss due to a relatively dry ambient air supplied. Moreover, the weight loss in the reactor is higher than that in the micro-scale study because of bigger pore solution content. A part of this solution may be regained during hydration if time is given to release physical water sorption energy.
- ✓ The RH is a quite important parameter to hydrate absorbent material. The higher the relative humidity during the discharging process, the more the released energy and power.
- ✓ The decrease in airflow rate leads to a reduction of the maximum releasing power but makes the maximal hydration temperature increased.
- ✓ In this study, the mass power has reached 915 W/kg which is higher than that most energy storage systems. Moreover, there exists no delay for the response of heat-releasing in this system. The maximal hydration temperature was 57.5 °C. The materi-

al energy density is about 176 kWh/m^3 while a prototype energy density of 104 kWh/m^3 for the fixed bed.

The present results are promising in using this kind of low-cost energy storage material for short-period or seasonal thermal energy storage. However, the material is still need to be developed to improve the hydration kinetics by increasing its porosity or ettringite content. Furthermore, large-scale prototypes are necessary before the integration into building.

5.4 References

[1] Johannes K et al. Design and characterisation of a high powered energy dense zeolite thermal energy storage system for buildings. Appl Energy 2015;159:80–6.

[2] J.A., Goff; S. G. Low-temperature properties of water from -160 to 212 °F. Trans Am Soc Heat Vent Eng 1946;52:95–121.

[3] Okhrimenko L et al. Thermodynamic study of $MgSO_4$–H_2O system dehydration at low pressure in view of heat storage. Thermochim Acta 2017;656:135–43.

[4] Kuznik F, & Johannes K. Thermodynamic efficiency of water vapor/solid chemical sorption heat storage for buildings: Theoretical limits and integration considerations. Appl Sci 2020;10.

[5] Pan ZH, & Zhao CY. Gas–solid thermochemical heat storage reactors for high-temperature applications. Energy 2017;130:155–73.

[6] Ndiaye K et al. Experimental evaluation of two low temperature energy storage prototypes based on innovative cementitious material. Appl Energy 2018;217:47–55.

[7] Michel B et al. Experimental investigation of an innovative thermochemical process operating with a hydrate salt and moist air for thermal storage of solar energy: Global performance. Appl Energy 2014;129:177–86.

[8] Hongois S et al. Development and characterisation of a new $MgSO_4$-zeolite composite for long-term thermal energy storage. Sol Energy Mater Sol Cells 2011;95:1831–7.

[9] Zondag H et al. Prototype thermochemical heat storage with open reactor system. Appl Energy 2013;109:360–5.

[10] Mauran S et al. Solar heating and cooling by a thermochemical process. First experiments of a prototype storing 60kWh by a solid/gas reaction. Sol Energy 2008;82:623–36.

[11] N'Tsoukpoe KE et al. The concept of cascade thermochemical storage based on multimaterial system for household applications. Energy Build 2016;129:138–49.

Chapter VI. General conclusion and prospects

The research works on the near-/long-term storage of excess solar energy, by a thermochemical process, are indispensable for rationalizing the management of residential heating consumption. This kind of solution is particularly promising because it allows a big amount of energy stored in the form of chemical potential without thermal losses over time. In this context, the objective of this thesis work was to demonstrate the feasibility of ettringite-based materials for thermal energy storage and analyze the operation of an adapted thermochemical reactor prototype.

Ettringite mineral, existing in hydrated cement, which can be produced in large quantity around the world, is low-cost, zero-toxic, non-flammable, and in high energy density. Such kinds of materials are currently considered as a more suitable material solution to store excessive heat for later use, compared to the most literature promising hygroscopic salts in the literature, such as $MgSO_4$, $SrBr_2$, and $LaCl_3$. Moreover, a porous ettringite-based material produced from commercial cements is a simple-craft composite material by hydrating cement without additional host carriers to avoid particle agglomeration, which is a big advantage at the level of manufacture. Therefore, this thesis project about studying ettringite and ettringite based-materials is significant to reveal their thermal behaviors and advance heat storage technologies.

6.1 Mains results obtained

The extractions of the main achievements of the previous chapters of this thesis are presented below:

- ✓ By the thermal characterizations of the synthetic ettringite powder, particularly via TGA-DSC, the kinetics and thermodynamics of de/hydration have been studied for discharging and charging thermal energy. The conversion between ettringite and meta-ettringite is strongly dependent on the temperature and partial water vapor pressure.

  In the kinetic study, the dehydration mechanism of ettringite, by analyzing the variation in the heat flow of reaction, has experimentally proved the conjecture for **a stepwise dehydration relating to its crystal structure in the literature**. Moreover, the enthalpy of the process is a monotonic function of the loss in the water molecule number. As the reversible process of removing water molecules, the over-hydration in different degrees exists commonly under high relative humidity (RH, > 76 %) without excluding the adsorption at the mineral surface. Unlike salt hydrates, this over-

hydration of ettringite does not form a concentrated solution thanks to being insoluble in water. **The hydration enthalpy refers to an energy storage capacity of 547 kWh/m^3 under the operating condition (20 °C and 90 % RH)** not including the condensation heat by over-sorption.

An experimentally derived model of thermodynamics explains the impact of water activity on the stability of ettringite / meta-ettringite as a function of temperature. This model can estimate the hydration state and stability limits of hydrates under a given condition, which can forecast the quantity of accessible chemical energy in the materials. Being consistent with the literature, the hysteresis is equally observed between dehydration and hydration.

- ✓ In regard to the industrial production and the technical problem of powder agglomeration during hydration, ettringite composite materials are recommended for thermal energy storage except for their potential carbonation issue (as for all the types of cement-based materials).

  Therefore, this thesis presents the development of three novel porous ettringite-enriched materials and their corresponding meta-ettringite based materials (partially dehydrated) based on commercial cements, as well as their investigation of carbonation durability under different relative humidity with respect to thermal energy-releasing scenarios. The natural and accelerated carbonation of ettringite and meta-ettringite-based materials shows an essential effect by the relative humidity regardless of the grain size (1–4 mm). Among the three ettringite-based materials, the one containing the highest amount of ettringite (~ 75 wt.%), shows the highest carbonation resistance. Under the "standard" conditions of RH and temperature for the material storage (20 °C & 50 % RH), the carbonation rate is very low (even under an atmosphere containing 1 vol.% CO_2). However, when the RH level increases to 90 %, both the carbonation rate and carbonation degree raise, thereby leading to a more significant depletion of ettringite in case of accelerated carbonation (under 1 vol.% CO_2). Specifically for meta-ettringite based materials, high RH hydrates firstly the meta-ettringite to a higher hydrate then it is destroyed to small molecules, such as $CaCO_3$ polymorphs (vaterite and aragonite), $CaSO_4$ hydrates (hemihydrate for 70 % RH and gypsum for 90 % RH), amorphous $Al(OH)_3$ and water. In the natural environment (20 °C & 50 %

RH), after exposure of 6 months, the hydrated and dehydrated materials are only carbonated to approximately 6 %, which designates that this material is very storable.

A special series of experiments are carried out so as to study the effect of carbonation on the thermal energy storage capacity. At its initial stages (up to the CO_2 binding quantity of 0.075), carbonation has relatively little influence on the energy storage capacity, which stabilizes at 890 J per gram of anhydrous mixture. However, after a certain time of carbonation (up to the CO_2 binding quantity of 0.23), the decrease of the energy storage capacity becomes more significant (with a reduction to 320 J/g of anhydrous mixture), in accordance with the depletion of ettringite.

- ✓ After being proved carbonation resistant, the same composite material requires to be analyzed in TGA-DSC for de/hydration kinetics as well as reactor tests in macroscale.

Same as pure ettringite samples, the conversion between ettringite and meta-ettringite in the composite material is under the effect of the temperature and partial water vapor pressure. The enthalpy of reaction is a function of the weight loss of material during dehydration and presents an energy storage capacity of 286 kWh/m^3. The hydration process of the composite material takes a long time and arrives at a lower degree of advancement compared to the hydration kinetics of pure ettringite under the same conditions.

In the fixed bed reactor tests, the granules made of the composite material containing ettringite (about 71 wt.% just before the tests) can be fully charged in several hours by airflow at temperatures corresponding to the heat resource from the solar collectors. The main dehydration stage occurs at the temperature range 55–65 °C. In addition, a higher temperature can cause a bigger weight loss. During the cooling phase, the sensible heat is lost but chemical potential can be released during hydration. To experiment with a real-world scenario of discharging heat at 20 °C, the **instantaneous response**, the **maximal temperature of 57 °C** and a preliminary **material energy-releasing density of 176 kWh/m^3 declare its good energetic performance. The maximal releasing power can be 915 W/kg** which is several tens, even hundreds, higher than other materials in different thermal energy projects. This heat discharging ability may easily satisfy the high demand for thermal power in the building during the peak energy consumption period.

6.2 Prospects

During this thesis work, we have established that ettringite-based materials, until recently, are an interesting and promising research field for being used as thermal energy storage material. Although the current work has laid a good foundation, several points still need to be assessed for the future development of such kind energy-storage technologies using ettringite.

6.2.1 Understanding of thermal behaviors

The reaction system between ettringite / meta-ettringite and water vapor is now better described relating to the thermal energy storage conditions, in terms of the reaction mechanisms, kinetics, and thermodynamics of hydration and dehydration process.

Nevertheless, it would be necessary to investigate the thermodynamics more widely in the temperature range for the hydration reaction, in order to minimize the effect of fluctuation of experimental results on the accuracy of experimental thermodynamic models.

The cyclability in terms of charging / discharging for pure ettringite has been studied in the literature via dehydration at low-temperature (40 °C). In view of this result, it is not suitable for the thermal energy storage concepts in combination with solar air collectors, urban heating network or industry waste heat. Therefore, it is significant to carry out a specific study on the cyclability of ettringite under application conditions.

Furthermore, the hysteretic behavior, existing in thermodynamics between the dehydration and hydration of ettringite, may be related to the variation of reaction mechanism (mono-variant and bi-variant) which lead to the change of free energy barrier to overcome for desorption and sorption, but not have been proved. The literature explanation of the meta-stability of some hydration states seems to be less possible since all the thermodynamic equilibriums of meta-stable phases gather without any overlapping area between hydration and dehydration in this study (see appendix A-2). A systematic work is then required to evaluate the hysteretic behavior for a comparison between different materials.

6.2.2 Optimization of the composite material containing ettringite

Ettringite composite particles from cement are promising candidates without supplementary investment in the fabrication of matrix material. Aiming at improving the thermal performance of this kind of material, the optimization of certain natures is still necessary. The mix-

ture fractions for the types of cement could be optimized to find a balance between higher ettringite content and durability/cyclability of the composite material.

The high water-solid ratio used to hydrate cement results in a high porosity but also reduces the mass density of the material which leads to a relative small volume energy storage capacity. In future development, a high permeability is preferred to ensure the mass transfer of water vapor. In the meantime, the pore volume and size needs to be controlled in order to obtain a smaller but more interconnected porosity. This enhancement can increase the efficient volume of material thereby enlarging the material energy density.

Obviously, this improvement may also change the carbonation kinetics. Therefore, a carbonation durability study is always recommended if the material is going to be used in ambient airflow. Besides, the addition of other hydrates, like calcium silicate hydrates, portlandite ($Ca(OH)_2$), could protect ettringite from carbonation depletion. Alternatively, regular replacement of material is necessary, which leads to caring about the coordination between economy and systemic integration problems. On the other hand, a foreign ion substituted ettringite, of which carbonation resistance is enhanced, may also be an interesting solution to this problem.

6.2.3 Reactor experiments

In this thesis work, the inspiring results are obtained with a small volume of material, which is far away from an application-scale prototype. The amount of material used for a single household in near-term single needs several tens of kilograms and several cubic meters to meet the demand of heating and domestic hot water for long-term heat storage. Therefore, prototypes in larger scales need to be designed and experimented in order to validate the use of ettringite-based materials for real-world use. As for the carbonation issue of materials in the prototypes, closed systems that work with a closed working fluid circuit can avoid the impact of CO_2 from the atmosphere. However, a high system cost is required for solving the derivative problems, like lower working pressures, system tightness, the efficiency of heat exchangers, etc. The parameter of compactness of the fixed bed has also to be studied because it affects the mass and heat transfer during dehydration / hydration cycles. To release the stored chemical potential, high-levels of RH is obligatory, which raises the issue of producing water vapor at low cost and energy requirements. Therefore, the development of a numerical model for a porous fixed bed, validated by the experimental results, would be relevant to pre-

dict the thermal behavior of the TESC system under different operating conditions. In addition, a thermo-economic study is recommended to apply a thermal energy storage system in the different energy consumption scenarios of buildings.

Appendix

A-1 Description of the Thermogravimetry-Calorimetry (TGA-DSC) coupling

The Sensys Evo TG-DSC device from Setaram is presented in Figure A-1 a. It is absolutely symmetrical for the system of TG (thermobalance) and DSC sensors. It can simultaneously measure the change in mass and heat flow over time. The crucibles in quartz (Figure A-1 b), of which the bottom is a neutral porous matrix allowing passing carrier gas flow, are placed in the furnace at the level of the Calvet 3D sensor (Figure A-1 a). Thanks to the symmetry design, the buoyancy effect is compensated automatically during heating the sample. The variation in the mass of the sample is measured by the electrical balance placed in the head of the device, which is under helium protection to avoid the entry of corrosive gas to the device. The carrier gas, composed entirely of N_2 (50 mL/min) and the desired quantity of water vapor, is introduced into the furnace from the bottom. The water vapor pressure is set by using a Setaram Wetsys steam generator.

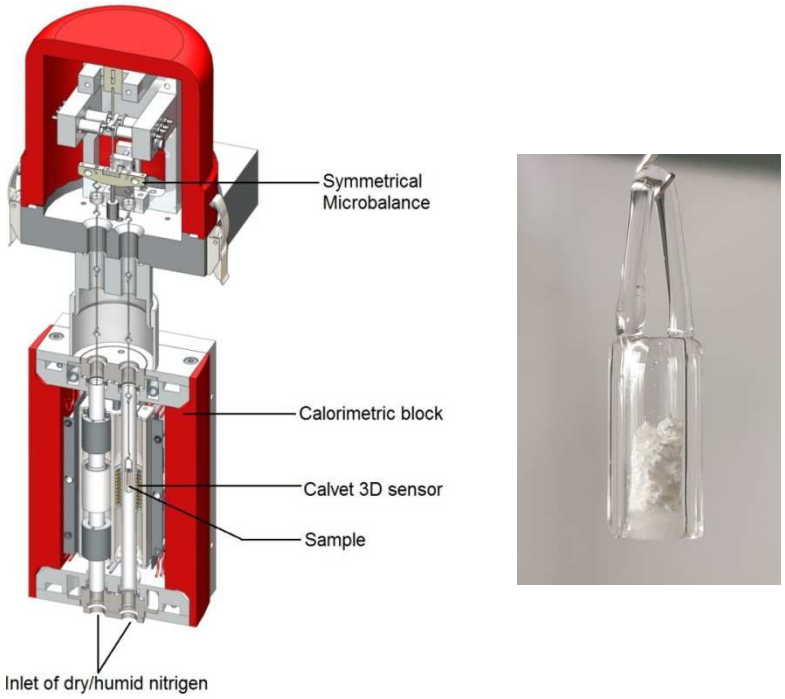

(a) Schematic of TG-DSC (b) Photo of quartz crucibles

Figure A-1: Setaram Sensys Evo TG-DSC thermobalance equipment.

A-2 Thermodynamics of de/hydration of ettringite

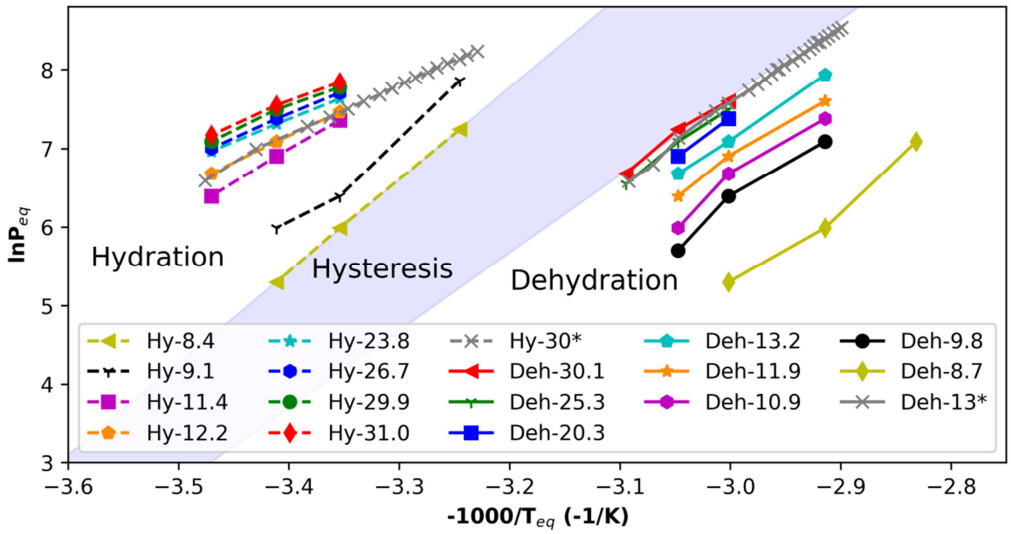

*Figure A-2: Thermodynamic equilibrium of ettringite dehydration, in which * is the reversible process of Met13 ↔ Ett30 adapted from [1].*

A-3 The theoretical CO_2 binding capacity of common cement phases

Table A-1: CO_2 binding capacity of certain cement phases [2].

	Molar mass (g/mol)	CO_2 binding capacity (mole CO_2 /mole phase)	CO_2 binding capacity (g CO_2 /100g phase)
C	56.1	1	78.5
N	62.0	1	71.0
CH	74.1	1	59.4
C_3S	228.3	3	57.8
C_2S	172.2	2	51.1
C_3A	270.2	3	48.9
CA	158.0	1	27.8
CA_2	260.0	1	16.9
$C_{12}A_7$	1386.7	12	38.1
$C_4A_3\bar{S}$	610.3	3	21.6
C_4AF	486.0	4	36.2
K	94.2	1	46.7
$C_9S_3\bar{S}_3{\cdot}CaF_2$	1003.2	6	26.3
$C\bar{S}H_2$	172.2	0	0
$C\bar{S}H_{0.5}$	145.1	0	0
$C\bar{S}$	136.1	0	0
CC	100.1	0	0
Insert	/	0	0

Insert: M, CT, C_7MS_4, C_3MS_2, C_2AS, and NA_{11} treated as inert to carbonation.

A-4 Granulometry photos of granule samples

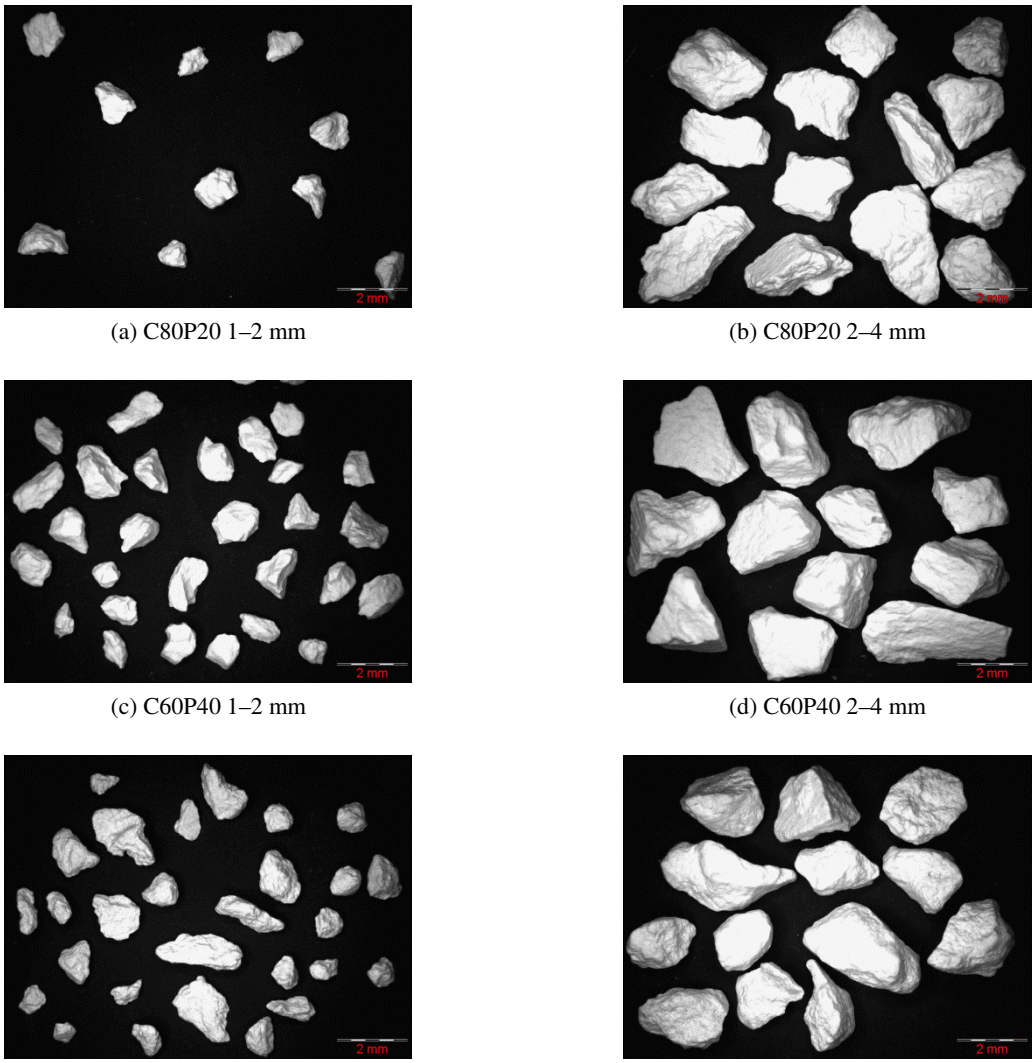

(a) C80P20 1–2 mm (b) C80P20 2–4 mm

(c) C60P40 1–2 mm (d) C60P40 2–4 mm

BCSAF 1–2 mm BCSAF 2–4 mm

Figure A-3: Granulometry analysis of three hydrated binders' granules in Chapter 4

A-5 SEM photos of ettringite / meta-ettringite

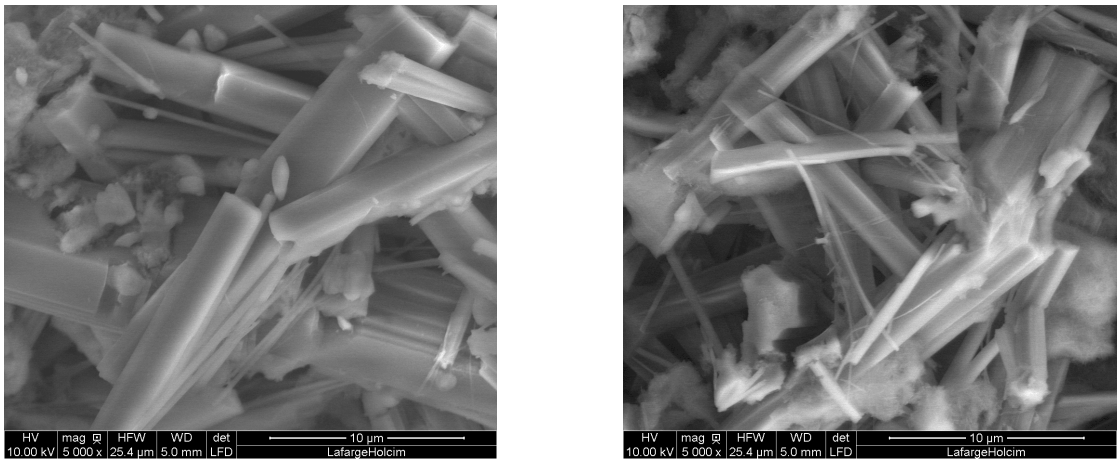

(a) Ettringite in hydrated cement (b) Meta-ettringite in oven-dehydrated cement paste

Figure A-4: Ettringite and meta-ettringite morphography

Reference

[1] Baquerizo LG et al. Impact of water activity on the stability of ettringite. Cem Concr Res 2016;79:31–44.

[2] Hargis CW et al. Carbonation of calcium sulfoaluminate mortars. Cem Concr Compos 2017;80:123–34.

FOLIO ADMINISTRATIF

THESE DE L'UNIVERSITE DE LYON OPEREE AU SEIN DE L'INSA LYON

NOM : CHEN

DATE de SOUTENANCE : 22/07/2020

Prénoms : Bao

TITRE : Study of an ettringite-based thermochemical energy storage for buildings

NATURE : Doctorat

Numéro d'ordre : 2020LYSEI056

Ecole doctorale : ED 162 – MEGA (Mécanique, Énergétique, Génie Civil, Acoustique)

Spécialité : Thermique et Energétique

RESUME :

Les besoins en énergie dédiés au chauffage et à l'eau chaude sanitaire dans des bâtiments, caractérisés par des pics de consommation en début et en fin de journée tout comme en hiver, représentent un défi d'importance vis-à-vis de l'utilisation des énergies renouvelables. Une des technologies les plus prometteuses, se présente sous la forme d'un système de stockage d'énergie dit thermochimique (TCES). Ce mode de stockage permet en effet de stocker différents types d'énergie sous la forme d'un potentiel chimique et est caractérisé par une absence de dissipation d'énergie. En tant que matériau de stockage thermochimique récemment étudié, l'ettringite conviendrait ainsi à une utilisation à grande échelle en raison de sa non-toxicité, de son faible coût de production et de sa haute densité énergétique à basse température de fonctionnement.

Cette thèse avait pour premier objectif d'étudier les propriétés physico-chimiques de l'ettringite et les mécanismes réactionnels lors des processus d'hydratation (formation d'ettringite) et de déshydratation (formation de méta-ettringite). Les connaissances acquises lors de ces travaux de thèse, vis-à-vis de la cinétique des réactions et des diagrammes thermodynamiques (Déshydratation: Ett30.6 → Ett30 → Met12 → Met6; Hydratation: Met7.4 → Met12 → hydrate de $24H_2O$ → hydrates supérieurs), permettront ainsi de mieux utiliser l'ettringite pour stocker/déstocker de la chaleur (à différentes conditions isothermes et isobares).

Après avoir étudié les propriétés de l'ettringite pure, trois liants cimentaires distincts pouvant être produits industriellement ont été utilisés afin de tester des teneurs en ettringite différentes mais aussi des mélanges de phases hydratées particulières. Les travaux effectués ont permis d'étudier les mécanismes de carbonatation de ces différents matériaux ettringitiques et de déduire plusieurs informations pertinentes quant à leur durabilité dans le cadre d'une utilisation en tant que TCES.

Enfin, le matériau cimentaire ettringitique le plus résistant au phénomène de carbonatation a été caractérisé par différentes techniques d'analyse afin de mieux maitriser l'influence des paramètres thermo-physiques sur sa performance énergétique. Ce matériau a ensuite été incorporé dans un réacteur à lit fixe, sous la forme d'un lit poreux de 56 mm de hauteur composé de granulés de 1 à 2 mm de diamètre. Le processus de chargement/déchargement de l'énergie a été réalisé pour étudier la réversibilité du couple ettringite/méta-ettringite dans diverses conditions expérimentales. Les essais réalisés dans le réacteur ont alors montré qu'une puissance instantanée maximale de 915 W par kg de matière hydratée initiale et une densité de déstockage d'énergie de 176 kWh/m^3 pouvaient être obtenues. Ces données seront très utiles pour envisager un futur prototype (à l'échelle 1:1) d'un système de chauffage contenant de l'ettringite et destiné aux bâtiments.

MOTS-CLÉS : alimentation en chauffage des bâtiments, carbonatation, cinétique, ettringite, hydratation/déshydratation, méta-ettringite, réacteur à lit fixe, stockage d'énergie thermochimique, thermodynamique.

Laboratoire (s) de recherche : Centre d'Energétique et de Thermique de Lyon (CETHIL UMR 5008)

Directeur de thèse: Frédéric Kuznik

Président de jury :

Composition du jury : Nolwenn Le-Pierrès, Stéphane Ginestet, Herbert A. Zondag, Jean-Jacques Roux, Frédéric Kuznik, Kévyn Johannes, Matthieu Horgnies